



climate change initiative

European Space Agency

# Algorithm Theoretical Basis Document Phase 2 (ATBD)



**glaciers**  
cci

Prepared by: Glaciers\_cci consortium

Contract: 4000109873/14/I-NB  
Name: Glaciers\_cci\_Ph2-D2.1\_ATBDv2.6  
Version: 2.6  
Date: 14.11.2016

Contact:  
Frank Paul  
Department of Geography  
University of Zurich  
Winterthurerstr. 190  
CH-8057 Zurich  
frank.paul@geo.uzh.ch

Technical Officer:  
Stephen Plummer  
ESA ESRIN



University of  
Zurich <sup>UZH</sup>



UNIVERSITY  
OF OSLO



UNIVERSITY OF LEEDS



GAMMA REMOTE SENSING



## Document status sheet

Version	Date	Changes	Approval
V2.1	25.11. 2014	Update Phase 2 year 1 (Landsat 8 OLI)	
V2.2	22.10. 2015	Update Phase 2 year 2 (Sentinel 1 and 2)	
V2.2	25.01. 2015	Integration of Feedback from TO	
V2.3	22.10. 2015	Year 2 update	
V2.4	25.01. 2016	Comments from TO integrated	
V2.5	02.05. 2016	Some final edits from TO included	
V2.6	14.11. 2016	Updated version for Year 3 of Phase 2	

The work described in this report was done under ESA contract 4000109873//14/I-NB. Responsibility for the contents resides with the authors that prepared it.

Author team:

Frank Paul, Tobias Bolch, Philipp Rastner (GIUZ); Kirsty Langley, Robert McNabb, Andreas Käab, Christopher Nuth (GUIO); Thomas Nagler (ENVEO); Tazio Strozzi (GAMMA); Kate Briggs, Andrew Shepherd (SEEL)

Glaciers\_cci Technical Officer at ESA:  
 Stephen Plummer

## Table of Contents

<b>Table of Contents .....</b>	<b>3</b>
<b>1. Executive Summary .....</b>	<b>5</b>
<b>2. Introduction .....</b>	<b>6</b>
2.1 Purpose of this document .....	6
2.2 Background to the approaches .....	6
2.3 General remarks .....	7
<b>3. Glacier area .....</b>	<b>8</b>
3.1 Introduction .....	8
3.2 Scientific background.....	9
3.3 Description of available algorithms .....	13
3.3.3 Developments during the first and second year of Phase 2 .....	18
3.4 Description of the algorithm chosen .....	20
3.4.1 Justification for the algorithm chosen .....	20
3.4.2 Mathematical description of the algorithm .....	20
3.4.3 Description of the processing line .....	21
3.5 Required input data and generated output .....	21
3.6 Error budget estimates and expected accuracy.....	23
3.6.1 Contributions to the error budget .....	23
3.6.2 Overall accuracy.....	23
3.7 Expected performance gains by future developments.....	24
3.8 New aspects from the Landsat 8 sensor OLI.....	25
<b>4. Elevation changes from repeat altimetry .....</b>	<b>33</b>
4.1 Introduction .....	33
4.2 Laser Altimetry .....	33
4.2.1 Scientific Background .....	33
4.2.2 Justification on the algorithm chosen.....	43
4.2.3 Mathematical algorithm development description .....	44
4.2.4 Description of the processing line .....	47
4.2.5 Input data and algorithm output .....	49
4.2.6 Error budget estimates.....	50
4.2.7 Practical considerations for implementation .....	50
4.3 Radar Altimetry .....	51
4.3.1 Scientific Background .....	51
4.3.2 Justification on the Algorithm Chosen .....	54
4.3.3 Mathematical algorithm development description .....	54
4.3.4 Description of the processing line .....	54
4.3.5 Input data and algorithm output .....	54
4.3.6 Error budget estimates.....	54
4.3.7 Practical considerations for implementation .....	54
<b>5. Elevation changes from DEM differencing .....</b>	<b>55</b>
5.1 Introduction .....	55
5.2 Scientific background on DEM generation .....	55

5.2.1. Stereoscopic DEMs .....	56
5.2.2. Interferometric DEMs .....	56
5.2.3. Laser scanning DEMs .....	57
5.3 Elevation changes from multi-temporal DEMs .....	57
5.4 Description of the algorithm chosen .....	58
5.4.1 Justification on the algorithm chosen.....	58
5.4.2 Algorithm overview .....	59
5.4.3 Mathematical description .....	59
5.4.4 Description of the processing line .....	61
5.5. Input data and algorithm output .....	61
5.6 Error budget estimates.....	62
5.7 Expected accuracy .....	63
5.8 Practical considerations for implementation .....	63
<b>6. Glacier Velocity .....</b>	<b>64</b>
6.1 Introduction .....	64
6.1.1 Ice Surface Velocity from SAR data.....	65
6.1.2 Ice Surface Velocity from Optical data.....	66
6.2 Scientific background.....	66
6.2.1 Selection of the algorithm for ice motion fields from SAR data .....	66
6.2.2 Selection of the algorithm for surface displacements from repeat optical data .....	69
6.3 Justification on the algorithm chosen .....	72
6.4 Processing line for optical data .....	73
6.4.1. Pre-processing .....	73
6.4.2 Selected algorithms for glacier velocity .....	74
6.4.3 Post-processing .....	76
6.5 Processing line for SAR .....	79
6.5.1 Pre-processing Module .....	79
6.5.2 Offset-tracking Module .....	80
6.5.3 Outlier Filtering Module .....	81
6.5.4 Geocoding Module .....	81
6.6 Input data .....	82
6.6.1 Landsat 8 Operational Land Imager (OLI) .....	83
6.6.2 Sentinel-2 MSI .....	86
6.6.3 Sentinel-1 .....	89
6.6.4 JAXA ALOS-2 PALSAR-2 .....	93
6.7 Output products .....	94
6.8 Error budget estimates.....	97
6.9 Expected accuracy .....	98
6.10 Practical considerations for implementation .....	99
<b>References .....</b>	<b>100</b>
<b>Abbreviations .....</b>	<b>111</b>

## 1. Executive Summary

This document is the Algorithm Theoretical Basis Document version 2 (ATBDv2) of the Glaciers\_cci project. It is an update of the former ATBDv2 (Glaciers\_cci, 2013e) prepared during phase 1 and with a focus of the algorithms applied in the prototype system. Having selected and justified algorithms in previous versions, the major additions in this revised version of the ATBDv2 are updates on new available sensors and their impact on the processing schemes and output products.

For the glacier area product, recent glacier outline detection studies are reviewed for possible improvements to the algorithms employed in this project; and a new section is dedicated to discussion of improvements to be gained by Landsat 8 Operational Land Imager (OLI) and sentinel 2 Multispectral Imager (MSI). For the elevation change from altimetry section the processing line has been updated; the plane fitting method is described and a new sub-section is dedicated to RADAR altimetry for the purpose of introducing and including CryoSat-2 RADAR altimetry in the production line. There are no significant changes to the elevation change from DEM differencing. In the glacier velocity section updates to post processing outlier filtering are explained and new sensors to be included in the data production are discussed, including Sentinel-1, JAXA ALOS-2 PALSAR and Landsat 8 OLI.

In each Chapter we provide an Introduction, a scientific background and a justification of the algorithm selected, before the algorithms are described in detail. A short description of the input and output data, error budget estimates, and practical considerations for their implementation are also given. More detailed descriptions of these topics can be found in the IODDv1 (Glaciers\_cci, 2013b), the DPMv1 (Glaciers\_cci, 2013c) and the UCRv1 (Glaciers\_cci, 2013d).

For glacier area it was confirmed in the round robin that band-ratio based algorithms work best for glacier mapping and that the different interpretation of debris-covered glacier parts cause the largest uncertainties. To reduce the latter, the creation of illustrated guidelines is encouraged. The Chapter on glacier elevation changes from DEM differencing highlights the importance of proper co-registration of the two or more DEMs and that care must be taken when different software products are used for the analysis as the interpretation of geolocation information might differ. Elevation changes from altimeters are best obtained along repeat tracks and from the optical (higher resolution) GLAS sensor. The RADAR altimeters were removed in ATBDv1 due to poor spatial coverage and inability to properly correct in steeper terrain. They are reinstated here along with the plane fitting method. Glacier velocity can be derived from both optical and microwave sensors using in principle the same method (tracking). In particular the selection of an appropriate image matching window size and the subsequent filtering of the results requires attention in the pre- and post-processing stage. The tracking itself works automatically and can be applied globally. InSAR techniques were disregarded for global-scale velocity determination. For using this technique to create coherence images (for identification of debris-covered glaciers) we refer to the former ATBDv2 (Glaciers\_cci, 2013e).

## 2. Introduction

### 2.1 Purpose of this document

The document provides a detailed description of the selected algorithms chosen to generate Fundamental Climate Data Records (FCDRs) of the data products requested by the end-users. As for the Phase 1 ATBD, the document is mainly structured along the Glaciers\_cci product types, i.e. glacier area, elevation change and velocity. While glacier area and elevation changes from DEM differencing and altimetry have individual chapters, velocity as derived from optical and microwave data are summarized in one chapter. There is thus some repetition of statements and the structure is not fully similar for both sensors. According to the Statement of Work (SoW), the phase 2 ATBD is an updated version of the phase 1 ATBD that provides a detailed description of the scientific background and theoretical justification for the algorithms developed and implemented. It includes:

- a description of the physics of the problem
- a definition of the scope of the algorithm
- a detailed mathematical description of the algorithm including error budget estimates
- the assumptions made for the design of the algorithm, and its limitations
- a definition of the input data required and the outputs generated
- an analysis of the computation resources needed
- practical considerations for algorithm test and validation, quality control and diagnostics,
- approaches for exception handling.

Due to the large methodological differences in generating the four products, the topics listed above are described differently for each product. However, all Chapters follow the same principle structure (section headings) to keep them comparable to some extent.

### 2.2 Background to the approaches

Using satellite data to derive **glacier outlines** over large regions or on a global scale from automated image classification techniques is a key recommendation (Tier 5) of the tiered glacier monitoring strategy of GTN-G (e.g. Haeberli, 2006). In view of the demand to further transform these outlines (contiguous ice masses) into a glacier inventory (individual glaciers with topographic attribute information), the application of modern geoinformatic techniques (using a GIS and DEMs) is required for efficient data processing (e.g. Kääb et al., 2002; Paul et al., 2002). With the free availability (and in the case of Landsat already accurately orthorectified) satellite data from USGS combined with the free DEMs from SRTM, the ASTER GDEM, or national DEMs (e.g. NED, CDED), the principle accomplishment of this task is feasible (Paul, 2010). As clearly expressed in the URD (Glaciers\_cci, 2014a), the most important task is to complete the global glacier inventory. Since the required technical specifications for the sensors used is described in the DARD (Glaciers\_cci, 2014b), we here focus on the processing methods and what is required to understand their physical background.

Multi-temporal satellite elevation data provides an effective approach to continuously monitor glacier surfaces. Glacier **elevation changes** are often used to characterize glacier mass balance variations, especially in remote areas where field measurements are difficult. Indeed, it is the large spatial and temporal coverage of satellite-derived elevation changes that increase the desirability and potential of this method for glacier monitoring. Elevation change of a glacier surface is, however, not directly transferrable into mass changes because the surface change is the result of both surface mass balance processes (accumulation, ablation or firn layer variability) and dynamical ice flux components: general downward flow, submergence in the accumulation area, and emergence in the ablation area. This makes the interpretation of short-term glacier elevation changes complicated. Therefore, the products created by Glaciers\_cci will focus on uncorrected elevation change measurements as requested in the URD (Glaciers\_cci, 2011a). However, a mean elevation change value per glacier entity or region is a product that is also requested and will thus be generated as well where it is scientifically meaningful (for instance where the data coverage is spatially complete enough). Elevation changes are derived by two general approaches; (1) repeat altimetry (LIDAR/RADAR) with a focus on repeat track measurements that have small spatial offsets, and (2) DEM differencing with a focus on the pre-processing of the DEM pairs. In both approaches, the detection of bias is essential and required corrections should be determined.

The generation of **glacier velocity** measurements from repeat satellite data is highly desirable in the glaciological community to better characterize glacier dynamics and potential changes in the dynamic behaviour of glaciers. Since in-situ measurements of velocity are limited in space due to logistical constraints of deploying GPS instruments, satellite derived velocities provide a significantly larger spatial data set, both in terms of the number of glaciers that can be measured and by providing the spatial distribution of velocity within an individual glacier. Tracking methods based on repeat optical or SAR satellite images are efficient approaches to derive surface displacements on glaciers. A large variety of tracking algorithms were investigated in the round robin (e.g. normalized cross-correlation, cross-correlation operated in the Fourier domain, least squares matching, phase correlation, orientation correlation) and two of them were selected as the most appropriate in phase 1. Based on the results of the round robin, also the key pre- and post-processing steps are described for both sensor types.

## 2.3 General remarks

A major guideline for the algorithms and processing chains described in this document is a high potential for automation. However, it should be mentioned that in many cases at least some degree of human interaction is required to derive glaciologically meaningful and reliable data of glacier areas, elevation changes and velocities. For instance, automatic glacier outlines have to be checked and corrected for debris-covered glacier parts, or some remaining velocity outliers have to be corrected manually, depending on the purpose of the application. In these cases, the goal of the algorithms and processing chains included here is to minimize the degree of human interaction and to support this interaction as much as possible. In the round robin, some of these interactions from analysts were evaluated for their impact on the quality of the result. Whenever we refer to the round robin, please check the PVASR (Glaciers\_cci, 2012b) for details. As mentioned in Section 1, the ATBDv2 (Glaciers\_cci, 2013e) was shortened compared to ATBDv0 (Glaciers\_cci, 2013a) to focus on the algorithms selected for the prototype; this version has been expanded to include discussion of new sensors. If information on other processing methods is required, we refer the reader to ATBDv0 and v1.

## 3. Glacier area

### 3.1 Introduction

Compared to the use of aerial photography for glacier mapping in the World Glacier Inventory (WGMS, 1989), the application of satellite data has the special advantage of the much larger area covered combined with a sensor in the shortwave infrared (SWIR) that allows the automated classification of clean to slightly dirty (i.e. optically thin) glacier ice (e.g. Paul and Käab, 2005). Of course, the spatial resolution is an order of magnitude lower (10 to 30 m) compared to aerial photography (about 1 m), but the smallest glacier entity that can still be called glacier (about 0.01 km<sup>2</sup> in size according to Paul et al., 2009) can still be mapped under good conditions (Andreassen et al., 2008). So in times of rapidly shrinking glaciers the gain in processing speed is really an asset. Under special circumstances it might even be possible to map nearly all glaciers of an entire mountain range within a few weeks, like for the Alps in the summer of 2003 (Paul et al., 2011) or for the western Himalaya within 3 years (Frey et al., 2012). Compared to the 30-year time span that was required to map all glaciers in the Alps in the previous inventory (Zemp et al., 2008), this is an important benefit, in particular for large scale hydrologic modelling (e.g. Zappa and Kan, 2007; Huss, 2011). So the most efficient means for repeat mapping of glaciers on a global scale is indeed provided by satellite data.

So far, 'satellite data' refers to optical data with a number of multispectral bands in various parts of the electromagnetic spectrum (from the visible to the thermal infrared). Though the SWIR band (e.g. TM5 on Landsat) allows discrimination of snow from clouds, none of the optical bands can penetrate through clouds, i.e. apart from seasonal snow cover, clouds are a major bottleneck in the operational application of satellite data for glacier mapping. If a scene has clouds over the glaciers to be analysed, the scene has to be excluded or can only partly be processed. In the latter case, the use of multi-temporal datasets might help, as usually the clouds in two, otherwise very good images are often not located at the same position. This gives the possibility to merge two data sets to get a (more or less) cloud free coverage (e.g. Le Bris et al., 2011). However, when cloud boundaries cover only parts of a glacier the issue can get rather complicated as the outline of one glacier entity might then refer to different years.

The other bottleneck is debris cover on glaciers that has the same spectral properties as the surrounding terrain and can thus not be discriminated from multispectral data alone. Though a number of techniques for debris-cover mapping have been developed in the recent past (e.g. Paul et al., 2004; Shukla et al. 2011), they all require manual post-processing to give sufficiently accurate results. With microwave data cloud penetration is not a problem, but the dielectric properties of ice and snow are not sufficiently different from other terrain to precisely map glacier extent automatically (e.g. Hall et al., 2000). However, the recent application of coherence images from ALOS PALSAR acquired during the summer months have revealed new possibilities to precisely delineate debris-covered glaciers in regions where image contrast is poor (e.g. Strozzi et al., 2010; Frey et al., 2012). For a part of Alaska even the entire delineation of glaciers from PALSAR coherence worked largely automatically (Atwood et al., 2010).

So in regard to clouds and debris-cover there is still potential for important algorithm improvements by considering also microwave data. When seasonal snow is present (and hiding

parts of the glacier perimeter), the only feasible option is to use a scene from another date. In some regions of the world this reduces the number of useful satellite scenes considerably (Paul et al., 2011), but in our experience product quality would otherwise be below acceptable standards.

Indeed, the best algorithms for automated classification of snow and ice produce results that are only different at the level of individual pixels (e.g. Paul and Kääb, 2005; Paul and Hendriks, 2010). The quality of the generated outlines does thus largely depend on the experience and qualification of the analysts responsible for the post-processing. Errors introduced by the wrong interpretation of debris cover, snow fields, or glacier parts in shadow are much larger than differences in the algorithms (Gjermundsen et al., 2011). For this reason a major task towards improved product quality and consistency is the generation of illustrated guidelines for the analyst. This should not exclude further advances in the automated classification and hence reduce the required post-processing, but in the end the analyst has to decide whether a glacier outline is acceptable or not. Statistical tests or standard error assessments do not provide this information.

## 3.2 Scientific background

In the following we focus on the main-processing stage, i.e. the glacier mapping algorithm to be applied. To find a most suitable algorithm, one has to be aware of what a glacier looks like, i.e. the spectral properties of the typical surface characteristics as seen from space. As glaciers result from the metamorphosis and compression of snow, their spectral properties are very similar to snow (e.g. Hall et al., 1988). Of course, dust, debris and liquid water on the surface alter the spectral response and can be found nearly anywhere on the glacier ([Fig. 3.1](#)). In this regard the spectral information of a satellite image pixel (in the 10-30 m range) is in most cases a mixed signal with the respective deviations from a pure (laboratory) signal. In [Fig. 3.2a](#) and [3.2b](#) a comparison of the spectral reflectance for snow of varying grain size from theoretical considerations (Dozier, 1989) with field-based measurements from Qunzhu et al. (1983) is shown. Besides the high reflectance of snow in the visible part (VIS) of the spectrum (independent of grain size), the strong reflectance drop in the near infrared (NIR) can be seen ([Fig. 3.2a](#)). The dependence of the reflectance on grain size is very high in the NIR (with smaller grains having the higher reflectance), indicating the potential to map snow grain size from the reflectance value in this spectral range. In the SWIR the reflectance increases slightly again and is still strongly dependent on grain size ([Fig. 3.2](#)). On the other hand, clouds still have a rather high reflectance in the SWIR and thus can be easily discriminated from snow with a SWIR sensor (Dozier, 1989).

In a spectral sense, glacier ice can be seen as snow with very large grain sizes, so that the spectral reflectance curve of pure glacier ice follows the curve of snow very closely. However, impurities in and on the ice (e.g. dust and soot) shift the curve of spectral reflectance downwards ([Fig. 3.2b](#)). The spectral reflectance curve of debris is based on the lithology of the material and can thus have any shape.

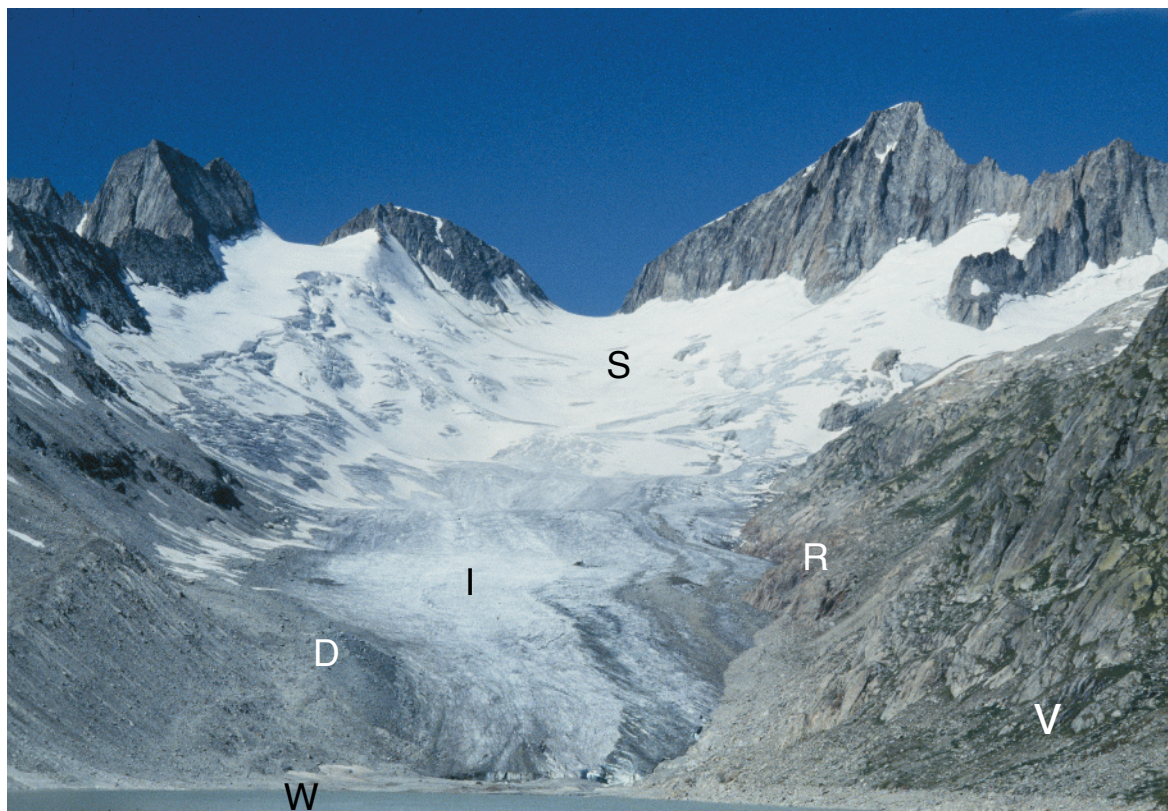


Fig. 3.1: Oberaargletscher in Switzerland. The picture illustrates the spectral reflectance of bare ice (I), debris-covered ice (D), snow (S), rock (R), vegetation (V) and turbid water (W) in the visible part of the spectrum. A spectral discrimination of the debris cover on the glacier and from the lateral moraine (in the lower left of the image) is not possible.

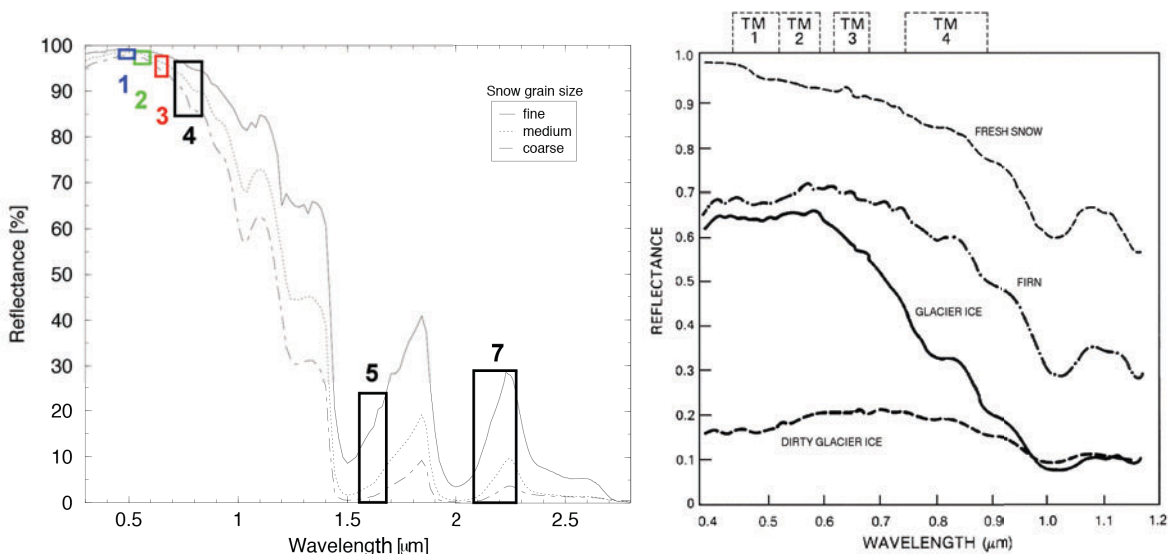


Fig. 3.2: Modelled spectral reflectance curves of snow with three different grain sizes and position of TM spectral bands (left). Spectral reflectance curves of snow, firn, ice and dirty glacier ice according to field measurements (right). The data for the left figure are taken from the ASTER spectral library (JPL, 2002), the right figure is adapted from Hall et al. (1988).

Apart from the above components, shadow on the glacier surface alters its spectral response as atmospheric scattering (brightening these regions) is dependent on wavelength. The same is true for thin clouds (cirrus or fog). A high impact on the absolute reflectance values results from illumination differences due to the topography (i.e. the sun - target - sensor geometry) and to a lesser extent from atmospheric conditions. The use of absolute reflectance values for glacier classification therefore requires topographic and atmospheric corrections (e.g. Rott and Markl, 1989).

The spectral reflectance of glaciers in the individual spectral bands is shown in Fig. 3.3 for the Landsat TM sensor (ASTER and SPOT look similar, but do not have a TM band 1 equivalent band in the blue part of the spectrum) for a typical high-mountain region with glaciers (cf. Paul, 2002). In agreement with the spectral curves shown in Fig. 3.2, the high reflectance over snow in the VIS to NIR (VNIR) bands (TM1, TM2, TM3, TM4) and the lower reflectance over glacier ice can be seen. In the NIR the low reflectance of water and the higher reflectance of vegetation become obvious. The very low reflectance of glacier ice and snow in the SWIR can be seen in TM 5 and TM 7 (not shown here). The reflectance of water is also very low and vegetation and rock have a very high surface reflectance. Finally, the digital numbers (DNs) in the thermal infrared band (TIR) of TM6 depend on surface temperature. They are thus related to surface emission rather than reflectance. The higher the temperature is, the higher the DNs are and vice versa. Hence, glacier ice and snow (at the melting point) have rather low DNs, whereas sunlit mountain slopes are already warmed at the time of image acquisition and appear much brighter. Terrain in shadow is also cooler and thus appears somewhat darker. Most noticeable is the much coarser resolution (120 m) of TM band 6 (ETM+: 60 m, ASTER: 90 m) compared to the other bands.

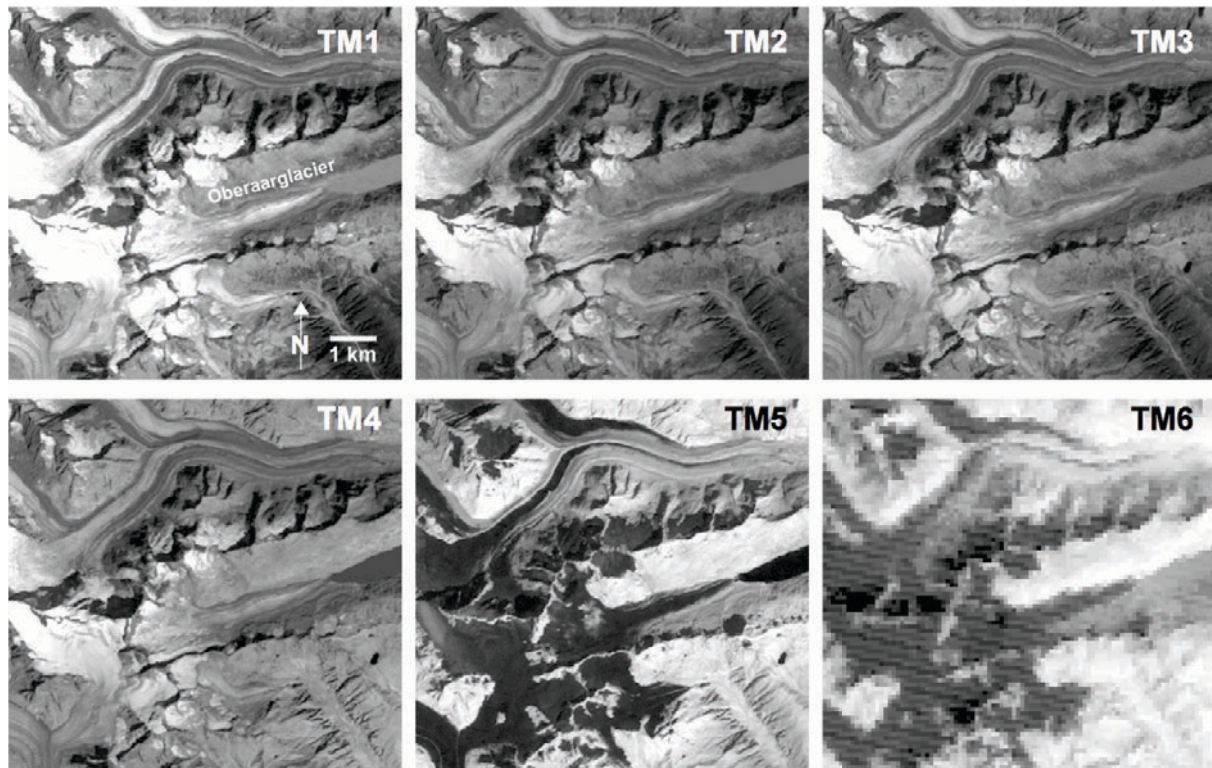


Fig. 3.3: Visualization of reflectance values in TM bands 1 (TM1) to 6 (TM6) for a subset of a Landsat TM scene around Oberaargletscher in the Swiss Alps (image size is 9.5 km by 9 km).

The thermal band was proposed in various publications as being useful to delineate debris-covered glacier parts, due to the cooling of the rocks on the surface from the underlaying ice (e.g. Shukla et al., 2011 and references therein). However, we are sceptical that this really works for alpine type glaciers. In most cases some bare ice is included in the related mixed pixels (strongly reducing the temperature of the respective pixel) and the effect of differential thermal heating of the rocks by the sun is rather obvious. However, in the case of a (thin) volcanic ash layer and comparably large glaciers (e.g. the Vatnajökull icecap on Iceland), the thermal band could be used as an alternative to the SWIR band (Bishop et al., 2004), i.e. all glacier ice and snow has a similar low reflectance (independent of the ash cover).

The different spectral responses of ice and snow compared to other surface types (water, rock, vegetation) or clouds, allows them to be classified automatically (see section 3.3). However, in the post-processing stage omission and commission errors have to be corrected (e.g. adding debris cover or glacier parts in shadow, removing lakes). For this purpose contrast enhanced RGB composites are created from the different spectral bands that are used in the background to guide the correction process (see examples in Fig. 3.4). The most useful combinations in this regard are the classical band 3, 2, 1 (natural colours with TM) and 4, 3, 2 (false colour infrared) combination, as well as the band 5, 4, 3 false colour composite (FCC). While the 321 composite is best suited to identify ice and snow in shadow, the 432 composite has best contrast to identify water surfaces, vegetation trimlines, snow cover and drainage divides in the accumulation region. The 543 FCC allows a clear identification of glaciers (they appear in light blue), helps to identify clouds (which appear white) and provide good contrast for debris cover identification. Thus all three band combinations are useful and should be generated in the pre-processing stage from the raw data using digital image processing software.

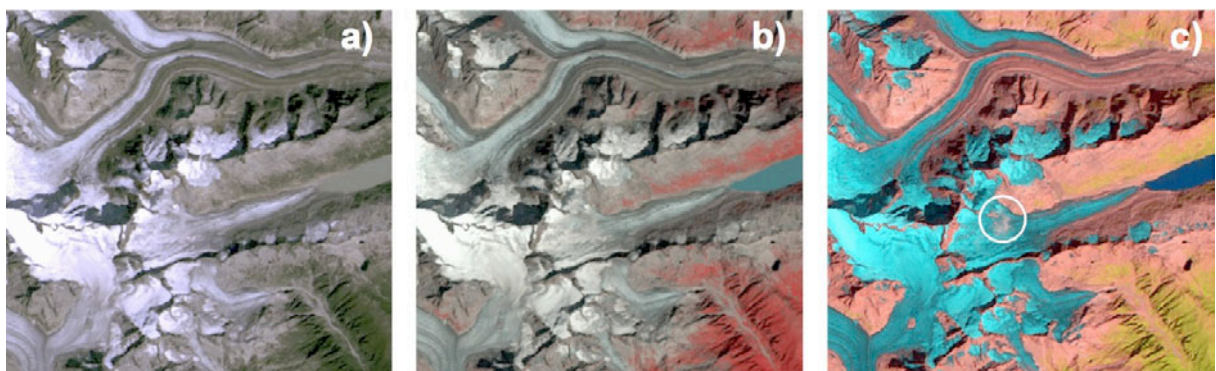


Fig. 3.4: RGB composites of the region shown in Fig. 3.3 with a) bands TM 3, 2, and 1, b) 4, 3, 2, and c) 5, 4, 3. The small cloud is only visible in this image (white circle).

The algorithms presented in the following sections are based on raw DNs, i.e. they are not converted to top-of-atmosphere (TOA) reflectance values or corrected for topographic or atmospheric effects. The main reasons are: (a) the latter requires a DEM that has no artefacts and is perfectly aligned with the satellite image. This is nearly impossible to achieve, as the registration error of satellite images is seldom better than +/- 1 pixel (RMSE), in particular in steep high-mountain terrain. Without a proper coregistration, artefacts are introduced to the reflectance values during topographic correction (e.g. due to over correction), which reduce the quality of the classification. At the same time a 'perfect' topographic correction would

remove subtle reflectance differences that are important to classify glaciers accurately (e.g. in shadow). (b) Atmospheric correction requires a number of atmospheric parameters being available (at least visibilities at different altitudes) which is often not the case in remote regions where glaciers are found. (c) The most accurate mapping methods are based on band ratios. They partially normalize topographic and atmospheric conditions within a scene and thus work without this pre-processing step. Using TOA reflectance instead of DNs does not improve the classification so this conversion is not required either (Paul, 2001).

### 3.3 Description of available algorithms

A wide range of glacier classification methods have been developed and compared in the past two decades (e.g. Albert, 2002; Paul et al. 2003; Sidjak and Wheate, 1999). They range from manual delineation to simple band ratios (e.g. Bayr et al., 1994; Jacobs et al., 1997; Paul 2002), to more complex band ratios such as the Normalized Difference Snow Index (NDSI) (e.g. Racoviteanu et al, 2008), and supervised classification techniques like spectral end members (Klein and Isacks, 1999), maximum likelihood classifiers (Aniya et al., 1996), principal component analysis (PCA) (Sidjak and Wheate, 1999) or fuzzy set theory (e.g. Binaghi et al., 1997). For (operational) glacier mapping on a global scale, the algorithm to be applied must be simple (in terms of the required pre-processing), accurate (compared to a reference data set and/or other algorithms), and robust (transferable to other regions without changing too many of the parameters). Hence, a high pre-processing workload is only justifiable when the results are much better than with less demanding algorithms. Hence, all supervised (e.g. selection of training areas or end members) or scene dependent methods (e.g. PCA) are too demanding (see Albert (2002) for a detailed comparison) and are not considered further.

For the same reason, band ratios have become a quasi-standard for glacier mapping in the past decade (e.g. Racoviteanu et al. 2008), given that a SWIR band is available. When only panchromatic or false colour infrared images are available, only manual delineation of the glacier outlines can be applied. However, despite the often much higher resolution of the related panchromatic images (e.g. from aerial photography or high resolution satellite sensors, including Corona and Hexagon scenes), this could be more error prone than glacier mapping with a lower resolution SWIR band. The example in Fig. 3.5 illustrates this for the Waxeggkees in the Zillertaler Alps (Austria), where the surrounding rock has the same spectral reflectance in the VIS as bare ice. As manual delineation needs to be applied in the post-processing stage in any case, we focus in the following on the description of band ratios using a SWIR band. The characteristics of the three most often applied band ratio classifiers is provided in Table 3.1.

The band ratio method is based on the division of the (high) DNs over ice and snow in the red band by the low DNs in the SWIR yielding high values over glaciers and low values elsewhere. Using a simple threshold the resulting ratio image can be segmented into glacier (black) and other terrain (white). This works for all ratios, either red/SWIR, NIR/SWIR or the NDSI: (green+SWIR)/(green-SWIR). As an example for the red/SWIR band ratio (e.g. TM3/TM5) the algorithm in pseudo code is:

```
IF (red/SWIR) > thr THEN glacier ELSE other
```

The threshold ‘thr’ is often close to 1.8 (+/-0.2) for this band combination. Depending on the software used, the implementation of the algorithm might look slightly different.



*Fig. 3.5: Screenshot from Google Maps showing the Waxeggkees in the Zillertaler Alps (Austria). The glacier is nearly invisible in this natural colour image, indicating that a high spatial resolution alone is not always sufficient to accurately map glaciers.*

Unfortunately, certain adjustments have to be made to all band ratios. An additional threshold in the blue (TM1) or green (AST1) band is required to improve the often occurring misclassification of rocks in shadow when using the red/SWIR ratio. The latter is due to the atmospheric scattering that is still present in the red band and brightens bare rock in shadow similar to ice in shadow. Band 1 is highly sensitive to atmospheric scattering and is strongly reflected from snow. Snow and ice in shadow is thus in general much brighter than rock in shadow and can be separated by a threshold (Paul and Kääb, 2005).

This correction is not required for the NIR/SWIR ratio as atmospheric scattering (or path radiance) is very low in the NIR. However, the high reflectivity of vegetation in the NIR often results in a misclassification of vegetation in shadow. This can be removed by additionally classifying vegetation, for example using the Normalized Difference Vegetation Index (NDVI). Of course, this step might not apply in regions without vegetation and it has to be considered on a case-by-case basis if red/SWIR or NIR/SWIR gives the better results (e.g. Andreassen et al., 2008; Paul and Kääb, 2005).

The NDSI has problems in regions with cast shadow as the high path radiance present in the green band needs to be subtracted before the NDSI is applied. The lowest DN in the respective scene can be found by histogram analysis and must then be subtracted from all DNs. This method is also named Dark Object Subtraction (DOS) in the literature (Chavez et al., 1988). The results are then very similar to the red/SWIR ratio (cf. Paul and Kääb, 2005).

Table 3.1 provides a summary of the three algorithms described above.

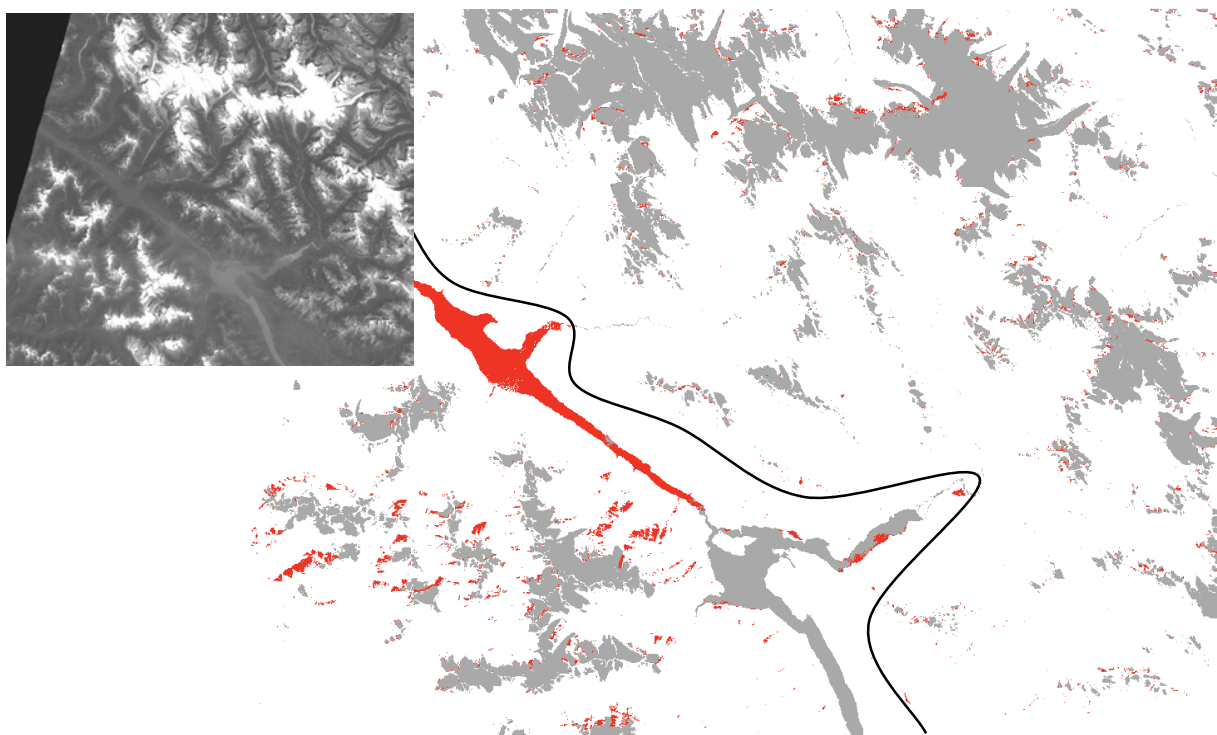
<b>Abbreviation</b>	<b>BR RS</b>
<b>Algorithm</b>	Band Ratio with the red and SWIR bands (e.g. TM3/TM5)
<b>Reference</b>	Paul et al. (2003)
<b>Applications</b>	Paul and Kääb (2005), Andreassen et al. (2008), Paul et al. (2009)
<b>Description</b>	Strong differences in spectral reflectance of ice and snow in the SWIR compared to other terrain and the VNIR bands allows their automated classification (clean to slightly dirty glacier ice) from a simple band ratio.
<b>Advantages</b>	<ul style="list-style-type: none"> <li>- The algorithm is very simple and the thresholds are robust, i.e. the result is not very sensitive on the exact value and a best value can easily be found.</li> </ul>
<b>Disadvantages</b>	<ul style="list-style-type: none"> <li>- Rock in shadow and turbid lakes are also mapped</li> <li>- An additional threshold in band TM1 is required to improve the shadow classification and wrong lakes need to be removed</li> </ul>
<b>Improvements</b>	The thresholds have to be determined interactively, an automated determination of both thresholds should be developed
<b>Abbreviation</b>	<b>BR NS</b>
<b>Algorithm</b>	Band Ratio with the NIR and SWIR bands (e.g. TM4/TM5)
<b>Reference</b>	Paul et al. (2003), Paul and Kääb (2005)
<b>Applications</b>	Paul et al. (2002), Paul (2002), Jacobs et al. (1997), Bayr et al. (1994)
<b>Description</b>	Strong differences in spectral reflectance of ice and snow in the SWIR compared to other terrain and the VNIR bands allows their automated classification (clean to slightly dirty glacier ice) from a simple band ratio.
<b>Advantages</b>	<ul style="list-style-type: none"> <li>- The algorithm is very simple and the thresholds are robust, i.e. the result is not very sensitive on the exact value and a best value can easily be found.</li> <li>- Is less sensitive to lakes</li> </ul>
<b>Disadvantages</b>	<ul style="list-style-type: none"> <li>- also maps vegetation (in shadow) that requires an additional threshold</li> <li>- sometimes misses ice in shadow</li> </ul>
<b>Improvements</b>	The threshold has to be determined interactively, might be merged with BR RS
<b>Abbreviation</b>	<b>NDSI</b>
<b>Algorithm</b>	Ratio with the green and SWIR bands (e.g. (TM2+TM5)/(TM2-TM5))
<b>Reference</b>	Paul and Kääb (2005)
<b>Applications</b>	Racoviteanu et al. (2008)
<b>Description</b>	Strong differences in spectral reflectance of ice and snow in the SWIR compared to other terrain and the VNIR bands allows their automated classification (clean to slightly dirty glacier ice) from a simple band ratio.
<b>Advantages</b>	None compared to BR RS and BR NS (i.e. results are the same)
<b>Disadvantages</b>	<ul style="list-style-type: none"> <li>- All rock in shadow and turbid lakes are also mapped when DOS is not applied to the green band before the ratio</li> <li>- Histogram analysis has to be performed manually</li> </ul>
<b>Improvements</b>	All thresholds have to be determined interactively, an automated determination of both thresholds should be developed

Table 3.1: Details of the algorithms used for glacier mapping. Glaciers\_cci will preferably use BR RS and sometimes also BR NS for data production.

To a variable extent, all of the above methods misclassify turbid lakes as glaciers. While there is some potential to also classify lakes automatically from multispectral information alone (e.g. Huggel et al., 2002) and thus remove them from the glacier map, there is some overlap with glaciers that can remove correctly classified glacier pixels. In this regard, the safest way is to manually select (by visual inspection of the satellite image) and delete the lake polygons at the post-processing stage (after vectorization of the outlines).

Finally, in some cases a correct spectral classification does not result in a correct classification of the object. For example, lakes on the surface of a glacier need to be included in the glacier area, whereas ice bergs or sea ice have to be excluded. This is currently most effectively performed in the vector domain of the post-classification stage.

From the comparison of the algorithms listed in Table 3.1 it becomes clear that the threshold selection is the most critical step for the classification. Currently, the advice is (e.g. Racoviteanu et al., 2009) to select this threshold in a most sensitive region (shadow) in a way that the workload for post-processing is minimized. In most cases this means that a rather low value for the TM1 threshold is used to get all ice and snow in shadow properly included. At the same time this increases noise or misclassification at other places. However, these additional (often isolated pixels) either do not matter (e.g. over water) or can be later removed by a noise filter. In some cases it is not possible to include the ice in shadow in one part of the image without including all bare rock in shadow in another part of the image. This can happen as a consequence of special atmospheric conditions (e.g. haze or fog), that locally increases path radiance. In such a case two glacier masks with two different thresholds were created and digitally combined afterwards. In Fig. 3.6 an example of such a dual classification from the Canadian Rockies is shown. The decision is based on visual inspection.



*Fig. 3.6: Glaciers as mapped by two different thresholds. Red pixels were included below and excluded above the black line. The inset (TM 1) illustrates the subtle haze conditions.*

A final processing step is the application of a noise filter (e.g. 3 by 3 median) to eliminate isolated pixels (e.g. snow patches) and close small gaps on a glacier (e.g. in shadow). Whether the application of this filter is really a benefit for the mapping or not has to be decided on a case-by-case basis. In Fig. 3.7 we demonstrate the sensitivity of the algorithm on the threshold value applied and the changes of the glacier map due to the application of a median filter (3 by 3 kernel size). The number of pixels added by lowering the threshold in steps of 0.1 is very small. Moreover they appear in regions that have to be carefully checked and often corrected anyway (debris-cover and shadow). In this regard the threshold value can be considered as robust and good results were likely achieved even with a fixed threshold value (around 1.9 in this case). With a threshold of 1.8 (all colours) already some isolated noisy pixels (red) appear. This indicates that the threshold value should not be much lower than this. The median filter efficiently closes isolated gaps (blue pixels in the right image of Fig. 3.7) but at the same time also deletes isolated pixels or small pixel clusters (red). As the latter are often related to isolated (seasonal) snow patches, this consequence is rather beneficial. However, in regions with many very small glaciers and no seasonal snow, it might be better to proceed with the raw glacier map (e.g. Paul et al., 2011b).

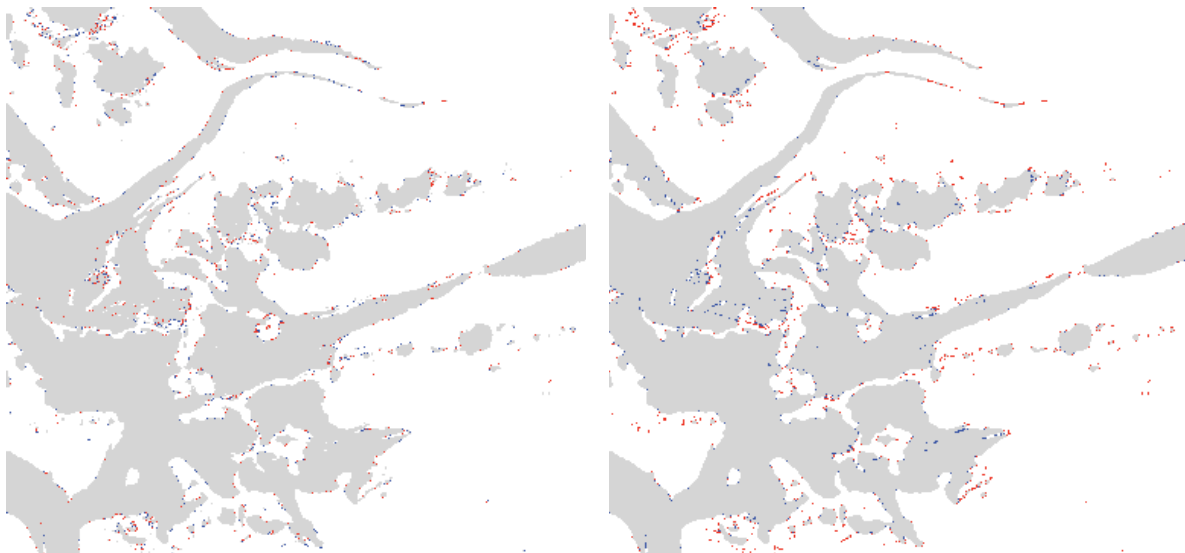


*Fig. 3.7: Left: Three glacier maps combined resulting from three threshold values: 1.8 (all colours), 1.9: (grey and blue), 2.0 (grey). Right: Effect of a  $3 \times 3$  median filter: red pixels are removed and blue pixels are added (shown here for the map with the threshold 1.9).*

Applications in various regions of the world have shown that also glaciers under thin cirrus clouds (e.g. from aircraft contrails) or other optically thin clouds can be mapped with the TM3/TM5 band ratio (Paul and Andreassen, 2009). More difficult to map is bare ice in the shadow of convective clouds or deeply crevassed zones creating local shadows. For all these regions careful visual inspection and maybe correction of the generated outlines is required, using one of the above mentioned RGB composites in the background. The quality of this step depends on the contrast of the image and the skills of the analyst to interpret subtle features. In any case, the application of one of the above automated methods to map clean glacier ice is strongly recommended compared to a full manual digitization. The latter should be restricted to applying edits to the initial mapping.

### 3.3.2 New algorithms developed during Phase 1

In the past 3 years some new studies have investigated further methods to map glaciers (see overview in [Table 3.2](#)). A study by Burns and Nolin (2014) used topographically and atmospherically corrected image bands and the NDSI method to map glaciers in the Cordillera Blanca in several years. The advantage of the corrections compared to using raw DNs for the NDSI is not described. The main conclusion to carefully select the threshold value is in agreement with the workflow used in Glaciers\_cci.

The study by Holobaca (2013) integrated the glacier mapping algorithms presented in Table 3.1 in an automated workflow (Toolbox for ArcGIS) to determine glacier changes and their dependence on topographic characteristics (slope, aspect). The suggested workflow is very specific to the selected site (an ice capped volcano) and requires perfect co-registration of the two satellite images to work. The challenging issue of separating the ice cap into individual glaciers is not addressed in that study.

The study by Yan et al. (2014) investigated rough set theory as an approach to classify glaciers. The method also integrates the BR RS method (TM3/TM5) and considers additional information such as thermal bands, slope information and homogeneity texture. The method is rather complex and requires a priori knowledge, but in the end also fails in including the debris-covered glacier parts in case of a complete coverage. The example shown in the study indicates that the ice is more dirty than debris covered, i.e. not a real challenge.

A similar approach for glacier mapping has been investigated by Rastner et al. (2014) using object based image analysis (OBIA) in three different test sites. It was demonstrated that the results obtained with OBIA are as good as with the standard methods listed in Table 3.1 or even slightly better when the thermal band is providing useful information. The main advantage was the reduced workload for post-classification editing as context based information could be incorporated in the analysis. Mapping of heavily debris-covered glaciers worked quite well in the Himalaya test site, but manual corrections remained also in this case.

Overall, the newly developed algorithms provided interesting results but none of them need to be added to those already selected. In general, they are more difficult to apply without providing a significant improvement of accuracy, helping to find the threshold automatically or solving the key challenge debris cover mapping. We will thus continue mapping glaciers with the methods presented in Table 3.1 (preferably BR RS).

### 3.3.3 Developments during the first and second year of Phase 2

Several publications on the mapping of debris-covered glaciers have appeared during the first year of Glaciers\_cci Phase 2, six alone in 2015 ([Table 3.2](#)). This demonstrates the recently increased interest in this topic and the wish of the scientific community to solve it. Thereby, most new studies utilize the method developed by Paul et al. (2004) and extend it with either new spectral bands (thermal), further data products (velocity fields) or datasets (river network) and other techniques (OBIA). In general, a higher complexity of the proposed methods also increases the accuracy of the results obtained. However, the coarser resolution of thermal bands (120 m for TM, 90 m for ASTER, 60 m for ETM+) and the dependence on high-quality DEM data still requires careful visual control and manual editing. Although we do not see a need to implement any of these new algorithms in the Glaciers\_cci processing line, it is important to carefully follow the research activities in this regard.

Nr.	Author	Year	Journal	Topic	Title
1	Holobaca	2013	IJRS	Mapping & future	Glacier Mapper – a new method designed to assess change in mountain glaciers
2	Rastner et al.	2014	JSTARS	Mapping w/ OBIA	A comparison of pixel- and object-based glacier classification with optical satellite images
3	Yan et al.	2014	AdvSR	Mapping & outlines	Glacier mapping based on rough set theory in the Manas River watershed
4	Burns & Nolin	2014	RSE	NDSI mapping	Atmospherically-corrected Landsat imagery to measure area change in the Cordillera Blanca, Peru (1987-2010)
5	Bhardwaj et al.	2014	CRST	Debris mapping	Mapping debris-covered glaciers and identifying factors affecting the accuracy
6	Paul et al.	2015	RSE	Algortihm overview	The glaciers climate change initiative: Methods for cre-a-ting glacier area, elevation change and velocity products
7	Bhardwaj et al.	2015	IJAEOG	Facies & debris m.	Applicability of Landsat 8 data for characterizing glacier facies and supraglacial debris
8	Alifu et al.	2015	IJRS	Debris + TIR	A new band ratio technique for mapping debris-covered glaciers using Landsat imagery and a DEM
9	Gosh et al.	2015	JAppIRS	Debris + TIR	Mapping of debris-covered glaciers in Greater Himalaya, Ladakh, western Himalaya, with remote sensing and GIS
10	Shukla and Ali	2016	Anngl	Debris + TIR	A hierarchical knowledge-based classification for glacier terrain mapping: a case study from Kolahoi Glacier, Kashmir Himalaya
11	Khan, Naz, Bowling	2015	JHydr	Snow, ice, debris mapping	Separating snow, clean and debris covered ice in Upper Indus Basin, Hindu Kush–Karakoram, using Landsat images between 1998 and 2002.
12	Smith et al.	2015	TC	DC mapping	Improving semi-automated glacier mapping with a multi-method approach: applications in central Asia
13	Robson et al.	2015	RSE	DC mapping	Uses OBIA to combine optical and coherence images to map debris-covered glaciers Nepal
14	Winsvold et al.	2016	JSTARS	Multi-temp. mapping	Regional glacier mapping using optical satellite data time series

Table 3.2: Overview on the new literature relevant for glacier mapping. All publications are listed in the References section.

More recently, new approaches are developed to better exploit the long Landsat time series available, and the upcoming dense time series from Sentinel-2, possibly combined with Landsat 8. Winsvold et al. (2016) developed several application scenarios for modified and improved glacier mapping based on such dense time series of multispectral satellite images, such as synthesising optimal mapping scenes or exploiting quasi-sinusoidal annual variations in snow/ice reflectances. Interestingly, also these new approaches work best if based on the robust VNIR/SWIR band ratios.

On a longer time scale there is an issue with an increasingly poor temporal match, i.e. when DEM information (or flow velocities) are derived from datasets that have been acquired several years earlier or later. A similar problem applies to the PALSAR coherence scenes (acquired in 2007 to 2009) that are used in Glaciers\_cci for correcting outlines manually as the latter are based on scenes acquired around the year 2000. However, terminus positions and extents of heavily debris-covered glaciers change only slowly in most cases (Scherler et al., 2011), allowing a  $\pm$  decadal difference in acquisition dates, i.e. for satellite scenes acquired between 2000 and 2015. For the latter period (around 2015) coherence images derived from Sentinel 1 might be used as well as first results for a test site in the Swiss Alps were very

promising. In Glaciers\_cci we will follow the strategy to manually correct debris cover and water with support from coherence images and high-resolution data in Google Earth. The 10 m resolution images from Sentinel 2 will allow a more accurate delineation of debris cover on glaciers from the beginning (see Section 3.9). After all, outline accuracy is driven by the skills of the analyst and a uniquely correct interpretation might not exist in many cases. This implies that change assessment should only be performed by the same analyst.

### 3.4 Description of the algorithm chosen

#### 3.4.1 Justification for the algorithm chosen

All algorithms described in Table 3.1 were applied for glacier mapping by the participants of the round robin. Additionally, an ISODATA clustering algorithm was applied on the first 5 principal components. The overlay of the generated glacier outlines as shown in Figs. 2.12 and 2.13 of the Phase 1 PVASR document (Glaciers\_cci, 2012b) demonstrate that all of the applied algorithms perform equally well, i.e. they can only be discriminated at the level of individual pixels. In this regard, no preference can be given to any of the algorithms and the choice has to be made according to other criteria. For Glaciers\_cci the BR RS method is chosen, i.e. a threshold applied to a band ratio with the red and shortwave infrared band (e.g. TM3/TM5) combined with an additional threshold in a blue or green band (e.g. TM1) to improve classification in cast shadow as required. A key reason for this selection is also the fast and easy processing and the related implementation in simple scripts. Three decisions have to be taken by an operator: (1) the threshold for the band ratio, (2) if an additional blue or green band should be applied and if yes, the threshold, and (3) if a median filter should be applied for smoothing or not. Once these have been determined, the algorithm can be applied.

As the round robin demonstrated, product quality for debris-covered glaciers is driven by the manual corrections applied (e.g. Paul et al. 2013). These differ largely among the analysts (in particular for debris cover) and will be difficult to homogenize. The way forward might be in the compilation of illustrated guidelines demonstrating for various examples around the world where to place the boundary. However, differences in interpretation - despite clear visibility - also occur for the accumulation region as a recent comparison by Nagai et al. (2016) for various glacier inventories in Bhutan has shown. In the case of manually digitized glacier extents and dependent on the purpose of the inventory, the steep accumulation areas of glaciers were neglected, resulting in much smaller overall extents for the specific region. As mentioned above, also these differences result in the general recommendation to only perform change assessment with inventories created by the same analyst.

#### 3.4.2 Mathematical description of the algorithm

Product generation from the raw data requires a pre-, main and post-processing stage (see 3.4.3). We focus in this section on the main processing stage that is largely automatic. As described in section 3.3, the mathematical core of the algorithm is very simple, as just the raw DNs (converted to floating point for at least one of the bands) of two image bands have to be divided by each other (resulting in a ratio image) and a threshold has to be applied to convert the ratio image into a binary image (following the rule to minimize workload for manual editing). Together with the conversion of the original geotif (*etm230009\_010820b1.tif*) to the grid format of the software (*imagegrid*), a ratio applied to the blue band (*k1gr*), the application of a median filter (*focalmedian*) to the resulting binary image and the subsequent raster to vector conversion (*gridpoly*). The script performing these steps (here in Arc Macro Language or AML coding for illustration) might look like this:

```

imagegrid etm230009_010820b1.tif k1gr
imagegrid etm230009_010820b3.tif k3gr
imagegrid etm230009_010820b5.tif k5gr
grid
t = con((float(k3gr) / k5gr) > 1.8, 0, 255)
tt = con(t == 0 and k1gr > 45, 0, 255)
tmed = focalmedian(tt)
ttt = setnull(tmed == 255, 0)
q
gridpoly ttt glmap1

```

The analyst has to adjust the red numbers (1.8 and 45) in a text editor and run the script again until a satisfying result is achieved. Satisfying means that the workload for post-processing (i.e. correction of regions in cast shadow) is minimized. By writing the outlines to different filenames (*glmap1*, *glmap2*, ...), the improvements can be monitored (compared to a contrast enhanced version of the original satellite image) and the most appropriate threshold selected. When Landsat 7 ETM+ scenes in scan-line corrector off mode are processed, a couple of scenes with missing lines located at different places can be processed and the resulting grids merged at the *tt* or *tmed* level (for a smooth transition) before the raster vector conversion.

### 3.4.3 Description of the processing line

A schematic overview of the entire processing line is presented in Fig. 3.8. In the pre-processing step appropriate satellite scenes (in regard to snow and cloud conditions) have to be selected from the quick-look catalogue, downloaded, converted to the file formats of the digital image processing software applied, and RGB composites (see Fig. 3.4) might be created. Then the algorithm is applied, the thresholds selected and the raw vector outlines are exported for post-processing at three further levels (L0, L1, L2) and GLIMS conversion.

The post-processing of the raw glacier outlines is divided into four major steps: (a) correction of the outlines to L0 (e.g. wrongly classified, debris, water, shadow and clouds), (b) intersection with drainage divides to obtain glacier entities to L1, (c) calculation of topographic parameters for each glacier (L3), and (d) conversion to the RGI format and submission. For steps (b) and (c) a DEM is required and additional scripts have to be applied.

## 3.5 Required input data and generated output

The input data required to generate the output with the algorithms described above are an orthorectified satellite scene (with at least the geometric accuracy of the L1T product from USGS) and a DEM. Further details are described in the DARD (Glaciers\_cci, 2011c). While the satellite data are normally provided in geotif format, the DEMs use a variety of formats (bil, geotif, ASCII, grid, etc.). As a starting point, these formats have to be converted to the storage format of the digital image processing and GIS software used. The next step is related to pre-processing work (e.g. creation of true and false colour composites, deriving hillshades, contour lines and drainage divides from the DEM), before one of the algorithms described above is applied in the main processing stage. The output is a binary raster map that is converted to the vector format before the editing in the post-processing stage can start. For this purpose the entire dataset is still in the UTM projection of the satellite scene(s) used as an input. The further processing follows the above four steps as in the GlobGlacier project.

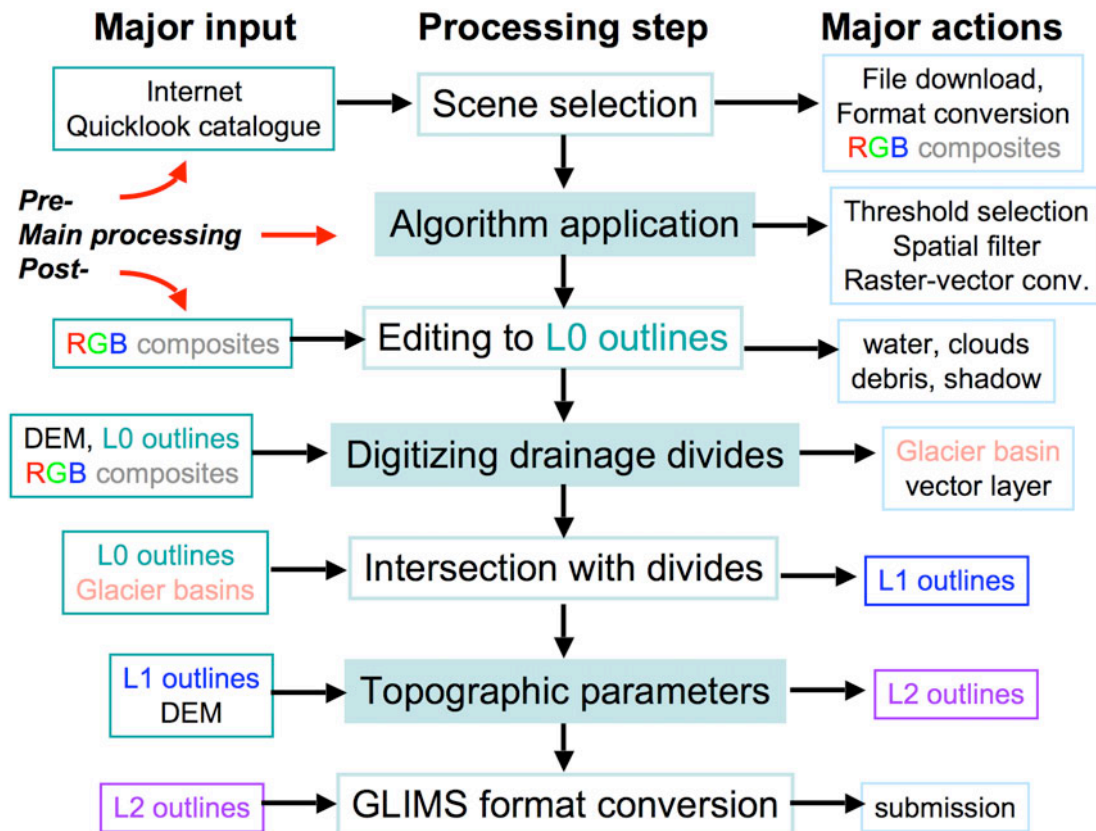


Fig. 3.8: Generalised processing work flow including the key steps of the pre- and post-processing. The main processing step ('Algorithm application') is described in section 3.3.

To facilitate internal communication, a tiered terminology was developed to discriminate different levels of processing. These levels are not related to the processing levels of satellite data in general (e.g. as used by ESA), but just to help to be precise and short. The raw glacier outlines have level 0 (L0), outlines corrected for gross errors (e.g. water, sea ice, clouds) have L0a, and fully corrected outlines (debris, shadow and all other issues) have L0b. Deriving individual glaciers (L1) from the L0b outlines requires to digitally intersect the L0b outlines with drainage divides that need to be derived beforehand from the DEM. The digitization of drainage divides is time consuming as it requires manual work, but it has to be done only once. For the glacier inventory, the L1 outlines are digitally combined with a DEM to have topographic parameters for each glacier (L2 product). Finally, the outlines are converted to the GLIMS format and submitted.

Although the details of the data processing work-flow will vary with the software used to process the data, the major steps described in Fig. 3.8 are common to nearly all software products. While the main processing algorithm works largely automatically, the other steps require more intense intervention by the analyst. However, some automated (script-based) processing is available for some of them as well (e.g. deriving L2 from L1 outlines). It has to be noted that the intermediate products of Level 0 and 1 are also useful for some applications (e.g. computing the sea-level contribution of glaciers).

## 3.6 Error budget estimates and expected accuracy

### 3.6.1 Contributions to the error budget

When considering the final glacier outline product, errors are introduced at the pre, main and post-processing stage. The quantification of the respective errors require different measures and are sometimes difficult to assess. As a first step, we provide an overview on the potential error sources in [Table 3.3](#). From this table it becomes clear that the largest errors are introduced in the post-classification stage. They could be up to one order of magnitude larger than errors caused by the algorithm or the mosaicing of scenes in UTM projection (e.g. when debris-cover is not included). This is indeed not the error that occurs when the debris cover is manually corrected. However, in this case other errors occur (generalization, inconsistent interpretation of mixed pixels) that can be determined by multiple digitizations. The magnitude of these errors was assessed in the round robin (Glaciers\_cci, 2012b). The geolocation error has no direct effect on glacier size, but needs to be considered when the outlines are combined with a different DEM (e.g. drainage divides).

Step	Uncertainty	Typical	Measure	Comment
Pre-processing	geolocation	+/- 1 pixel	GCPs (provided with the Metadata information)	only relevant for L1/L2 outlines (DEM fusion)
Main- pro- cessing	algorithm	< 3%	validation data	accuracy is for debris-free ice
	threshold	< 5%	overlay of binary maps	see Gjermundsen et al. (2011)
Post- pro- cessing	median filter	<2%	RGB composites filtered vs. unfiltered	could be larger for very small glaciers
	water	> 100%	visual inspection (432)	should be removed
	other ice	> 100%	visual inspection (432)	should be removed
	debris	> 50%	comp. with ground truth	requires manual digitization
	shadow	< 50%	visual inspection (321)	can be locally difficult to identify
	projection	<2%	comparison with equal area projection	error <2% for +/-2 scenes combined in UTM projection

*Table 3.3: Uncertainties contributing to the overall error budget.*

When assessing an error against a reference data set, several issues have to be considered to derive the correct conclusions: The area of the glacier (polygon) changes with pixel size (e.g. Paul et al., 2003), at a much higher spatial resolution different features become visible, and without a band in the shortwave infrared (e.g. panchromatic imagery) the determination of the outline could be much more complicated (see Fig. 3.5). Moreover, some care has to be taken that the projection of the data used for comparison is the same. The reference data set that is used for comparison (or validation) must be acquired at the same point in time (week is sufficient in most cases) or at least the snow conditions must be the same.

### 3.6.2 Overall accuracy

The round robin for glacier area clearly revealed (cf. Paul et al., 2013), that product accuracy depends on the correct interpretation of the debris-covered glacier parts by the analyst and that it is difficult to determine the accuracy correctly, as potential reference datasets have about the same precision (a few percent). So the automated mapping with the band ratio method is as precise as manual digitization on the same (Landsat) or higher resolution imagery when applied to clean ice. Illustrated guidelines should be prepared to improve the consistency of the glacier mapping for glacier ice under debris cover.

### 3.7 Expected performance gains by future developments

As data availability and technical development is a continuous process, new algorithms and further improved products are expected in the future. The Glaciers\_cci consortium will monitor the ongoing efforts and actively participate in related activities. Key technical issues that might be improved in the near future are:

- (a) higher consistency of the generated products globally (through illustrated guidelines)
- (b) improved outlines for debris-covered glaciers (by integrating coherence images)
- (c) better geo-location accuracy of the products (orthorectification with improved DEMs)
- (d) a reduced workload for post-processing once glacier outlines are available
- (e) a more easy conversion of outlines to the GLIMS format (development of scripts)
- (f) availability of data processing algorithms for public domain software products

The round robin for the glacier area product (Paul et al., 2013) confirmed earlier studies that the results of the various algorithms (band ratio, NDSI) can only be distinguished at the pixel level (e.g. Paul and Kääb, 2005) and that the uncertainties introduced in the post-processing stage are much larger, in particular for debris-covered glaciers. Hence, the algorithm used by the analyst to map glaciers can be freely chosen, but the editing of the outlines has to be performed with great care and improvements at this end have to be in the focus of further efforts. The illustrated guidelines mentioned under (a) will help to increase the consistency in the interpretation. The guidelines will also benefit from the application of coherence images (b) that have a high potential for improving the interpretation of outlines from debris-covered glaciers (e.g. Frey et al., 2012).

The improvement of the geo-location (c) will be a continuous effort at the institutions performing the operational processing of the raw satellite data. Any achievements here will be related to the availability of improved DEMs (e.g. from TanDEM-X) compared to what is currently used (mostly the SRTM DEM in the void filled version from CGIAR). A recent study by Frey et al. (2012) has shown that location shifts of about 3 to 5 pixels can occur in regions where the data voids in the SRTM DEM have been poorly interpolated. This shift results in a considerable mismatch between drainage divides and glacier outlines and a related high workload for manual editing. This workload can be reduced (d) with a better geolocation. Once the related drainage divides are defined (at the correct location), they can be applied repeatedly thus further reducing the post-processing workload (e). It is also faster to remove wrong classifications (e.g. water and seasonal snow) once glacier boundaries are identified (d), for example by applying a one or two pixel sized buffer around all outlines.

A current bottleneck for uploading the generated outlines to GLIMS is the required conversion to the specific GLIMS format (see PSD). When the related workload for the user can be reduced by applying scripts that perform the conversion automatically, data input will certainly increase (e). Such scripts are currently under development for integration of the RGI outlines in the GLIMS database. Finally, the algorithms applied for generating the glacier area product are computationally simple and it should be possible to integrate them also in public domain software products. Though this might not increase their application at the user site, it opens the possibility to provide data processing as a web-based service. This could be a goal in the long-term.

### 3.8 New aspects from the Landsat 8 sensor OLI

With the failure of the Landsat 5 TM sensor in 2012, only the Terra ASTER and Landsat 7 ETM+ sensor continued to provide useful data for glacier mapping on a global scale. However, the ETM+ striping due to the failure of the scan-line-corrector (so-called SLC-off scenes) and the small ground swath covered by ASTER (60 km compared to 180 km for Landsat) limited their applicability. With the successful launch of Landsat 8 and its multispectral sensor OLI in February 2013, the data gap ended and the nearly 30-year time series of Landsat 5 could be continued. The OLI sensor has roughly the same bands as TM and ETM+ (e.g. same spatial resolution), but details have changed. Several new bands are available (e.g. 1 and 9), the panchromatic band has a reduced spectral band width (resulting in a better contrast between ice and rock / vegetation), and all bands have 12-bit instead of the former 8-bit radiometric resolution. To continue the application of the above algorithms also to OLI, we tested if the three algorithms for the initial glacier mapping (BR-RS, BR-NS, NDSI) are still applicable to the 12-bit bands of OLI and what the differences are.

For this purpose we have selected two test regions in Austria/Italy (Ötztal Alps) and Greenland on scenes from Landsat 7 ETM+ and Landsat 8 OLI that were acquired within a week (i.e. they have the same snow conditions). In both regions we tested several parts of the mapping algorithm outlined above:

1. Performance of the three algorithms (BR-RS, BR-NS, NDSI)
2. Influence of the median filter
3. Use of the thermal band
4. Accuracy of the classification provided by the quality image from USGS
5. Quality of the classification in shadow with band 1 (only Greenland test site)

The analysis was performed in comparison to a reference image that was manually corrected for each region and (on a pixel base) included masks for shadow, debris, clouds and the striping in ETM+ scenes. While the latter two masks were subtracted from both image pairs and the reference dataset to have an identical base for the statistical calculations, the former two masks were used to determine mapping quality specifically for these regions. The impact of the median filter was analysed separately for different size classes as previous (qualitative) investigations have shown a stronger impact on small than on larger glaciers.

Classification results (outline overlays) for the first test region are shown in Fig. 3.9 comparing the classification of the red/SWIR ratio (BR-RS) for ETM+ with OLI and the BR-RS vs BR-NS ratio for ETM+. In Fig. 3.10 the related pixel counting statistics are presented for the various tests. How the median filter changes the glacier map under conditions with abundant seasonal snow is shown in Fig. 3.11 and its size dependent influence is shown in Fig. 3.12. For the Greenland test region we compare the ETM+ with the OLI classification in the left part of Fig. 3.13 (ratio red / SWIR) and the shadow classification in the right part of Fig. 3.13. The histograms for the different methods and sensors are depicted in Fig. 3.14.

The outline overlay shown in Fig. 3.9 already reveals very small differences in the raw classification with ETM+ and OLI (94.2 vs 94.3% correct in Fig. 3.10), but the threshold is considerably lower with OLI (1.5 vs 2.7 for ETM+). The red/SWIR ratio performs slightly better than the NIR/SWIR ratio (94.2 vs 93.2% correct) and the median filter increases the number of correctly classified pixels by 0.4% for both ratios. More importantly, the number

of wrongly classified pixels are reduced by 0.6 (red/SWIR) and 1.0% (NIR/SWIR). Classification accuracy is even higher when using the NDSI (94.7% correct) or the thermal band (96.7%) but at the expense of more pixels being wrongly classified (7.2 and 8.2%, respectively). The NIR / SWIR ratio performs less good than the red/SWIR ratio for OLI (94.3 vs 93.8%) in particular regarding the wrongly classified pixels that strongly increase (from 7.9 to 14.3%). Hence, the higher sensitivity and radiometric resolution of the OLI sensor primarily introduces noise. This is also the case for the OLI sensor when using the thermal band: Though classification accuracy is highest and missed debris is lowest, nearly 19% of all pixels are wrongly classified. Only small differences can be seen among the methods in the amount of missed debris-cover and the quality image of Landsat 8 is poor in the amount of correctly classified pixels.

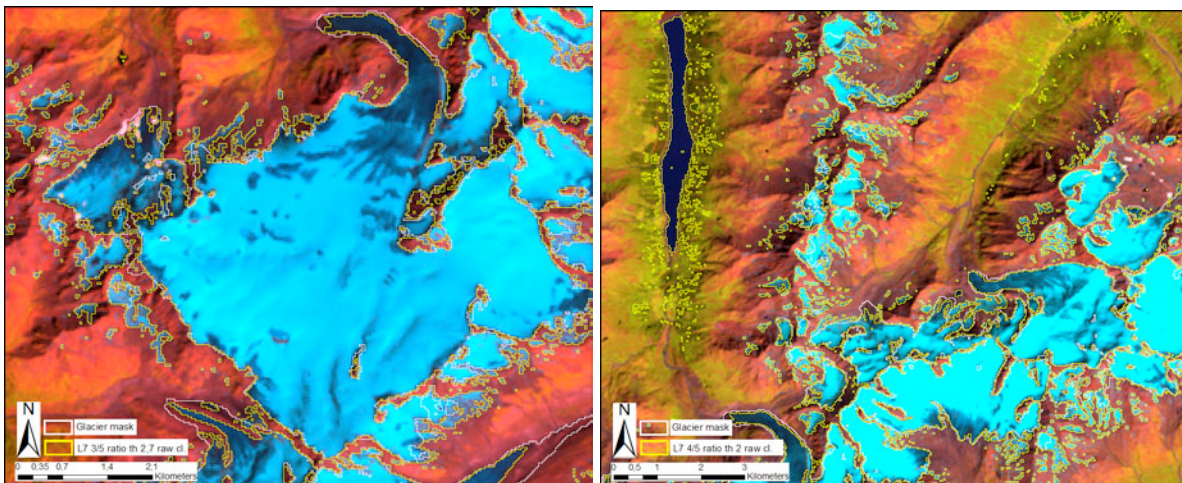


Fig. 3.9: Comparison of glacier outlines derived from the red/SWIR band ratio with ETM+ (black) and OLI (yellow) compared to the reference outlines (white) for the test region in Austria (left). The right image shows the comparison of the red/SWIR (black) and NIR/SWIR (yellow) band ratio with the reference outlines (white).

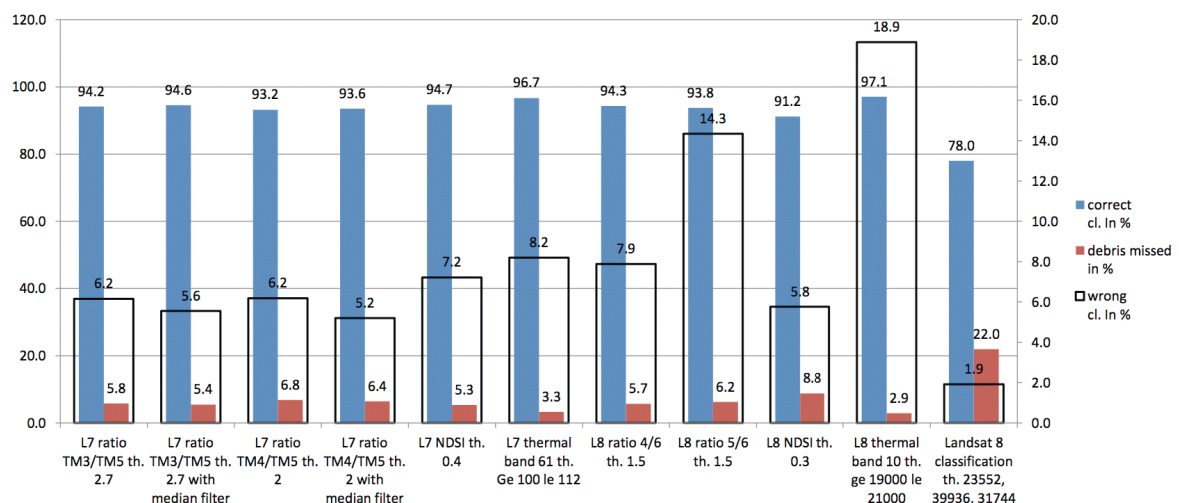


Fig. 3.10: Pixel counting statistics for the various methods and the two sensors for the test region in the Ötztaler Alps.

The impact of the median filter as depicted in Figs. 3.11 and 3.12 is a positive one for all size classes (i.e. increasing the classification accuracy) with the strongest effect on the 0.1-0.5 km<sup>2</sup> size class and a decreasing influence towards larger glaciers and the smallest size class. It can thus be recommended to apply this filter, in particular when snow conditions are not good.

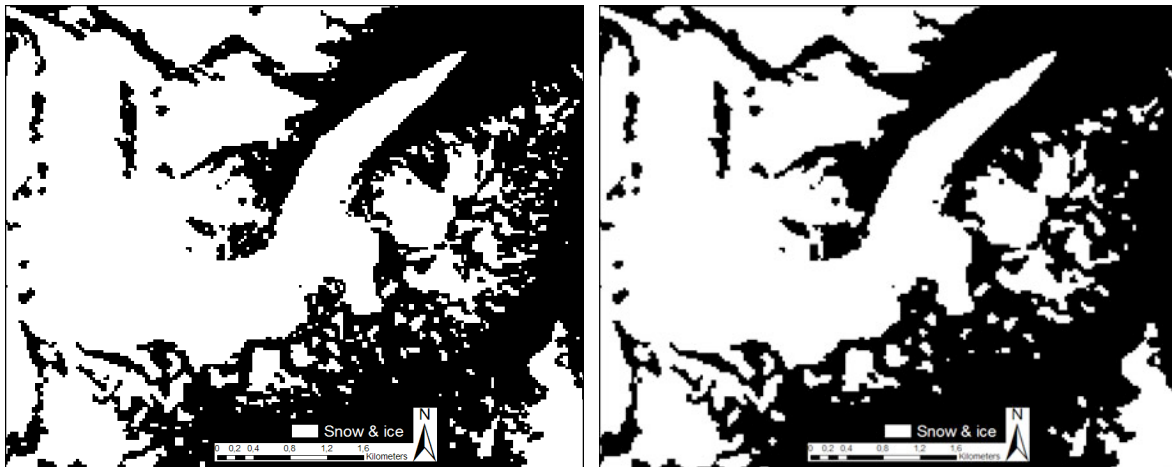


Fig. 3.11 Influence of the median filter for the Hintereisferner region. Left: without median filter, right: after a median filter (kernel size 3 by 3 pixel) is applied.

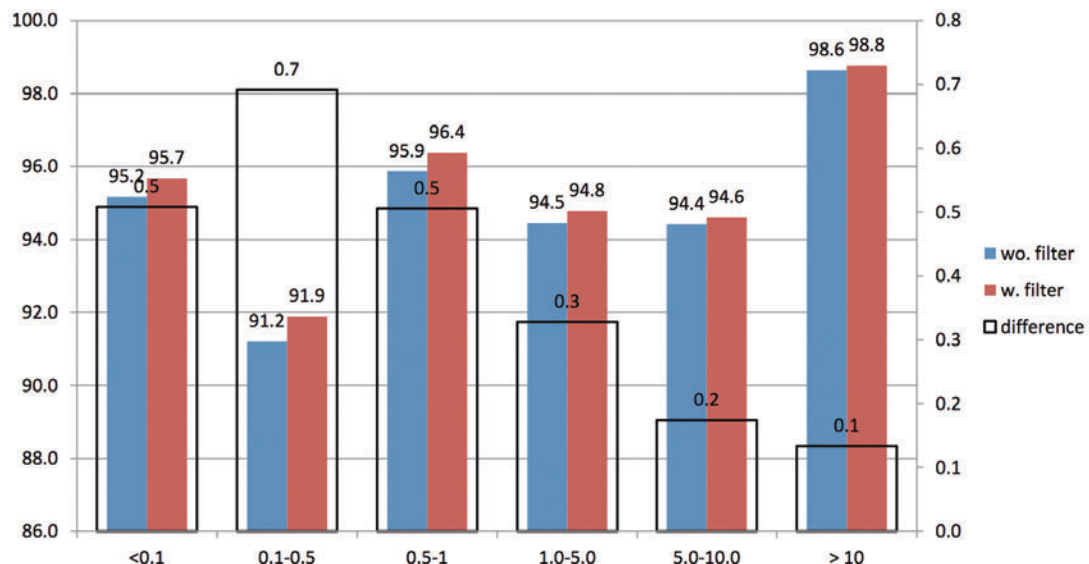


Fig. 3.12: Influence of the median filter (3 by 3 kernel) for different glacier size classes.

The mapping accuracy in cast shadow was investigated in another region due the more extended areas with snow and ice in shadow. The reference shadow mask was created from an ASTER DEM (considering sun azimuth and elevation at the time of image acquisition), converted to a vector outline, and manually corrected. The results are visualized in Fig. 3.13 and statistics are presented in Fig. 3.14.

The main results of this test can be summarized as follows (see Fig. 3.14):

- the ratio red/SWIR is always superior to the NIR/SWIR ratio
- the use of an additional threshold for the blue band only increases the accuracy when the threshold for the band ratio is low
- for the lower band ratio threshold the percentage of wrongly classified pixels increases
- at the same time the mapping of debris-covered regions improves
- the differences in classification accuracy are small when comparing ETM+ to OLI
- the blue band of Landsat 8 (OLI2) provides better accuracy for shadow regions than ETM+, but lower accuracy than without using it (87.6 vs 90.3% for threshold 1.2)
- band ratio thresholds are much lower for OLI than for ETM+ (1.2 vs 2)
- the quality image is less good than the band ratios

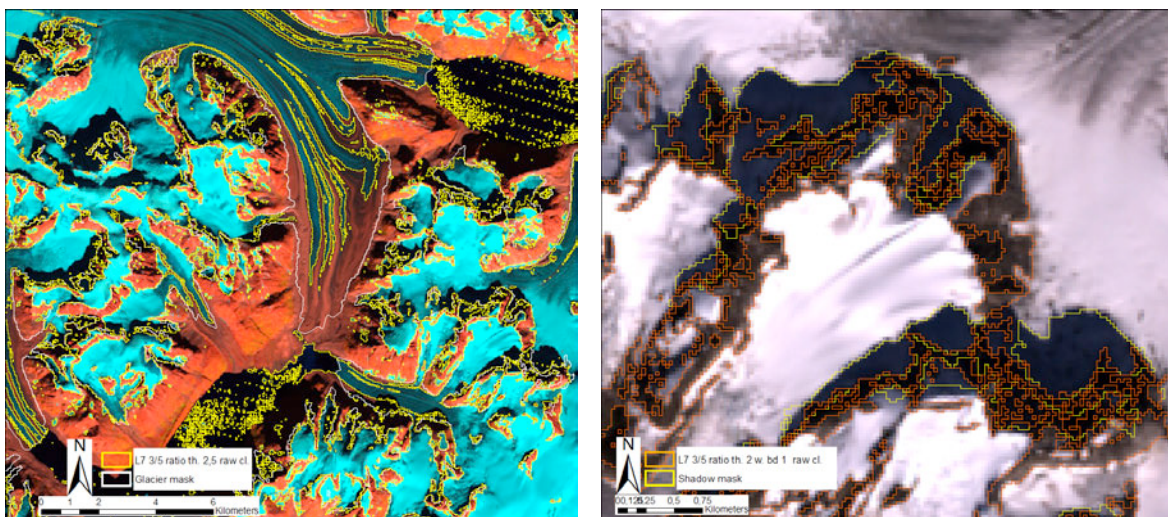


Fig. 3.13: Comparing glacier outlines as mapped with ETM+ (yellow) and OLI (red) using the red/SWIR band ratio to the reference outlines (white) for the test region in Greenland (left). The right image compares the mapped regions in shadow using the same colours.

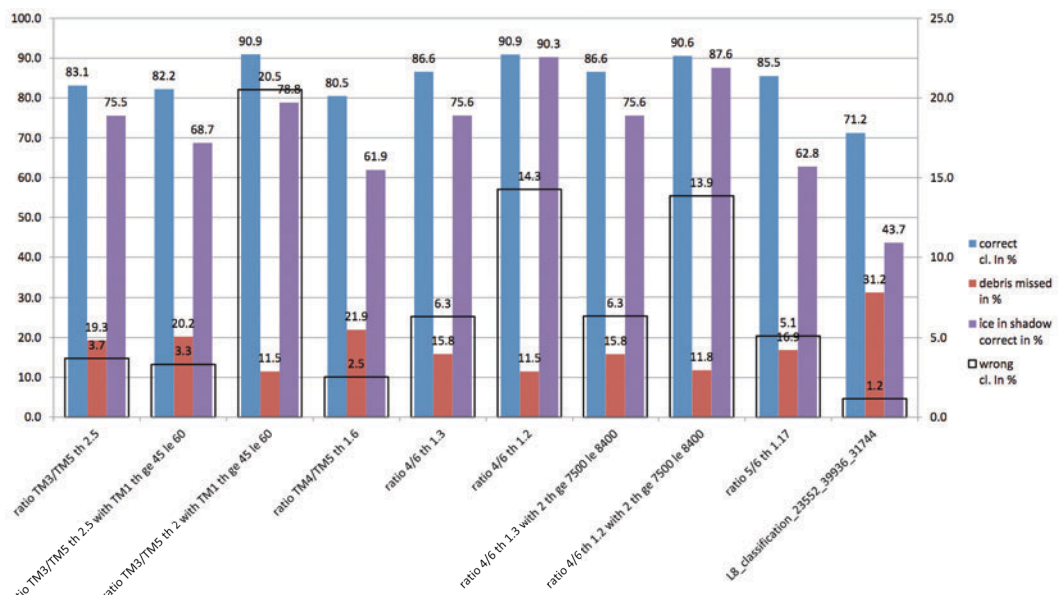


Fig. 3.14: Statistical comparison of the results obtained from different methods for the test site in south-east Greenland.

In conclusion the following general results were obtained:

- the algorithm (band ratios) developed for Landsat TM and ETM+ also work with OLI
- thresholds for the ratio image (using the raw digital numbers) are much smaller for OLI
- the red/SWIR ratio produces better results than the NIR/SWIR ratio
- the additional threshold for the blue band improves classification in shadow only when combined with the lower threshold ratio image
- but the blue band also increases the amount of wrongly classified pixels
- for OLI the additional threshold on the blue band decreases accuracy slightly

In Glaciers\_cci we will thus continue using the red/SWIR band ratio, but decide for OLI on case-by-case basis if the additional blue band threshold improves classification accuracy.

### 3.9 Glacier mapping with Sentinel 2 MSI and Landsat 8 OLI

As the spectral bands that are used for glacier mapping are also available on Sentinel 2 (S2 in the following) and Landsat 8, the algorithms presented in Table 3.1 can also be applied to their sensors MSI (MultiSpectral Imager) and OLI (Operational Land Imager). Due to several extra bands, the classical TM3/TM5 (red/SWIR) band ratio translates to MSI4/MSI11 and OLI4/OLI6 (see Table 3.4). An important difference to TM/ETM+ and OLI is the different spatial resolution of the MSI SWIR band 11 (20 m) compared to the VNIR bands which have 10 m resolution. The general strategy to compensate for the difference is to resample the 20 m SWIR band to the cell size of the 10 m red band using a bilinear interpolation. This allows to make full use of the higher resolution red band which is providing the fine details. As the spectral coverage from the OLI panchromatic band (pan) has been reduced from the range green to NIR to the range green to red (Table 3.4), glaciers show much better contrast in shadow and a band ratio pan/SWIR (OLI8/OLI6) has been tested as well (after bilinear interpolation of the SWIR band from 30 to 15 m). Glacier outlines from this method are directly compared to the classical (30 m) red/SWIR ratio with OLI.

Band	Band Number					Landsat			Sentinel-2A MSI	Terra ASTER
	TM	ETM+	OLI	MSI	AST	TM	ETM+	OLI		
Blue	1	1	2	2	-	0.45–0.52	0.45–0.52	0.45–0.51	0.46–0.52	-
Green	2	2	3	3	1	0.52–0.60	0.53–0.61	0.53–0.60	0.54–0.58	0.52–0.60
Red	3	3	4	4	2	0.63–0.69	0.63–0.69	0.63–0.68	0.65–0.68	0.63–0.69
NIR	4	4	5	8	3	0.76–0.90	0.76–0.90	0.85–0.89	0.78–0.90	0.76–0.86
SWIR	5	5	6	11	4	1.55–1.75	1.55–1.75	1.56–1.66	1.57–1.66	1.60–1.70
SWIR	7	7	7	12	5–9	2.08–2.35	2.09–2.35	2.10–2.30	2.10–2.28	2.15–2.43
Pan	-	8	8	-	-	-	0.52–0.90	0.50–0.68	-	-

Table 3.4: Comparison of spectral band numbers and ranges along with colour coded spatial resolution (black: 30 m, red: 20 m, blue: 15 m, green: 10 m) for five different optical sensors (from Paul et al. 2016).

A direct comparison of the 10 m visible bands from MSI with the 30 m bands from OLI is depicted in Fig. 3.15 for a test region in the Swiss Alps (Lauterbrunnen Valley). The temporal difference between the two acquisitions is only 2 days (S2: 29.8. 2015, OLI: 31.8. 2015) allowing a one-to-one comparison. The most exciting aspect of the 10 m MSI images is

certainly the clear visibility of crevasses that shows even small glaciers to look like glaciers rather than patches of white and grey pixels. This greatly improves image interpretation and will thus result in more accurate products. The latter is also true for the debris-covered lower parts, where now the visual separation of the debris on the glacier from the spectrally identical surrounding bare rock on the eastern side is much clearer (Fig. 3.15). This better visibility will result in a higher quality of the manually edited outlines for debris-covered glaciers.

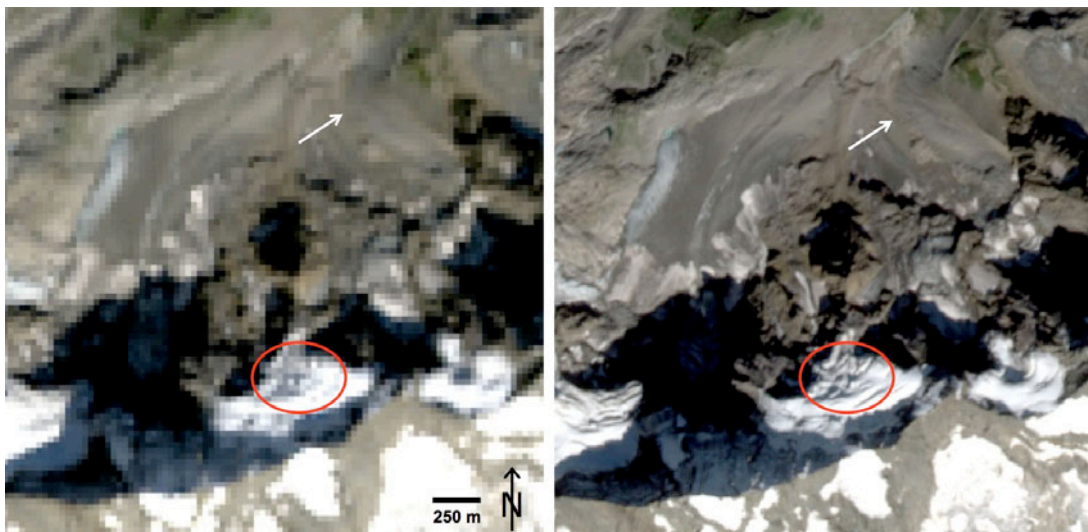


Fig. 3.15: Direct comparison of a small debris-covered glacier in the Swiss Alps as seen with OLI at 30 m (left) and MSI at 10 m (right). The circle marks crevasses that are only visible at 10 m resolution, the arrow is pointing to the glacier margin in a region with thick debris.

Application of the pan/SWIR (OLI) and red/SWIR (MSI) band ratios with various thresholds revealed a very precise mapping with OLI also in regions of shadow (Fig. 3.16, left). However, the threshold is rather sensitive as a change from 1.38 to 1.40 would already remove all yellow pixels from the glacier map. For MSI the red/SWIR ratio also included bare rock in shadow that had to be reduced back to ice in shadow with a further threshold in the blue band MSI2. As shown in previous studies (Paul et al. 2015; Kääb et al. 2016), the blue band threshold is rather sensitive to small changes (i.e. resulting in large changes of the mapped area) and has thus to be selected carefully. For the example shown in Fig. 3.16 (left) a threshold of 2.7 (red/SWIR ratio) and 95 (blue band) has been used to map the glaciers (all colours). When these thresholds are changed to 2.8 and 105 (115), the red (yellow) pixels will be removed and the glacier regions in shadow would be missed.

The overlay of all outlines shown in Fig. 3.17 reveals the overall good agreement of the mapping with both sensors and the two different ratios. In particular the red and yellow outlines derived from 10 m MSI and 15 m OLI are more or less on top of each other and differences are only noticeable at the level of individual pixels. The green outlines from the 30 m OLI bands seem to be a little bit more generous, i.e. are found mostly outside of the other two, in particular in regions of shadow and where debris cover is present. This leads to the conclusion that with 30 m pixels the inclusion of mixed pixels results in a larger glacier area. This might reduce the workload for manual corrections along the glacier margin where even clean ice is often dirty / polluted and would thus be discarded at 10/15 m resolution.

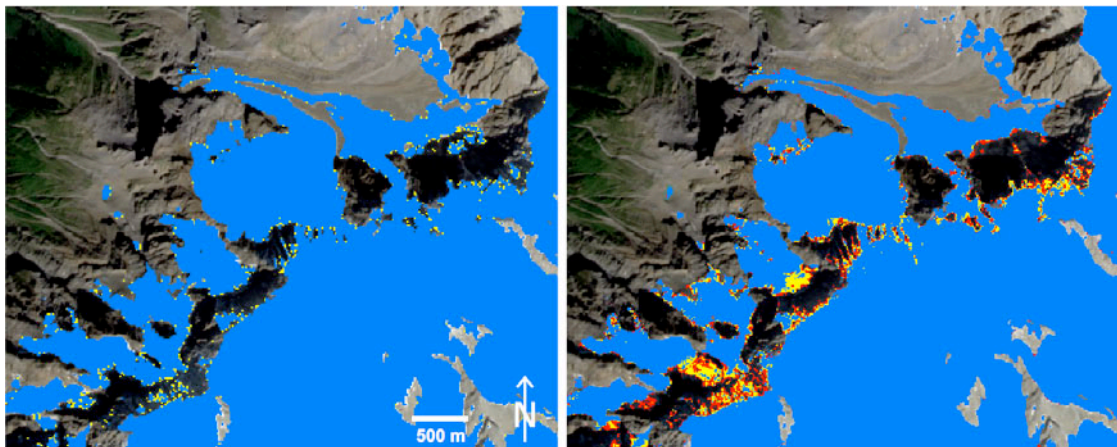


Fig. 3.16: Comparison of glacier extents as mapped with OLI pan/SWIR (left) and MSI red / SWIR (right). Blue (blue and yellow) regions are mapped with a threshold of 1.4 (1.38)

To determine the impact of spatial resolution on the mapped glacier area more quantitatively, we have determined the size of 155 glacier polygons (clean ice and snow only) separately (Fig. 3.18). The scatter plot reveals that area differences increase towards smaller glaciers, extents with the 30 m bands are generally larger, and the outlines using the 10 and 15 m bands are very similar and align around the 0 per cent line. So 15 m extents can be both larger and smaller than 10 m extents. On average, the differences are -0.7% when comparing MSI 10 m to OLI 15 m and -4.8 (-4.2)% for OLI 30 m vs. MSI 10 m (OLI 15 m) bands.

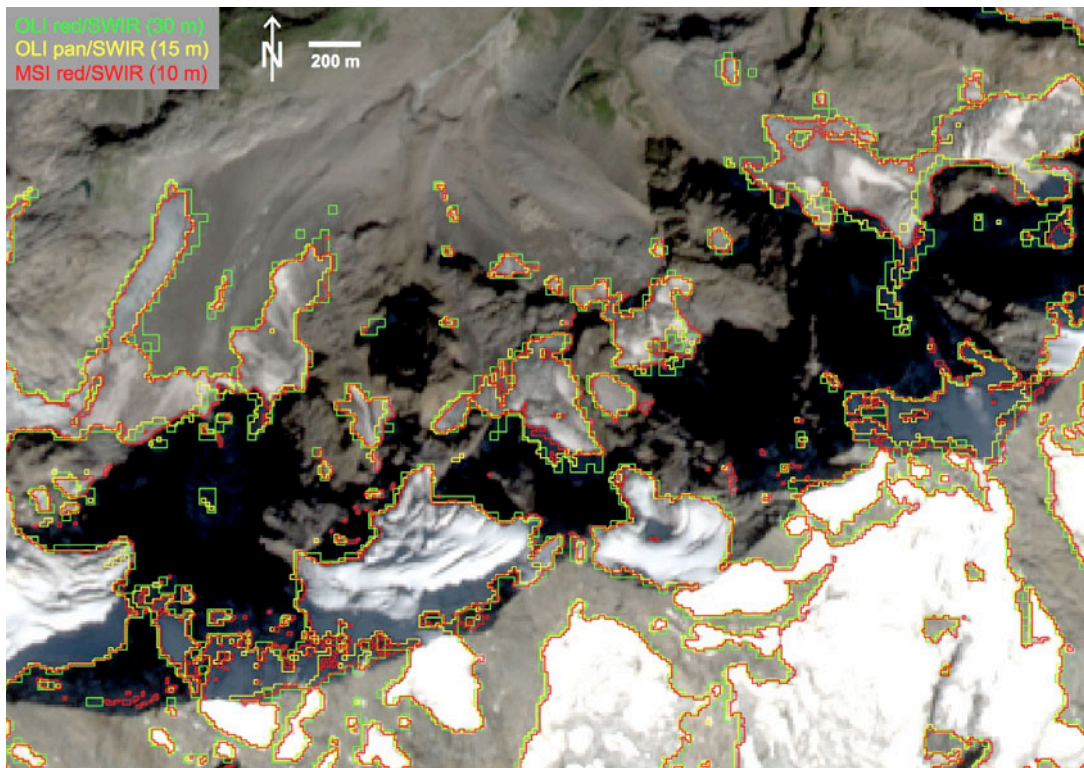
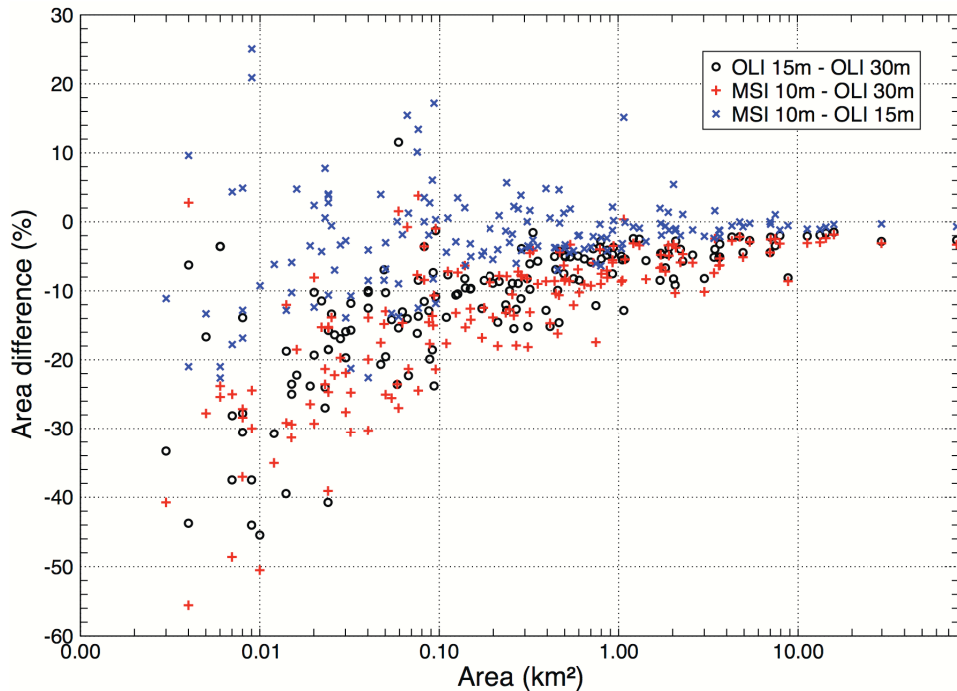


Fig. 3.17: Overlay of glacier outlines as derived from Landsat 8 OLI (red / SWIR and pan / SWIR ratios) and Sentinel 2 MSI (red / SWIR) for the test region depicted in Fig. 3.15.



*Fig. 3.17: Relative area differences vs. glacier area for 155 selected glaciers and the three ratios shown Figure 3.17: OLI 15 m = OLI8/OLI6, OLI 30 m = OLI4/OLI6, and MSI 10 m = MSI4/MSI11.*

We conclude that glacier mapping with Sentinel 2 and Landsat 8 is possible using the same algorithms as before (see Table 3.1), that glacier and debris identification is much improved at the higher resolutions and that henceforth the quality of the derived products should also be higher with MSI and OLI. However, it has to be considered that also the work load for correcting mis-classification will be much higher as dirty ice along a glacier's perimeter might be excluded at the higher spatial resolution. The area difference of about 5% between the 30 and the 10/15 m resolution bands is quite large and needs to be carefully corrected to achieve the same accuracy over 'clean' glacier ice as with the 30 m Landsat TM/ETM+. Further details and examples comparing glacier and snow facies mapping with Landsat 8 and Sentinel 2 are given in Paul et al. (2016). A recent overview by Bhardwaj et al. (2016) summarises sensors and methods to obtain glacier facies, outlines, velocities, hazards and mass balance. Overall, these are more than exciting to increasingly contribute to missing observational data and change assessment.

## 4. Elevation changes from repeat altimetry

### 4.1 Introduction

Repeat satellite altimetry will be used to create surface elevation change products over glaciers and ice caps. The product supplied will be basin scale averages of elevation change measurements and will span the operational time periods of the sensors from which data is to be used (i.e. 2002 onwards). Estimates will be produced using RADAR altimetry data. The objectives of this chapter are to:

- provide a scientific background and theoretical basis of the techniques and algorithms that will be used to generate elevation change maps from RADAR altimetry.
- assess the accuracy of these products
- evaluate the range of applicability and the limitations of the derived data.

A detailed ATBD for laser altimetry was developed and accepted during Phase 1 of the project. This is included here in Section 4.2, with updates to Section 4.2.3 and 4.2.4 to include an additional algorithm for repeat track processing, developed in the latter stages of Phase 1. In Section 4.3 we provide an ATBD for RADAR altimetry; with the inclusion of CryoSat-2 data in Phase 2, this section is new to this document.

### 4.2 Laser Altimetry

#### 4.2.1 Scientific Background

For the wavelengths used by space-borne laser altimetry, the interaction of an electromagnetic wave with clouds and aerosol will be described to understand the main effects which cause attenuation and broadening of the laser beam as it propagates through the atmosphere. Heavy clouds (optical depth > 2 or so) will completely block ground returns, whereas thinner clouds and aerosols cause forward scattering, which is indeed a specific problem for laser altimeters. In the presence of clouds or aerosols in the atmosphere, a part of the signal can be scattered. These scattered photons travel a longer path than photons that pass directly to and from the target. Therefore the mean travel time of the return pulse is lengthened, and the centroid of the pulse is shifted toward a later time (Duda *et al.*, 2001). Forward scattering causes a long tail in the waveform (Fricker *et al.*, 2005), and measurements with such a tail can later be discarded.

##### 4.2.1.1 Review of laser principles

The basic idea of a laser profiler is rather simple. The instrument emits a short pulse of “light” (usually near-infrared radiation) from a downward-pointing laser. At the same instant, an electronic clock is started. The pulse propagates down through the atmosphere, bounces off the Earth’s surface, propagates back up through the atmosphere, and is detected by a photodiode. Detection of the pulse stops the clock, so that the two-way travel time to the surface can be deduced. If the propagation speed is known, the range to the surface can be determined. If the absolute position of the instrument is known, the absolute position of the reflecting point on the Earth’s surface can therefore also be determined.

The spatial resolution of a laser profiler has two aspects: horizontal resolution and vertical (height) resolution. The horizontal resolution is determined fundamentally by the beam width

of the laser. For a laser with a beam width of  $\Delta\theta$  (radians) operating from a height  $H$  above the surface, the horizontal resolution is clearly:

$$\Delta x = H\Delta\theta \quad (4.1)$$

This is often referred to as the laser's footprint.

The vertical resolution is determined by the accuracy with which the two-way travel time can be measured. Assuming that the electronic clock is sufficiently accurate, the accuracy with which the travel time can be measured is governed by the rise time  $t_r$  of the detected pulse (the time it takes to increase from zero to maximum power) and its signal-to-noise ratio  $S$ . For a single pulse, the vertical resolution is given by:

$$\Delta z = \frac{ct_r}{2S} \quad (4.2)$$

where it is assumed that the pulses travel at the speed of light  $c$ . However, laser profilers are pulsed systems and if the pulse repetition frequency (PRF)  $f$  is high enough and the platform speed  $v$  is low enough, a given footprint-sized area on the Earth's surface will be sampled several times. Since each of these samples is independent, and there are  $(f H\Delta\theta/v)$  of them, the vertical resolution when these samples are averaged becomes:

$$\Delta z = \frac{ct_r}{2S} \sqrt{\frac{v}{f H\Delta\theta}} \quad (4.3)$$

Eq. (4.3) indicates the features of a laser profiler's design that will give a high vertical resolution. The rise time of the returned pulse should be as short as possible. This obviously indicates that the transmitted pulse should be as short as possible, but reflection from a rough surface will spread the reflected pulse over time. The signal-to-noise ratio should be as high as possible, which indicates that a large transmitted power is needed, and also that the height  $H$  should be small to reduce losses through absorption and geometrical spreading. The platform speed should be small and the horizontal resolution  $H\Delta\theta$  large, though these considerations are clearly not optimal for other reasons. The PRF should be as high as possible, but there is an upper limit on the PRF. If it is too large, the measurement of the range  $H$  becomes ambiguous because it is no longer possible to identify which return pulse corresponds to which transmitted pulse. The simplest situation is that in which the second pulse is not transmitted until the first pulse has been received, and this implies that:

$$f < \frac{c}{2H} \quad (4.4)$$

**Figure 4.1** sketches the returned laser pulse, which is broadened by the distribution of surface heights within the footprint. The surface height distribution is characterised by a mean surface slope and a surface roughness within the footprint.

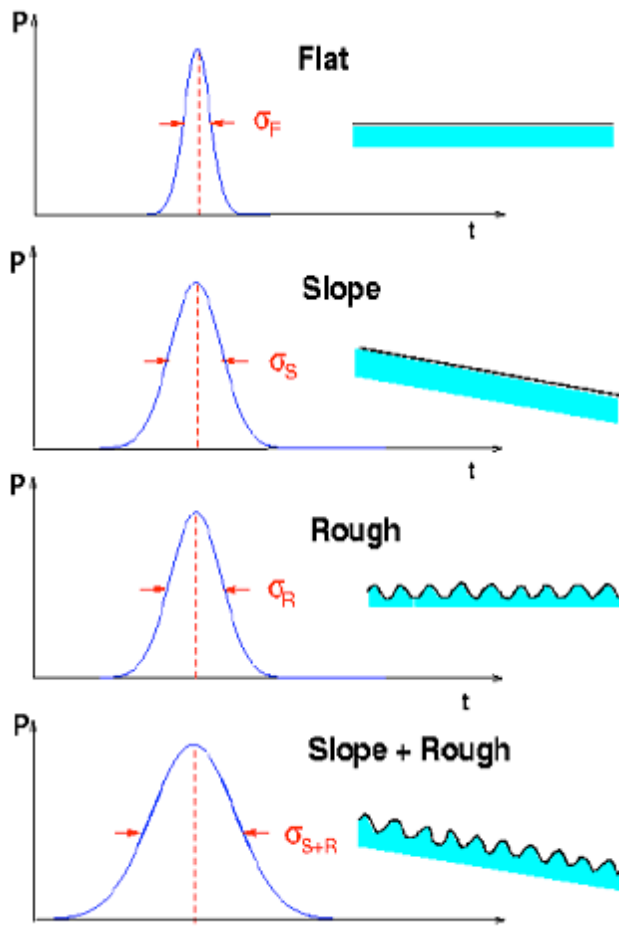


Fig. 4.1: Characteristics of the returned laser pulse as function of surface type. Both, surface slope and roughness broaden the pulse. Sigma ( $\sigma$ ) indicates one standard deviation.

#### 4.2.1.2 Laser beam atmospheric propagation

Many studies have been undertaken for characterising and modelling linear and non-linear atmospheric propagation effects on laser beams. In the following paragraphs, only a brief introduction to the fundamentals of laser beam propagation is presented, with emphasis on those phenomena affecting the peak irradiance at the target.

##### 4.2.1.2.1 Atmospheric transmittance

Attenuation of laser radiation in the atmosphere is described by the Beer Lambert law:

$$\tau(\lambda, z) = \frac{P(\lambda, z)}{P(\lambda, 0)} = e^{-\gamma(\lambda)z} \quad (4.5)$$

where

- $\tau(\lambda)$  is the total transmittance of the atmosphere at the wavelength  $\lambda$
- $P(\lambda, z)$  is the power at the distance  $z$  from the transmitter
- $P(\lambda, 0)$  is the emitted power
- $\gamma(\lambda)$  is the attenuation or the total extinction coefficient per unit of length

If the attenuation coefficient is a function of the path, the Eq. (4.5) becomes:

$$\tau(\lambda, z) = \int_0^z e^{-\gamma(\lambda, z') z'} dz' \quad (4.6)$$

The attenuation coefficient is determined by four individual processes: molecular absorption, molecular scattering, aerosol absorption, and aerosol scattering. The atmospheric attenuation coefficient is:

$$\gamma(\lambda) = \alpha_m(\lambda) + \alpha_a(\lambda) + \beta_m(\lambda) + \beta_a(\lambda) \quad (4.7)$$

where  $\alpha$  is the absorption coefficient,  $\beta$  is the scattering coefficient, and the subscripts  $m$  and  $a$  designate the molecular and aerosol processes, respectively. Each coefficient as shown in the equation depends on the wavelength of the laser radiation. It is convenient to discuss absorption and scattering in terms of the absorption and scattering cross sections,  $\sigma_a$  and  $\sigma_s$ , respectively, of the individual particles that are involved. They are defined as the ratio of the absorbed power to the incident power density and as the scattered power to the incident power density, respectively, and have the dimension of an area ( $\text{m}^2$ ). Thus, it is possible to write:

$$\alpha = \sigma_a N_a \quad (4.8)$$

and also

$$\beta = \sigma_s N_s \quad (4.9)$$

where  $N_a$  and  $N_s$  are the concentrations of the absorber and scatterers, respectively. In the absence of precipitation, the atmosphere contains finely dispersed solid and liquid particles (of ice, dust, aromatic and organic material) that vary in size from a cluster of a few molecules to particles of about  $20 \mu\text{m}$  in radius. Particles larger than this remain airborne for a short time and are only found close to their sources. Such a system, in which a gas (in this case, air) is the continuous medium and particles of solid or liquid are dispersed, is known as an aerosol. Aerosol attenuation coefficients depend considerably on the dimensions, chemical composition, and concentration of aerosol particles. These particles are generally assumed to be homogeneous spheres that are characterized by two parameters: the radius and the index of refraction. In general, the index of refraction is complex and defined as:

$$n = n' - jn'' \quad (4.10)$$

In general, both  $n'$  and  $n''$  are functions of the frequency of the incident radiation. The imaginary part (which arises from a finite conductivity of the particle) is a measure of the absorption coefficient. In fact  $n''$  is related to the absorption by (Ulaby et al., 1982):

$$\alpha = \frac{2\pi}{\lambda} n'' \quad (4.11)$$

For the wavelength in the visible region to about  $15 \mu\text{m}$  the principal atmospheric absorbers are the molecules of water, carbon dioxide, and ozone. Attenuation occurs because these molecules selectively absorb radiation by changing vibrational and rotational energy states. The

two gases present in greatest abundance in the Earth's atmosphere, nitrogen ( $N_2$ ) and oxygen ( $O_2$ ), do not possess electric dipole moment and therefore do not exhibit molecular absorption bands. The  $H_2O$  and  $CO_2$  are by far the most important absorbing molecules. Other absorbing molecules found in the atmosphere are methane ( $CH_4$ ), nitrous oxide ( $N_2O$ ), carbon monoxide (CO) and ozone ( $O_3$ ).

The scattering coefficient  $\beta$  in Eqs. (4.7) and (4.9) also depends on the frequency of the incident radiation as well as the index of refraction and radius of the scattering particle (supposed spherical). The incident electromagnetic wave, which is assumed to be a plane wave in a given polarisation state, produces forced oscillations of the bound and free charges within the sphere. These oscillating charges in turn produce secondary fields internal and external to the sphere. The resulting field at any point is the vector sum of the primary (plane wave) and secondary fields. Once the resultant field has been determined, the scattering cross section can be obtained. As is indicated in [Table 4.1](#), the physical size of the scatterer determines the type of scattering. Thus, air molecules that are typically several angstrom units in diameter lead to Rayleigh scattering, whereas the aerosols scatter light in accordance with the Mie theory. Furthermore, when the scatterers are relatively large, such as the water droplets found in fog, clouds, rain, or snow, the scattering process is more properly described by diffraction theory (Ulaby et al., 1982).

Type of Scattering	Size of Scatterer
Rayleigh Scattering	Larger than electron but smaller than $\lambda$
Mie Scattering	Comparable in size to $\lambda$
Non-selective Scattering	Much larger than $\lambda$

*Table 4.1: Types of atmospheric scattering.*

In the scattering process there is no loss of energy but only a directional redistribution which may lead to a significant reduction in beam intensity for large path lengths. In addition to this reduction, the presence of thin clouds and aerosols produces the multiple scattering phenomenon and consequently a stretching of the laser pulse and the presence of a long tail (Fricker et al., 2005). Scattered photons that pass through thin clouds and aerosols travel a longer path than photons that pass directly to and from the surface, so the mean travel time of the return pulse is lengthened and the centroid of the pulse is shifted toward a later time ([Fig. 4.2](#)). The use of the pulse centroid as the receiver time then produces a biased measurement or an apparent delay in the receive time (Duda et al., 2001).

To calculate the mean path delay accrued by photons, the angular distribution of the scattered energy must be known. This is represented by the scattering phase function. For particles that are large compared to the wavelength of light, diffraction theory shows that one half of the energy is scattered into a narrow forward diffraction peak. A reasonable approximation to this forward scattering peak can be achieved with a Gaussian (Eloranta, 1998). In (Duda et al., 2001), the authors derive the expression of the additional mean path delay based on a phase function given by the sum of a Gaussian forward peak containing one half of the scattered energy with the other half in an isotropic component. [Fig. 4.3](#) shows the average path delay of the received photons as function of mean cloud altitude and particle radius for the ICESat field of view of 475  $\mu$ rad. Large delays are predicted for clouds composed of particles less than 50  $\mu$ m in radius, and for low altitude clouds.

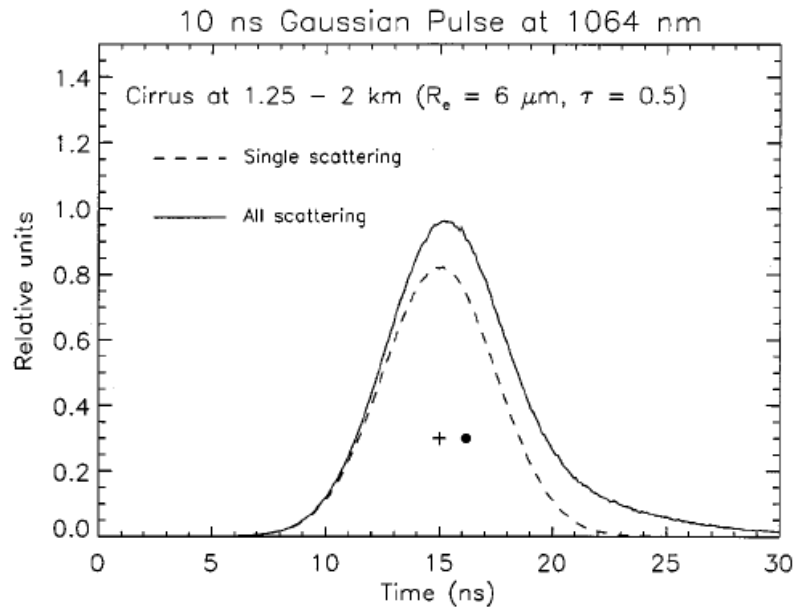


*Fig. 4.2: Plot of a typical simulated GLAS return pulse as a function of time in the presence on cirrus clouds at heights ranging from 1.25 – 2 km, with particle radius  $R_e = 6 \mu\text{m}$  and optical depth  $\tau = 0.5$ . The initial LIDAR pulse was assumed to be not divergent and to have a normal distribution of intensity with a pulse width of 10 ns. The centroid of the singly scattered part of the pulse is shown as a plus sign, and the filled circle indicates the centroid of the entire pulse (Duda et al., 2001).*

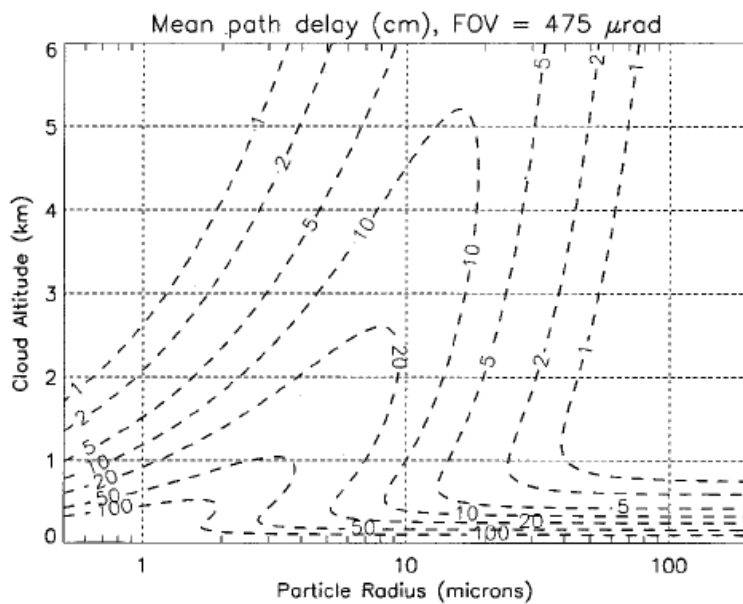


*Fig. 4.3: Mean GLAS path delay (in cm) of doubly scattered photons derived from the analytic model as a function of mean cloud height and cloud particle size. These results assume an optical depth of 0.2 (Duda et al., 2001).*

#### 4.2.1.2.2 Propagation through haze and precipitation

Haze refers to the small particles suspended in the air. These particles consist of microscopic salt crystals, very fine dust, and combustion products. Their radii are less than  $0.5 \mu\text{m}$ . During periods of high humidity, water molecules condense onto these particles, which then increase in size. It is essential that these condensation nuclei are available before condensation take place. Fog occurs when the condensation nuclei grow into water droplets or ice crystals with radii exceeding  $0.5 \mu\text{m}$ . Clouds are formed in the same way; the only distinction between fog and clouds is that one touches the ground while the other does not.

In the early stages of droplet growth the scattering cross section, and consequently the scattering coefficient, depends strongly on the wavelength. When the drop has reached a radius  $a \approx 10\lambda$  the scattering process is now independent of wavelength, i.e., it is non-selective. Since most of the fog droplets have radii ranging from 5 to  $15 \mu\text{m}$  they are comparable in size to the wavelength of infrared radiation. Consequently the value of the scattering cross section is near its maximum. It follows that the transmission of fog in either the visible or infrared spectral region is hampered for any reasonable path length. This, of course, also applies to clouds.

Since haze particles are usually less than  $0.5 \mu\text{m}$ , a laser in the infrared region has  $a/\lambda \ll 1$  and thus the scattering is not an important attenuation mechanism. Rain drops are of course many times larger than the wavelengths of laser beams. As a result there is no wavelength-dependent scattering. The scattering coefficient does, however, depend strongly on the size of the drop. In order to obtain accurate estimates of this parameter, the concentrations of different types of rain drops (radius) and the associated rainfall rates should be known. In this case, the scattering coefficient can be calculated as the sum of the partial coefficients associated to the various rain drops.

#### 4.2.1.2.3 Refractive index variation

When a laser beam passes through air, the randomly fluctuating air temperature produces small density and refractive index inhomogeneities that affect the beam in at least three different ways. Considering for example an initially well-defined phase front propagating through a region of atmospheric turbulence. Because of random fluctuations in phase velocity the initially well defined phase front will become distorted. This alters and redirects the flow of energy in the beam. As the distorted phase front progresses, random changes in beam direction (“Beam Wander”) and intensity fluctuations (“Scintillation”) occur. The beam is also found to spread in size beyond the dimensions predicted by diffraction theory.

The cause of all this, as we have stated, is the atmospheric turbulence that arises when air parcels of different temperatures are mixed by wind and convection. The individual air parcels, or turbulence cells, break up into smaller cells and eventually lose their identity. In the meantime, however, the mixing produces fluctuations in the density and therefore in the refractive index of air. To describe these random processes, one must have a way of defining the fluctuations that are characteristic of turbulence. The most common approaches adopted may be found in Strohbehn, 1978 and Weichel, 1990.

#### 4.2.1.3 Electromagnetic properties of snow in the optical and near-infrared regions

Fresh dry snow appears highly reflective, with little variation over the range of wavelengths approximately from 0.4 to  $0.65 \mu\text{m}$ . The reason for this lies in the dielectric properties of ice,

and the fact that the ice constituting snow is in a very highly divided form with of the order of  $10^9$  particles per cubic metre.

**Figure 4.4** is based on data given by Warren (1984) and collated by Rees (1999), illustrates this in more detail. In ice, the absorption length of visible-wavelength radiation, defined as the distance through which the radiation must travel in order for its intensity to be reduced by a factor  $e$  as a result of absorption alone, is of the order of 10 m, which means that in traversing a snow pack with a thickness of (say) 2 m, containing a total thickness of perhaps 1 m of ice, a photon has a negligible chance of being absorbed. On the other hand, the photon will encounter of a few thousand air–ice and ice–air interfaces as it traverses the pack, with a probability of about 0.02 of being reflected at each of these interfaces. Thus, it is almost certain that the photon will be scattered back out of the snow pack, and since neither the absorption nor reflection properties of ice vary significantly over the visible waveband, this will be equally true for all wavelengths.

This simple argument, which is developed more fully by Rees (2001), also implies that the reflection coefficient of a snow pack should be smaller if the grain size is larger, since the number of air–ice interfaces and hence scattering opportunities will be reduced. Furthermore, the generally increasing absorption (smaller absorption lengths) at longer wavelengths, illustrated in **Fig. 4.4**, implies a corresponding reduction in reflectance at these wavelengths. These phenomena are illustrated in **Fig. 4.5**, which shows the comparative insensitivity of reflectance to grain size in the visible region and the high degree of sensitivity in the range from about 1.0 to 1.3  $\mu\text{m}$ .

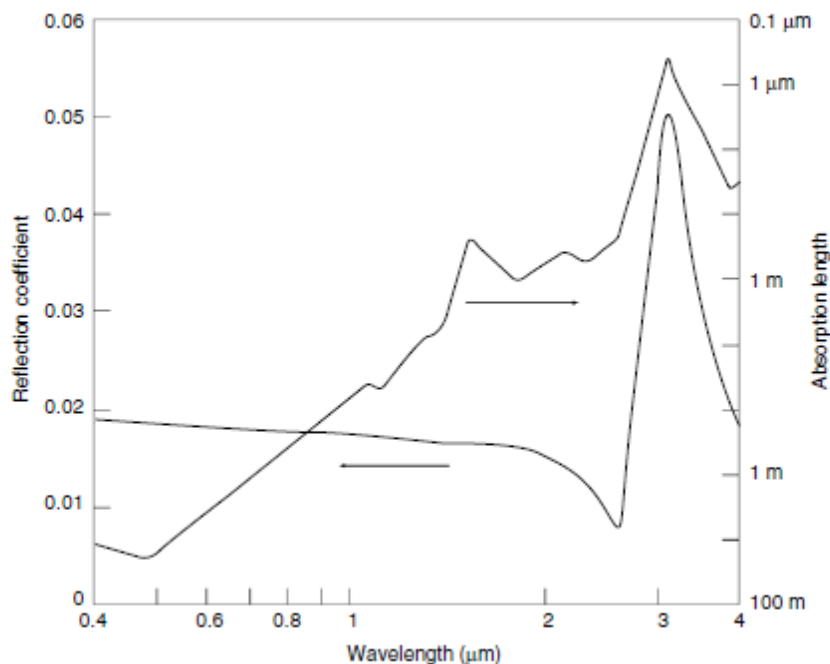


*Fig. 4.4: Reflection coefficient from an ice-air interface (curve identified by the arrow pointing to the left) and absorption length in ice (curve identified by the arrow pointing to the right) for electromagnetic radiation with wavelengths between 0.4 and 4  $\mu\text{m}$  (simplified)*

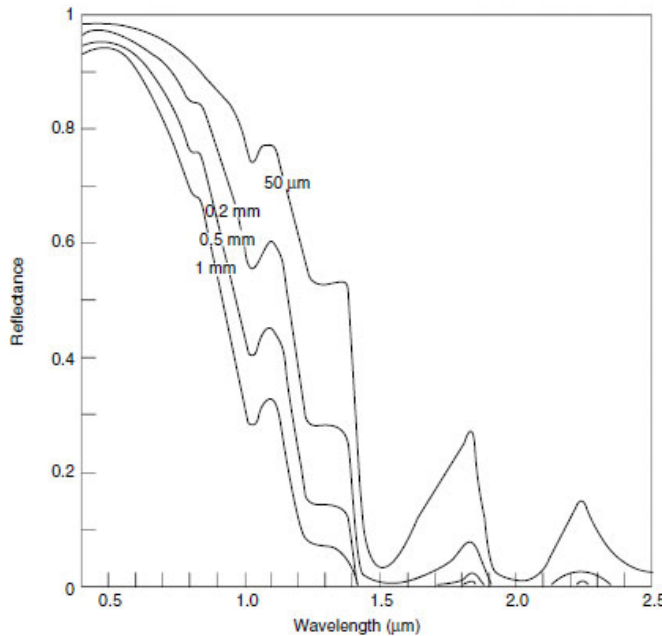


*Fig. 4.5: Spectral reflectance of a deep snow pack as a function of grain size (based on Choudhury and Chang, 1979).*

The reflectance of snow does not depend directly on density, although the processes of compaction by wind and gravity that cause the increase in density over time also lead to an increase in grain size and hence a consequent decrease in reflectance. As a snow pack ages, it may also acquire a covering of dust or soot that may also decrease the reflectance. While the albedo of a fresh snow cover can exceed 90%, this figure can fall to 40% or even as low as 20% for dirty snow (Hall and Martinec, 1985).

It is clear that these arguments apply only if the snow pack is sufficiently thick, since most of the photons encountering a thin pack will travel right through it without being scattered. This phenomenon can be quantified by specifying a scattering length for the snow pack. This is analogous to the absorption length, specifying the distance that radiation must travel through the medium before its intensity in the direction of propagation is reduced by a factor of  $e$  as a result of scattering. The optical thickness of a uniform snow pack is just the ratio of its actual thickness to its scattering length, and is a measure of its opacity. It is proportional to the grain size (radius) and inversely proportional to the snow density. Thus the optical thickness for a given grain size will depend principally on the snow water equivalent.

The presence of liquid water in a snow pack has little direct effect on its reflectance. The amount of water rarely exceeds 10% by volume and there is in any case sufficient dielectric contrast between water and ice to ensure that the multiple-scattering phenomenon continues to occur. The absorption of electromagnetic radiation in water is similar to that in ice in the visible and near-infrared regions. On the other hand, the presence of liquid water does have an indirect effect on the optical properties, since it promotes clustering of the ice crystals leading to a larger effective grain size and hence lower reflectance. Green et al. (2002) present model simulations that take into account both grain size and liquid water content as influences on the reflectance of snow. The most significant effect of increasing water content appears to be a small shift of the absorption feature at 1030 nm to shorter wavelengths.

Reflection from a snow pack is anisotropic (not strictly Lambertian), with enhanced specular scattering due to reflection from ice crystals (Middleton and Mungall, 1952; Hall et al. 1993; Knap and Reijmer, 1998; Jin and Simpson, 1999). However, most studies to date have neglected this effect (Koenig et al, 2001) even though it is rather important in calculating the albedo of a snow-covered surface.

#### 4.2.1.4 Electromagnetic properties of glaciers in the optical and near-infrared regions

In the winter, a glacier surface is usually covered by snow. The optical properties of snow cover have already been discussed in the previous section. In the summer, however, other surfaces can be exposed. [Figure 4.6](#) summarises some experimental data on the spectral reflectance properties of glacier surfaces. The spectra *a*, *c*, *e*, and *f*, for fresh snow, firn, clean glacier ice, and dirty glacier ice, respectively, are adapted from Qunzhu et al. (1984), while the spectra *b* and *d*, for the accumulation and ablation areas of Forbindels Glacier in Greenland, are adapted from Hall et al., 1990. Comparison of curve ‘*a*’ with [Fig. 4.5](#) shows that the snow grain size in this case is about 0.2 mm.

It is possible to note from [Fig. 4.6](#) a general tendency for the visible-wavelength reflectance of a glacier surface in summer to increase with altitude, moving upwards from the ablation area. This is illustrated in [Fig. 4.7](#), which shows the broad-band albedo of the glacier Midre Lovenbreen in Svalbard, measured in situ in summer. At wavelengths longer than about 600 nm the same general trend is observed, although there is greater observed scatter in the results, presumably as a consequence of the greater sensitivity to structural details such as grain size (Winther, 1993) and the quantity and size of air bubbles in ice.

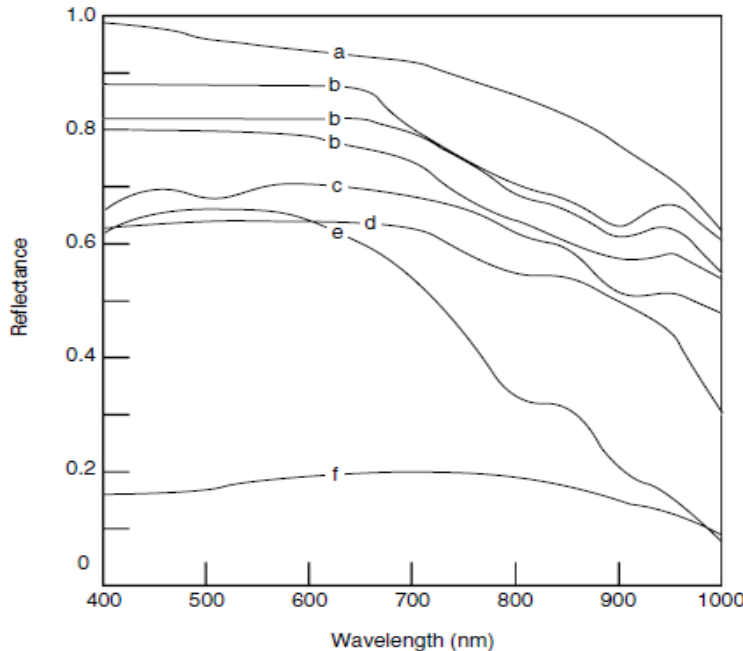


*Fig. 4.6: Spectral reflectance of different glacier surfaces (simplified). a: fresh snow; b: accumulation area; c: firn; d, e: glacier ice; f: dirty glacier ice.*

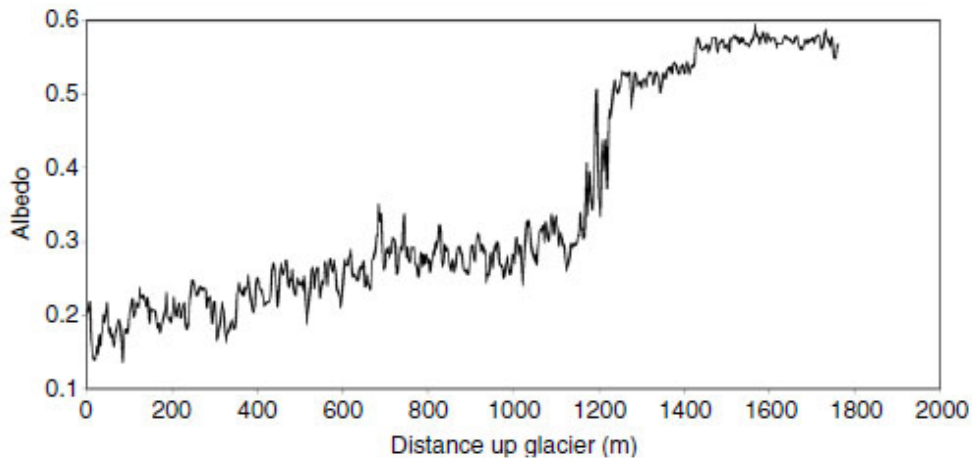


*Fig. 4.7: Longitudinal profile of Midtre Lovenbreen, Svalbard, showing the variation of summer albedo (data supplied by N. S. Arnold, Scott Polar Research Institute).*

#### 4.2.2 Justification on the algorithm chosen

Elevation changes using satellite altimeter data are typically studied with either crossover or repeat track analysis. Both techniques have been described in the ATBDv0 (Glaciers\_cci, 2012a) and were applied during the round robin, using RADAR altimeter data as input of the cross-over method and laser altimeter data as input to the different implementations of the repeat-track methods (cf. Glaciers\_cci, 2012a). The results of the comparison and validation activities are reported in the PVASR (Glaciers\_cci, 2012b). In particular, the limitation of the cross-over method in terms of spatial coverage was quite evident when compared with the repeat-track algorithm. The comparison between the different repeat-track implementations showed a good agreement between them indicating their almost equivalence. From the validation against airborne data, it evidently appeared that due to the large footprint the RADAR altimeter data were not measuring properly the elevation in correspondence of the ice sheet margin where the slope is too high. In addition, the repeat track method applied to laser altimeter data provided estimates of ice cap surface elevation change with significantly better accuracy than the cross-over method applied to RADAR altimeter. As a conclusion, the repeat track method applied to laser altimeter data has been selected as the most reliable technique for developing satellite based observations of ice cap surface elevation change.

It is worth noting that the selected repeat track algorithm, further described in the next section, is also applicable to new Cryosat-2 RADAR altimeter data, which is characterised by a footprint size comparable to the laser altimeter measurements available. Cryosat-2 is the first satellite equipped with a SAR Interferometric Altimeter (SIRAL) to enhance the RADAR's horizontal resolution to 250 m while allowing for precise measurements of changes as small as a few centimetres. Whereas conventional RADAR altimeters send pulses at intervals long enough that the echoes are "uncorrelated" (about 500 µs), the CryoSat-2 altimeter sends a burst of pulses at an interval of only about 50 µs. The returning echoes are correlated and, by treating the whole burst together, the data processor can separate the echo into strips arranged across the track by exploiting the slight frequency shifts, caused by the Doppler effect, in the forward- and aft-looking parts of the beam. Each strip is about 250 m wide and the interval between bursts is arranged so that the satellite moves forward by 250 m each time. The strips laid down by successive bursts can therefore be superimposed on each other and averaged to reduce noise which is known as the SAR mode. In addition, the presence of a second antenna,

which receives the RADAR echo simultaneously, provides a SAR Interferometry capability. Thus, Cryosat-2 is able to identify the location of the echo on sloping surfaces, such as those found around the edges of ice sheets.

#### 4.2.3 Mathematical algorithm development description

Repeat-track analysis is a technique used to detect elevation change rate by comparing elevations from different times along the same repeat portion of a ground-track or spot track from one orbital revolution of the altimeter, also referred to as track segment (Zlotnicki et al., 1989). The track segments will not repeat exactly, so repeat-track analysis is an attempt to reduce the associated errors by estimating parameters that influence the elevation. In an ideal case, ground-tracks or spot tracks for altimeter satellites in repeat-track orbits would repeat exactly so that elevations along the track at one time could be directly compared to elevations along the same track obtained at a different time. However, differences in the altimeter pointing angle and orbital perturbations will cause cross-track differences which should therefore be compensated for within the repeat track analysis.

The unmeasured topography between near repeat-tracks needs to be considered when comparing elevations from different tracks. Several algorithms have been developed for accounting for unmeasured topography when using near repeat tracks. The algorithms selected for Phase 2 are the DEM Subtracting Repeat Track Altimetry Method and the Plane fitting method. These are outlined as follows.

The DEM Subtracting Repeat Track Repeat Altimetry (DS-RT-RepAlt) is based on the use of an external DEM (the best available for the respective region) for correcting the slope effects. It slightly differs from the DP-RT-RepAlt algorithm described in the ATBDv0 (Glaciers\_cci, 2012a). In fact, the algorithm computes the difference between the GLAS measured elevations and the DEM elevations at each altimetry footprint location to assess the elevation change. The DEM elevations at these locations are obtained by interpolating the DEM grid. For a detailed mathematical description it is necessary to introduce an appropriate symbology for representing GLAS measurements, the epoch of acquisitions and the DEM elevation data.

Thus, for the  $i$ -th laser measurement at the acquisition time  $t = t_i^m$ , with  $t_i^m \in [t_{ini}, t_{fin}]$ , where  $t_{ini}$  and  $t_{fin}$  represent the epoch time interval under consideration, the measurement is indicated as a point in a 3D space, where the first two coordinates,  $x_i^m, y_i^m$ , represent the location on the Earth (i.e. latitude and longitude) and the third coordinate,  $h_i^m$ , represents the elevation above the reference ellipsoid (WGS84):

$$P_i^m = (x_i^m, y_i^m, h_i^m)$$

The upper index  $m$  stands for measurements. The same notation is used to indicate the  $j$ -th elevation available from the DEM obtained at the reference time  $t = t_{REF}$ :

$$P_j^{DEM} = (x_j^{DEM}, y_j^{DEM}, h_j^{DEM})$$

As mentioned above, the DEM elevation around the location of the laser acquisition were interpolated to achieve the elevation from the DEM data exactly in such location. Assuming a number of  $k$  DEM elevations available around the location  $(x_i^m, y_i^m)$  and indicating with  $f_{\text{int}}$  the interpolation function, the interpolated elevation can be written as follows:

$$h'_i = f_{\text{int}}(x_i^m, y_i^m; x_1^{\text{DEM}}, y_1^{\text{DEM}}; \dots; x_j^{\text{DEM}}, y_j^{\text{DEM}}; \dots; x_k^{\text{DEM}}, y_k^{\text{DEM}}) \quad (4.12)$$

The difference between GLAS measured elevation and the DEM elevation can be expressed as:

$$\Delta h_{t_i^m - t_{\text{REF}}} (x_i^m, y_i^m) = h_i^m - h'_i \quad (4.13)$$

The differences achieved for each laser footprint are then averaged in order to represent the spatial variation on grid cells of 1 km x 1 km:

$$\overline{\Delta h}_i(x_c, y_c) = \frac{\sum_{k=1}^N \Delta h_{t_k^m - t_{\text{REF}}} (x_k^m, y_k^m)}{N} = \frac{\sum_{k=1}^N h_k^m - h'_k}{N} \quad (4.14)$$

where  $N$  is the number of laser acquisitions within a fixed range distance from the centre of each grid cell,  $(x_c, y_c)$ , and  $t_k^m$  is the time of the each acquisition within the epoch considered, that is  $t_k^m \in [t_{\text{ini}}, t_{\text{fin}}]$ . The sub-index  $\bar{t}$  is the mean time value associated with the averaged difference  $\overline{\Delta h}$ :

$$\bar{t} = \frac{\sum_{k=1}^N t_k^m}{N} \quad (4.15)$$

This procedure is repeated for each ICESat operational period and the elevation trend for each grid cell is determined by fitting a first order polynomial,  $\Delta h(t) = b_0 + b_1 t$ , so that the slope of the polynomial, the coefficient  $b_1$ , represents the elevation trend in the data bin considered (Rinne et al., 2011). Analytically, if  $\bar{t}_i$  represents the averaged time of the  $i$ -th operational period, or epoch, and  $\overline{\Delta h}_i(x_c, y_c)$  is the average difference relative to such time in the grid cell centred around  $(x_c, y_c)$ , the first order polynomial is identified applying the least square method. The best estimation of the coefficients  $b_0$  and  $b_1$  is obtained minimising the sum square error:

$$\min_{b_0, b_1} \sum_{i=1}^M [\Delta h(\bar{t}_i) - \overline{\Delta h}_i]^2 = \min_{b_0, b_1} \sum_{i=1}^M [b_0 + b_1 \bar{t}_i - \overline{\Delta h}_i]^2 \quad (4.16)$$

where  $M$  is the total number of operational period, or epoch.

If we define the cost function  $f(b_0, b_1)$  as follow:

$$f(b_0, b_1) = \sum_{i=1}^M \left[ b_0 + b_1 \bar{t}_i - \bar{\Delta h}_i \right]^2 \quad (4.17)$$

minimising the eq. (4.16) corresponds to solve the following system of equations:

$$\begin{cases} \frac{\partial f}{\partial b_0} = 0 \\ \frac{\partial f}{\partial b_1} = 0 \end{cases} \quad (4.18)$$

whose solutions are:

$$\hat{b}_0 = \frac{\sum_{i=1}^M \bar{\Delta h}_i}{M} - \hat{b}_1 \frac{\sum_{i=1}^M \bar{t}_i}{M} \quad (4.19)$$

$$\hat{b}_1 = \frac{\sum_{i=1}^M \bar{t}_i \bar{\Delta h}_i}{\sum_{i=1}^M \bar{t}_i^2} - \frac{\sum_{i=1}^M \bar{t}_i}{\sum_{i=1}^M \bar{t}_i^2} \frac{\sum_{i=1}^M \bar{\Delta h}_i}{M} \quad (4.20)$$

**Fig. 4.8** is a flow chart for the computational procedure described above.

For rough topography, in particular mountain glaciers, the 1 km x 1 km averaging (Eqs. 4.14 onwards) produces too large uncertainties and typically fails. For these cases, only footprint-wise elevation differences with footprint time will be provided.

The plane fitting method follows that presented by Smith *et al.*, (2009) and McMillan *et al.*, (2014). The method works by taking segments along near repeating tracks and fitting a plane through the elevation points within that plane. In doing so, it is possible to simultaneously solve for slope and elevation change within the segment.

Prior to plane fitting it should be established that the data contained within each segment covers a sufficiently long time period to account for seasonality (i.e. more than a year), and they contain enough points to define a sloping surface. The algorithm for the plane fitting method uses basis vector fitting (least-squares) to fit a plane model surface to the datapoints from a single segment. The plane model surface has a constant slope and varies in elevation across the whole segment linearly with time. The equation for the surface may be written as:

$$z = ax + by + ct + d \quad (4.21)$$

where  $z$  is the elevation of the surface,  $x$  and  $y$  are the Cartesian projections of the longitude and latitude,  $a$  and  $b$  are the coefficients describing the effect of the  $x$  and  $y$  slope components,  $c$  is the coefficient describing the effect of temporal change,  $t$  is the timestamp, and  $d$  is a constant equivalent to the mean elevation at  $t = 0$ .

By converting data point coordinates into Cartesian space and using least square minimisation it is possible to derive the coefficients, residuals and formal 1 sigma errors from the covariance matrix by segment. This will allow clipping of poor data and error estimation.

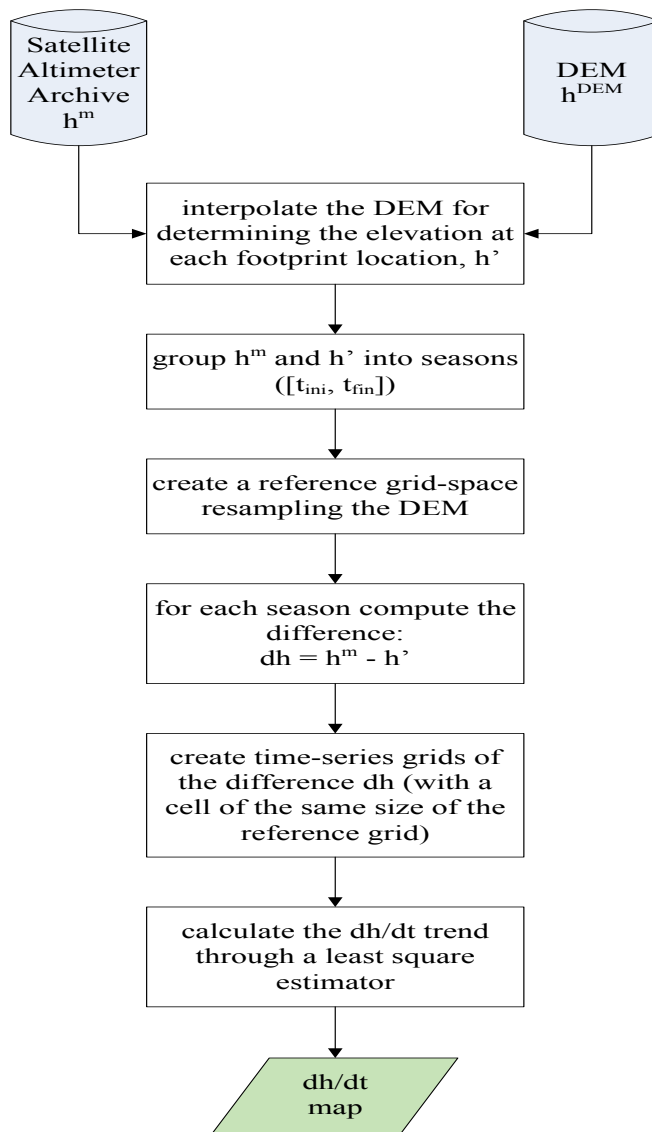


Fig. 4.8: Flow chart of the selected algorithm: DS-RT-RepAlt.

#### 4.2.4 Description of the processing line

Figure 4.9 shows the processing line to apply together with the DS-RT-RepAlt Algorithm. Before starting the processing using either method, the ICESat data archive needs to be filtered to discard data points where no saturation correction was applied and data points with large receiver gain values (greater than 150). A further check before applying the selected

algorithm regards the system reference projection used. In the case of the DS-RT-RepAlt Algorithm the two input datasets, the laser and DEM data, are expressed in two different reference systems then it is necessary to convert them into a common one.

For the DS-RT-RepAlt Algorithm, after the subtraction of the DEM from the elevation measurements, the time series is created taking into consideration measurement density thresholds and statistical filtering, like a 3-sigma clipping, where all the differences  $\Delta h_i$  that deviate more than three times the standard deviation from their mean value are discarded. Eventually a glacier mask is applied to discard all the points falling outside a given ice outline. For the plane fitting method, a glacier mask is applied prior to processing to remove all data points falling beyond the target ice body, and poor data is rejected by iteratively removing data points that give rise to a residual from the plane fit of a magnitude of greater than 5 m.

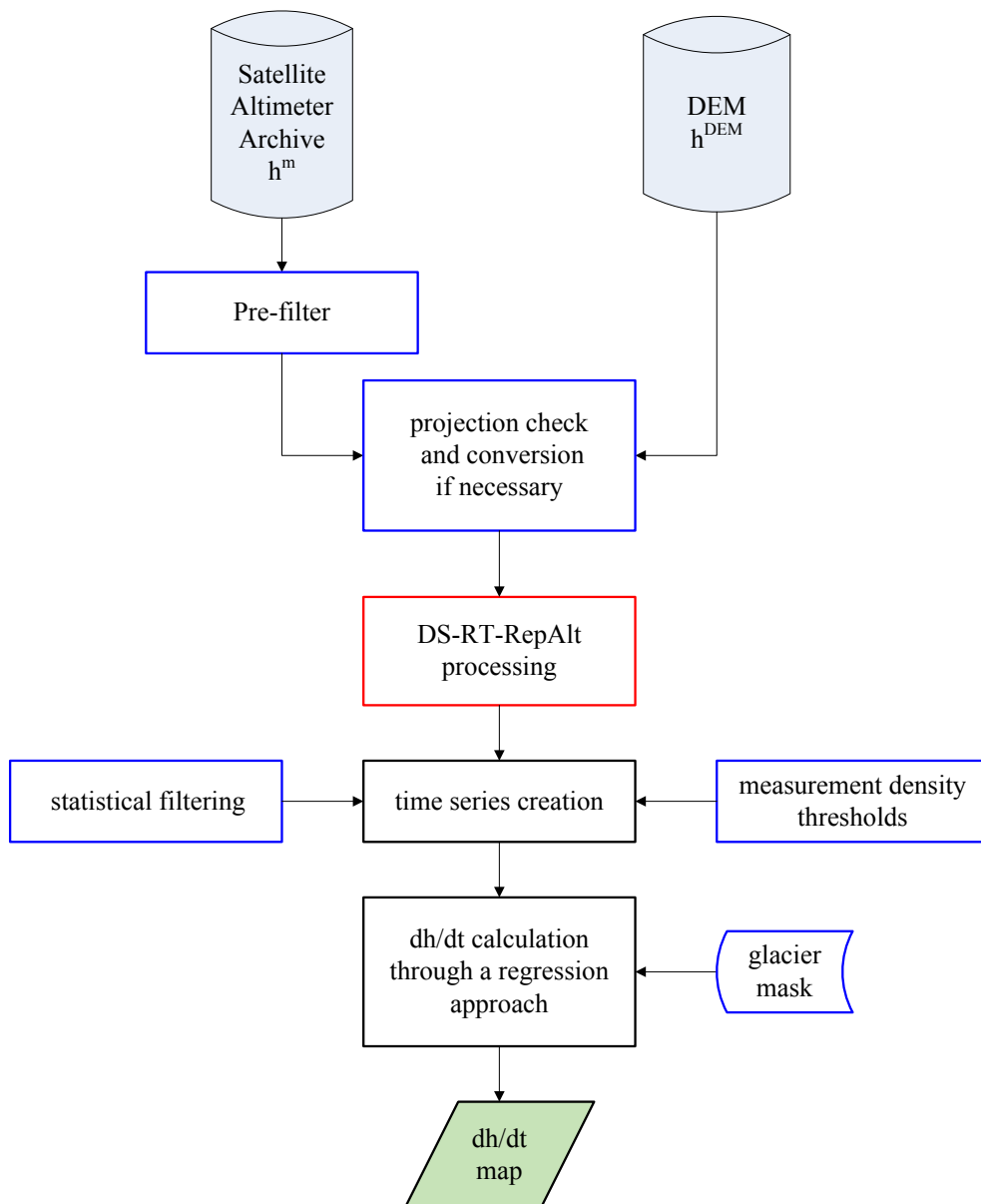


Fig. 4.9: Generalized processing line for the  $dh/dt$  map from altimeter data.

#### 4.2.5 Input data and algorithm output

The input necessary are the ICESat/GLAS measurement and additionally for the DS-RT-RepAlt algorithm, the DEM. The left panel of Fig. 4.10 shows an example of the elevations measured over Devon Ice Cap, which extends approximately over 13700 km<sup>2</sup>. On the right panel the DEM is shown in form of iso-level curves corresponding to increments of 100 m over the same area.

The elevation change is provided on a grid space with resolution of 1 km x 1 km. The elevation trend is associate with the location corresponding to the centre of each grid cell. This information are saved in a ASCII file. Fig. 4.11 shows an example of the elevation change over Devon Ice Cap obtained with the DS-Rt-RepAlt algorithm selected.

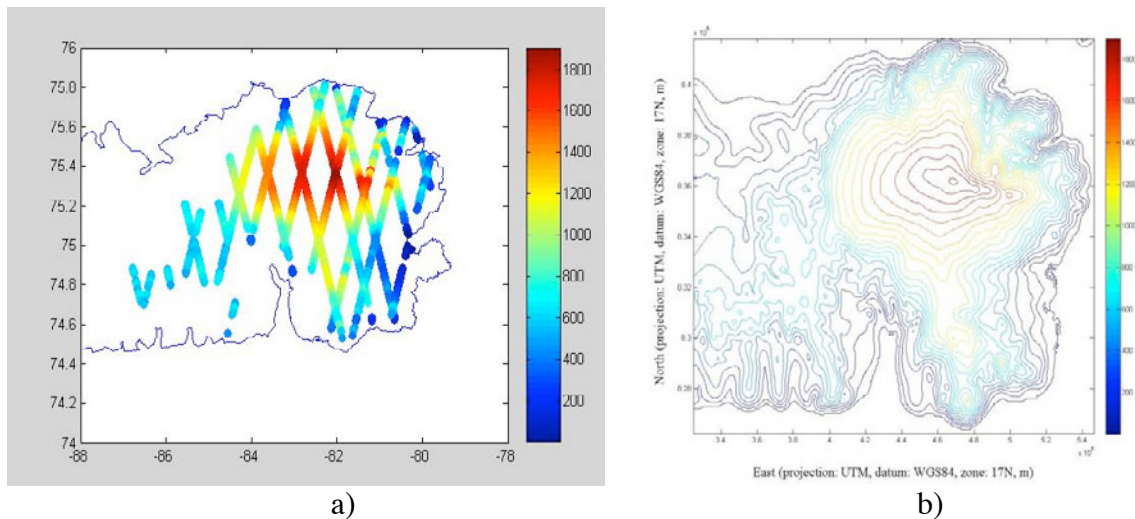


Fig. 4.10: a) Elevation in m obtained using the ICESat/GLAS archive over Devon Ice Cap; b) DEM, the iso-level curves correspond to increments of 100 m.

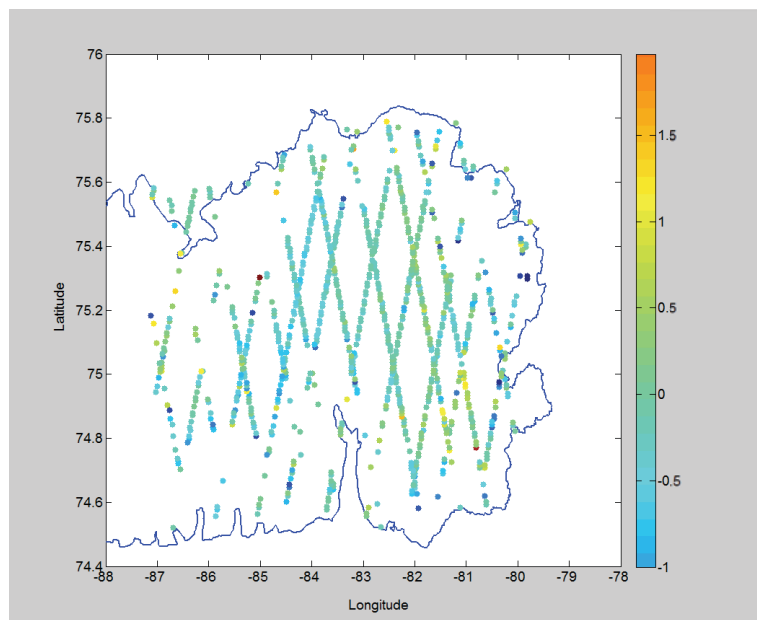


Fig.4.11: Example of  $dh/dt$  (m/yr) output of the DS-RT-RepAlt algorithm over Devon Ice Cap.

#### 4.2.6 Error budget estimates

There are several potential error sources originating from the EO data themselves that have an effect on the surface elevation measured. To achieve the best possible accuracy, the effect of these variables must be compensated for. However, their impact on the results is very small and the required computational effort to determine them is beyond the possibilities of the processor presented here. They are thus mentioned here for completeness only:

- uncertainty in satellite orbit (also known as radial uncertainty) due to gravity anomalies of the Earth as well as the gravity of the Sun and the Moon;
- uncertainty in satellite attitude (roll, pitch and yaw rotations) due to fuel consumption, solar panel orientation and other factors;
- waveform saturation;
- atmospheric propagation effects, i.e. the attenuation introduced by the scattering of water droplets and aerosols, and the multiple scattering phenomenon which causes a stretching of the return pulse and the formation of a long tail;
- Propagation effects due to haze and precipitation;
- Refractive index variation effects (random fluctuations in phase velocity and consequent phase front distortion; redirection of the flow of energy in the beam; intensity fluctuations; beam spreading);
- solid Earth tides due to gravity pull of the Moon and the Sun and to the variations of the Earth's rotation axis;
- ocean loading tides.

For laser altimetry over mountain glaciers using the DEM-differencing method additional error sources become relevant (Nuth and Käab 2011, Käab et al. 2012, Treichler and Käab 2016):

- Biases and spatiotemporal inconsistencies of the DEM used for differencing the altimetric heights;
- Terrain roughness and slope within the footprints;
- Spatiotemporal representativeness of footprint locations and timing with respect to the observed glaciers.

As Glaciers\_cci will, for mountain glaciers, provide un-averaged footprint-wise elevation differences, these error sources cannot be corrected directly. Rather, they will add to the product uncertainty, and will be described in the UCR and PSD with advice on how to handle them should the user wish to average elevation trends.

#### 4.2.7 Practical considerations for implementation

The NGAT software provided by NSIDC is used to open the ICESat/GLAS file and extract the information needed, i.e. the location of the measurements, the elevation, the time of acquisition, the saturation correction, and the gain. Additional scripts (described in the DPM) have to be used for converting the location of the measurements expressed in the geodetic reference system to the DEM reference system.

## 4.3 Radar Altimetry

In addition to dh/dt measurements from ICESat provided in Phase 1, in Phase 2 we will generate dh/dt measurements using CryoSat-2 RADAR altimetry. The following sections describe the algorithm theoretical basis for repeat RADAR altimetry.

### 4.3.1 Scientific Background

Altimeters using microwave frequencies are commonly referred to as RADAR altimetry. At these wavelengths the signal can penetrate cloud cover, making the measurements possible in all weather conditions. In addition, the use of microwaves enables measurements to be made independently from sunlight conditions. The repeat orbits of the satellites with altimeters on board are placed in repeat orbits (cover a region of up to 1 km on either side of a nominal ground track) enabling systematic monitoring of the Earth. Furthermore, satellite altimetry RADARs have been in continuous operation since 1991 and new missions are scheduled for the next decade. There is therefore the availability of long time series and as a consequence the possibility to monitor seasonal to inter-annual variations during the lifetime of these satellites.

Radar altimeters provide a measure of the time of a radio signal to travel from the emitting instrument, reach a target surface, and return/scatter back. The round trip distance from the reflecting target to the RADAR is given by (Elachi, 1988):

$$r = \frac{ct_d}{2} \quad (4.22)$$

where  $c$  is the speed of light and  $t_d$  is the round-trip delay. The accuracy with which the distance is measured is given by:

$$\Delta r = \frac{c}{2B} \quad (4.23)$$

where  $B$  is the signal bandwidth. The operating principle of an altimeter is shown in Fig. 4.13a. Surface elevation  $h$  is calculated as the difference of the satellite altitude  $a$  and the measured range  $r$ :

$$h = a - r \quad (4.24)$$

Surface elevation  $h$  is in relation to the reference ellipsoid used for determining satellite altitude  $a$  (see Fig. 4.12a). In addition to measuring range, the altimeter records a sample of the pulse echo return and estimates other parameters, including the magnitude of the return.

The side view representation in Fig. 4.12b shows the propagation of a single pulse along the beam of the antenna towards a horizontal and planar surface. The curved lines represent the pulse propagating and the temporal width between the curves is constant and equal to  $\phi$ , the duration of the pulse length. A different visualization of the propagation (looking down on the scattering surface from the instrument position) is also provided in Fig. 4.12b (plane view). When the spherical wavefront first hits the surface at the instant time  $t_0$ , the footprint is a

point. The area illuminated by the pulse rises to a circular area until the descending edge of the wavefront reaches the surface, at the instant time  $t1$ . The pulse-limited footprint is the maximum circular area defined as the radius of the leading edge of the pulse when the trailing edge of the pulse first hits the surface. As the pulse propagates, the circle transforms into rings of equal area (Fu and Cazenave, 2001). The figure shows also a typical return waveform. The power received begins to increase from the time when the wavefront hits the surface,  $t0$ , and continues to increase for the duration of the pulse. The waveform presents a linear leading edge corresponding to this initial interaction. At the times greater than the pulse duration, the area intercepted by the pulse remains constant with time. But instead of remaining constant, the power of the reflected pulse actually decreases gradually with time according to the illumination pattern of the antenna. The mid-point of the leading edge corresponds to the range to the mean surface within the pulse-limited footprint.

Information about surface roughness can be obtained from echo-shape analysis. When a pulse scatters from a surface, the returned echo has a shape reflecting the (statistical) properties of the surface. In the case of the ocean, where the surface is homogeneous, the height statistics are the main factors in determining the pulse shape. In the case of terrain, the surface composition varies across the antenna footprint and its statistical properties need to be taken into account. For a perfectly smooth surface, the echo is a mirror image of the incident pulse. If the surface has some roughness, some return occurs in the backscatter direction at slight off-vertical angles as the pulse footprint spreads on the surface. This results in a slight spread in time of the echo. If the surface is very rough, some of the energy is scattered when the radio pulse intercepts the peaks of the surface and more energy is scattered as the pulse intercepts areas at various heights of the surface. This leads to a larger multi-path spread of energy which results in noticeable rise in the echo leading edge. The rise time can be used to measure the surface roughness.

The above described propagation of the pulse in time assumes the forming of the returns is by scattering from the surface only. However it has been shown that ice sheet returns consist of a combination of surface and sub-surface volume scattering due to penetration of part of the RADAR signal through the snow surface (Ridley and Partington, 1988). Volume scattering mainly results from the presence of inhomogeneities in the host medium, like ice grains, air bubbles, and ice inclusions, whose size, shape, density, dielectric constant, and orientation affect the scattering. They cause a redistribution of the energy of the transmitted wave into other directions and results in a loss in the transmitted wave (Ulaby et al., 1982). Signal penetration is largest in the dry snow zone of the ice sheets and exceed 5 m (Davis and Poznyak, 1993; Légresy and Rémy, 1998).

Over ice sheet surface the on-board tracker is generally unable to keep the leading edge of the waveform centred on the tracking point of the waveform window, and a waveform retracking is to be applied to determine this offset. Several methods were developed for retracking ice sheet RADAR altimeter data (e.g. Bamber, 1994; Davis, 1997; Zwally and Brenner, 2001; Legresy et al., 2005). Retracking algorithms are based on defining the point where the waveform exceeds a certain percentage of the maximum power (threshold retrackers) or on functional fits to model waveform shape. All retrackers have their advantages and disadvantages and selection of the retracker will affect taking of topography and volume scattering into account. Functional-fit retrackers more accurately produce individual elevation estimates, while threshold retrackers could be preferred for elevation change studies because it gives more repeatable elevations.

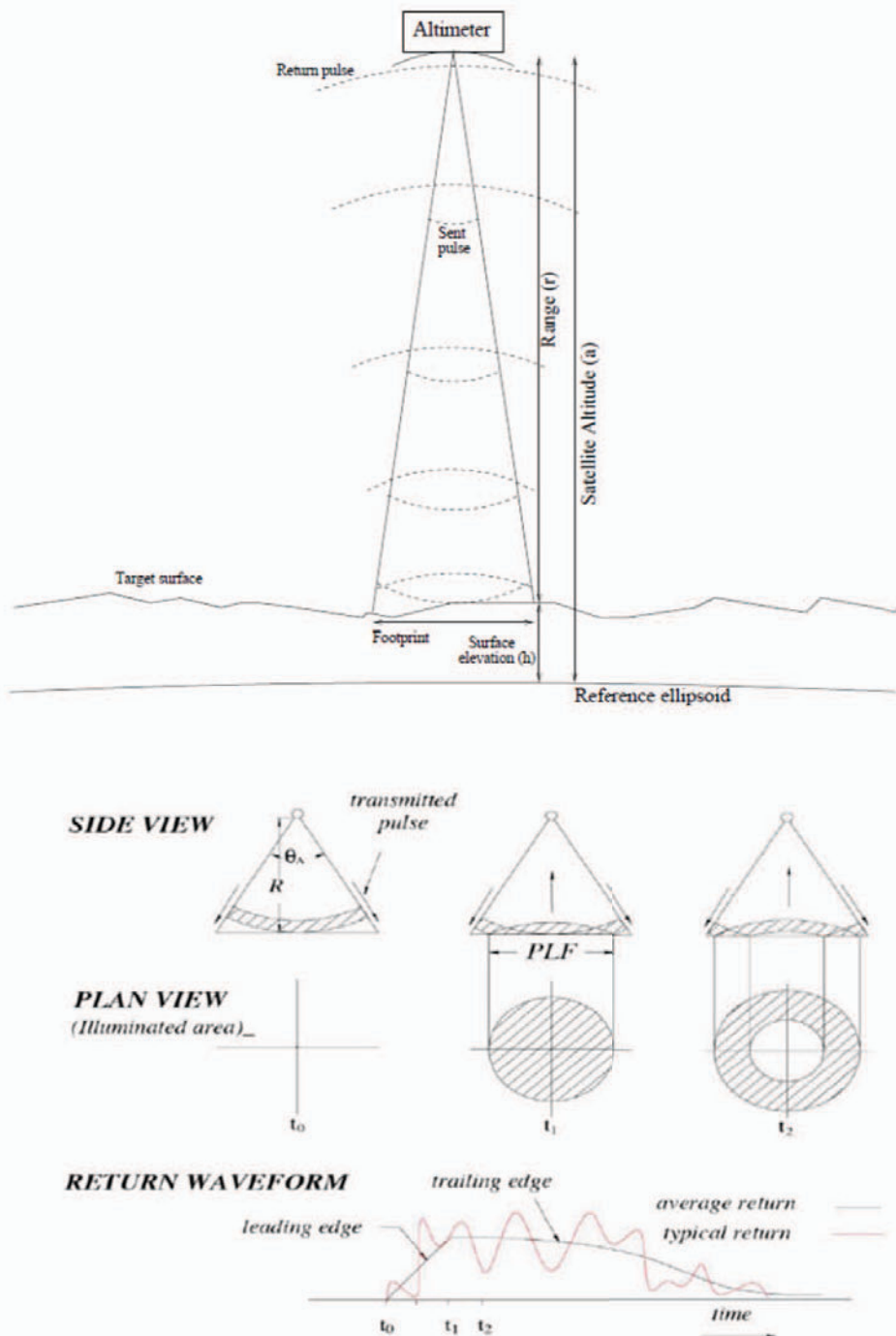


Fig 4.12: Upper panel (a): Altimeter measurement principle. Lower panel (b): The interaction of a RADAR altimeter pulse with a horizontal and planar surface, from its initial intersection ( $t_0$ ), through the intersection of the descending edge of the wavefront with the surface ( $t_1$ ), to the stage where the pulse begins to be attenuated by the antenna beam ( $t_2$ ). The return is from surface only (Ridley and Partington, 1988)

#### **4.3.2 Justification on the Algorithm Chosen**

The algorithm to be used for generating elevation change measurements is the same as the repeat track plane fitting method used for deriving elevation change from ICESat data. For justification please see Section 4.2.2.

#### **4.3.3 Mathematical algorithm development description**

The mathematical algorithm to be used for deriving elevation change from RADAR altimetry is the same as the plane fitting algorithm to be used for estimating elevation change measurements from ICESat. For details of the algorithm please see Section 4.2.3.

#### **4.3.4 Description of the processing line**

Prior to generating estimates of surface elevation change, the elevation measurements must be corrected for the effects of the interaction of the RADAR signal with the atmosphere and the ice/snow surface. As such, in our pre-processing, we will correct the elevation data for the lag of the leading-edge tracker and for variations in the dry atmospheric mass, water vapour, the ionosphere, solid Earth tides and surface scattering (Wingham *et al.*, 2009). All measurements falling beyond the target ice body will also be removed prior to plane fitting. As with the ICESat data, poor data is rejected by iteratively removing data points that give rise to a residual from the plane fit of a magnitude of greater than 5m. Measurements will be averaged over the target ice body.

#### **4.3.5 Input data and algorithm output**

The RADAR altimetry input data required for elevation change measurements are outlined in the DARD. The data output will be average elevation change measurements for each target ice body at seasonal to annual timescales.

#### **4.3.6 Error budget estimates**

We compute the uncertainty of area-averaged elevation trends from the root-sum-square of the uncertainties determined from contributing model fits, as errors associated with altimeter elevation measurements have been shown to rapidly decorrelate with increasing spatial separation (Wingham *et al.*, 1998).

#### **4.3.7 Practical considerations for implementation**

There are no known practical considerations for implementation at this time. These may be added later.

## 5. Elevation changes from DEM differencing

### 5.1 Introduction

This product is a spatially complete grid of elevation change values that can be converted to volume changes and to mass changes if appropriate assumptions of the density of the changed material can be made. DEM differences may be created over time spans of more than about five years to reduce the impact of seasonal fluctuations of glacier surface elevation due to meteorological causes (mass balance processes).

For DEM differencing, the major algorithms presented in this chapter are a part of the **pre-processing** stage. In order to assure that multi-temporal elevation data actually stem from corresponding ground points, i.e. have exactly the same horizontal coordinates in a reference system, elevation data sets require co-registration. This minimizes potential systematic errors (biases). After co-registration, biases may remain related to the acquisition strategy and DEM creation. For example, ASTER and SPOT DEMs have shown to have errors related to pointing inaccuracies of the sensors (Berthier et al., 2007; Nuth and Kääb, 2011). These should be analysed, typically by looking at along track and cross track geometries. However, as these types of biases are sensor or even scene-dependent, they are not considered as uniformly applied in all situations and therefore will remain as a suggested work-flow rather than a defined algorithm in the Glaciers\_cci project.

After co-registration between the DEMs, the main **elevation difference** algorithm is applied by simply differencing the two DEMs. The DEM differences (sometimes called dDEM, differential DEM) have three important error characteristics: voids, noise and bias. At all locations where at least one DEM has a void the dDEM will have a void (no-data value) too. There are many reasons for these voids but all depend primarily on the methods used for DEM generation (e.g. failed correlation for optical stereo, lack of phase coherence for InSAR, perspective obstruction by adjacent terrain, etc.). Secondly, dDEMs are affected by noise or random errors. These are typically evaluated statistically using robust methods to estimate the root sum of squares (RSS), standard deviation, and/or normalized median absolute deviation (NMAD) of the vertical differences between DEMs on stable terrain (Höhle and Höhle, 2009). Last, potential un-removed systematic bias may remain. They can be evaluated if a third dataset is available (e.g. laser altimetry). By performing co-registration between all three datasets, the residual remaining by triangulation of the three co-registration vectors is an estimate of the un-removed systematic bias. Hence, altimetry helps correctly calculating a dDEM while the DEM itself helps to correctly determine elevation changes from altimetry (slope correction). Last, as a **post-processing** step, dDEMs may be filtered or smoothed. This will also be a site/data specific task and thus Glaciers\_cci will not particularly focus on these algorithms. However, resampling to larger grids may be applied by Glaciers\_cci when providing data, to abide by potential copyright laws (e.g. in the case of national DEMs).

### 5.2 Scientific background on DEM generation

Digital Elevation Models are spatially continuous representations of the Earth surface and may be generated using stereo optical images, laser pulse scanning or RADAR interferometry

on either terrestrial, aerial or satellite platforms. This variation of acquisition methods results in a plethora of data that has different attributes. Since *Glaciers\_cci* will focus on the differencing of this type of data, and not specifically on the generation of DEMs, this section will only provide a short overview of the acquisition methods and DEM generation.

### 5.2.1. Stereoscopic DEMs

Stereoscopic DEMs are generated using photogrammetric principles. In along-track stereo, a parallax measurement gives the difference between the projected stereo rays of the same object onto the Earth's ellipsoid and can be converted to height provided the observer positions, the sensor pointing angles and camera parameters are known (Lillesand et al., 2004). Examples of satellite stereoscopic geometries are nadir and backward looking sensors (e.g. ASTER), forward and backward looking sensors (e.g. SPOT-5 HRS), forward, nadir and backward looking sensors (ALOS PRISM), or sensors that can be freely rotated to any stereo geometry (e.g. Ikonos, WorldView, Pleiades), all of which are pushbroom or line scanners.

Satellite stereoscopy is slightly more complicated than traditional photogrammetry from aerial frame imagery due to the typical pushbroom acquisition strategies and to the greater effect of Earth's rotation and curvature from the higher flying height of satellites (Toutin, 2004; Kääb, 2005). Image orientation may be solved from Ground Control Points (GCP) and a satellite orbital model (Toutin, 2004) that is implemented in commonly available software e.g. PCI Geomatica®. Automated approaches are becoming more common for deriving the relative and/or absolute orientation of stereo images using direct measurements of the satellite's attitude and position (i.e. pointing information, auxiliary and ancillary data) (for more details, see Schenk, 1999). Common examples of automatically generated satellite stereo DEMs that are available today include: the ASTER DEMs produced by LPDAAC using the SilcAst software (product AST14) (Fujisada et al., 2005) and the SPOT5-HRS DEMs (Bouillon et al., 2006; Korona et al., 2009), as for instance available through the IPY SPIRIT (SPOT 5 stereoscopic survey of Polar Ice: reference Images and Topography) project.

Errors associated with stereoscopic DEMs are related to the errors in the orientations of the stereo-scenes, either from GCP-based solutions or direct on-board determination, and to the ability of the matching algorithms to locate the corresponding points on two or more images. Errors in the parallax determination are both due to imperfect matching procedures and to imperfect image quality such as from lack of visible contrast, cloud cover, shadows and topographic distortions. Errors related to the parallax matching often result in blunders and voids rather than bias, whereas errors related to the image orientation will typically induce bias. ASTER DEM uncertainty is reported to be typically within 15 to 60 m RMSE in the vertical depending upon terrain type (Toutin, 2002, 2008; Kääb et al., 2002; Hirano et al., 2003; Kääb, 2005; Fujisada et al., 2005) and between 15 and 50 m horizontally (Fujisada et al., 2005; Iwasaki and Fujisada, 2005). SPOT5 uncertainty is reported to be between 10 and 25 m vertically (Berthier and Toutin, 2008; Korona et al., 2009) and greater than 15 m in the horizontal (Bouillon et al., 2006; Berthier and Toutin, 2008). In relation to pushbroom sensors (e.g. ASTER and SPOT5 HRS), it has been shown that variation in the satellite's attitude induces biases within the raw images acquired as well as final DEMs produced (Leprince et al., 2007; Berthier et al., 2007; Nuth and Kääb, 2011).

### 5.2.2. Interferometric DEMs

Interferometric DEMs are generated through synthetic aperture RADAR (SAR) interferometry which uses the phase differences between two RADAR images acquired with a small

base-to-height ratio. These phase differences are the photogrammetric equivalent to a “parallax” measurement allowing retrieval of topography (Rosen et al., 2000). Examples include the SRTM DEM, acquired in February 2000, which mapped the Earth from 60° N to 56° S using single-pass SAR interferometry (Farr et al., 2007), and the ongoing TanDEM-X Mission.

Many glacier elevation change studies have used the SRTM as a base dataset to compare to both newer and older data products (Rignot et al., 2003; Larsen et al., 2007; Schiefer et al., 2007; Paul and Haeberli, 2008). Typically reported vertical uncertainties of the dataset are ±10m which is lower than the mission standards of ±16m (Rodriguez et al., 2006). However, vertical biases are present due to instability of the sensor and/or platform (Rabus et al., 2003), and elevation-dependent biases have also been shown due to penetration of the C-band RADAR waves (centre frequency at 5.3 GHz) into snow and ice (Rignot et al., 2001; Berthier et al., 2006). Rignot et al. (2001) determined that the phase centre of the C-band signal return was 1 to 10 m into the surface depending upon the snow conditions (i.e. wet vs. dry) in Greenland and Alaska. In Svalbard, the volumetric phase centre of the C-band varied from 1 to 5 m along a profile from ablation to firn zones, respectively (Müller, 2011). Corrections for depth penetration are hardly used for the SRTM data, and it is extremely difficult to correct for as knowledge of the snow conditions at the time of acquisition is required but generally not available. Nonetheless, this bias is crucial to understand when interferometric DEMs are used in differencing. Future potential in determining this bias may entail the comparisons between the C-Band and X-Band SRTM datasets (e.g. Gardelle et al., 2012).

### 5.2.3. Laser scanning DEMs

DEM generated from laser altimeters are at the present time typically restricted to airborne platforms and are therefore less widespread than satellite based DEMs. However, their accuracy is unprecedented and therefore provide great potential for glacier elevation changes (Geist et al., 2003; Geist et al., 2005; Aberman et al., 2010). Elevation acquisition from laser pulses is described in section 4.3.2. Laser scanning uses the same principles but collects data not only along a profile (as ICESat), but also across track (swath). Depending upon the flying height and sampling frequency, airborne laser scanners can typically acquire a horizontal point density on the order of 1-2 metres. The accuracy of the returned elevations are typically a function of the accuracy of the laser range determination and of the GPS position of scanner through time. Laser scanning DEMs are not globally available, and are only used as a secondary DEM source for those particular glaciers from which they are available.

## 5.3 Elevation changes from multi-temporal DEMs

Glacier elevation changes can be derived from multi-temporal DEMs through differencing. DEM differencing provides a more-or-less complete spatial representation of the glacier changes in height (provided no data voids), but has a coarse temporal resolution. This is because a greater time between data acquisitions is required to estimate significant changes due to the accuracy of the DEMs and due to seasonal elevation variations of the glacier surface as a result from accumulation and ablation. To compensate for both DEM accuracy and natural seasonal height variability, glacier elevation changes from DEM differencing are typically derived as long-term averages (i.e. >5 years). However, the time period required between successive DEMs is strictly dependent upon the accuracy of the DEMs and the magnitude of the changes, and therefore will not be standardized within Glaciers\_cci.

Glacier elevation changes are used for analysing changes in the geometry of glaciers (Hagen et al., 2005) and for estimating volume and mass changes (Käab, 2008; Berthier et al. 2010; Nuth et al., 2010), and possibly their relation to climate. However, the estimation of volume and mass changes requires some standard assumptions about the density of the changes, which is difficult and rarely measured. Furthermore, an elevation change at a point on a glacier is the result of both climatic (surface mass balance) and dynamic (glacier flow) processes, and therefore a direct translation into responses induced by climate change is difficult. This is sometimes made easier when integrating all changes over individual glaciers (i.e. mean elevation change thickness) as the dynamic component of ice submergence and ice emergence cancels due to mass conservation within a land terminating glacier system. For these land terminating glaciers, this has led to a large effort to control field derived surface mass balances of glaciers (Andreassen, 1999; Elsberg et al., 2001; Cox and March, 2004; Thibert et al., 2008), but also to provide control and calibration for surface mass balance models (Huss et al., 2009). However, if the glacier is marine terminating and contains ice loss to calving processes, the mean elevation change will include both the surface mass balance component as well as the component related to the calving loss of ice. In some instances, glacier elevation changes from DEM differencing have been combined with surface mass balance modelling to estimate the calving component to volume change (Nuth et al., 2012). In summary, the algorithms presented for DEM differencing focus on the **pre-processing** and generation of elevation changes, rather than the translation of elevation changes into volume and mass changes, which require several assumptions. This latter step is the focus of Option 2, which has a focus on the extrapolation of spatially incomplete elevation change measurements (e.g. due to data voids for DEM differencing) to entire glaciers.

While the approach of DEM differencing is straight-forward (i.e. subtraction of the older DEM from the newer DEM), the results of this differencing can be misleading due to bias in one or both of the DEMs and to the geometric co-registration of the DEMs to each other. DEMs can be generated from optical, RADAR or LIDAR data, and therefore variation in the errors and biases in any of these products may propagate into the elevation changes. Thus, the goals in terms of algorithms will be to outline the best procedures for (1) combining the various datasets and (2) for detecting and correcting (if possible) potential biases between the datasets. Further, we aim for universal procedures that can be highly automated and are flexible for the various input data sources used to generate differential DEMs.

## 5.4 Description of the algorithm chosen

### 5.4.1 Justification on the algorithm chosen

For DEM differencing, the elevation change algorithm is simply subtraction of the two grids and therefore requires little attention. The main algorithm for DEM differencing is for horizontal and vertical co-registering of the DEMs. This algorithm (DEM CR) was discussed in the ATBDv0 (Glaciers\_cci, 2012a) and investigated together with other approaches during the round robin. In conclusion of the round robin and as documented in the PVASR (Glaciers\_cci, 2012b), the co-registration algorithm presented in the ATBDv0 is found to be the most robust and efficient algorithm with similar reliability to other published approaches and thus is the most appropriate for Glaciers\_cci. In addition, the analytical basis of the algorithm allows consistent application for multiple data types and sources in which the other algorithms experienced slightly worse reliabilities.

### 5.4.2 Algorithm overview

One of the DEMs will have to be re-sampled to the cell size of the other DEM. Any resampling technique more advanced than nearest neighbour (NN) should be used (i.e. bilinear interpolation), because NN resampling, though retaining the original measurements, will inherently compare ground elevations representing different locations and areas (pixel sizes). Therefore, despite the smoothing of higher order interpolations (e.g. bilinear), these methods are necessary to ensure comparison of similar ground locations and areas in order to limit the effect of mis-registrations on DEM differences. We here focus on the pre-processing steps to improve the accuracy (remove bias) and precision of DEM differencing measurements.

The accuracy of glacier elevation differences from multi-temporal DEMs is dependent upon the individual accuracies of each of the DEMs and the geometric alignment between the DEMs. For DEMs that contain sufficient non-glacier terrain (e.g. > 10% of the scene), DEM difference statistics in this terrain, assumed stable within the time period, can be used for co-registration and bias-assessments. The initial (and universal) pre-processing step for deriving glacier elevation changes from DEM differencing is thus co-registration of the DEMs to each other. After co-registration, higher order biases can be investigated and removed if possible.

### 5.4.3 Mathematical description

Two DEMs of the same terrain surface that are not perfectly aligned experience a characteristic relationship between elevation differences and the direction of the terrain (aspect) that is precisely related to the x-y-shift (co-registration) vector between them. Fig. 5.1 shows a schematic drawing and a real example where one DEM is shifted to the second. Resulting elevation differences ( $dh$ ) are larger on steeper slopes due to the relationship of the magnitude ( $a$ ) of the shift vector and the elevation errors to the tangent of the slope of the terrain ( $\alpha$ ):

$$\tan(\alpha) = \frac{dh}{a} \quad (5.1)$$

For the assumed shift in x-direction,  $dh$  is positive on eastern and negative on western slopes, exemplifying the relationship between the shift direction and terrain aspect ( $\Psi$ ). Because  $\Psi$  is usually defined circular from the north (azimuth), the direction of the shift can be modelled using a cosine of the difference between  $\Psi$  and the horizontal directional component of the co-registration vector. Combining this with the relation described by Eq. 5.1 derives the full analytical solution by relating the elevation differences to the elevation derivatives slope and aspect (Kääb, 2005):

$$dh = a \cdot \cos(b - \psi) \cdot \tan(\alpha) + \bar{dh} \quad (5.2)$$

where  $dh$  is the individual elevation difference,  $a$  is the magnitude of the horizontal shift,  $b$  is the direction of the shift vector,  $\alpha$  is the terrain slope,  $\Psi$  is the terrain aspect and  $\bar{dh}$  is the overall elevation bias between the two DEMs. Slope and aspect can be calculated by any standard GIS or mathematical software, and different approaches exist depending upon application. In this case (photogrammetric DEMs), the finite difference method is more appropriate than the D8 method, but for other DEMs (e.g. derived from contour lines) it might be vice versa (cf. Wilson and Gallant, 2000). To remove the error dependency on slope due to a geometric mis-registration, we normalize the vertical deviations by dividing by the tangent of slope at that pixel. This produces a clean sinusoidal relationship between elevation difference and aspect (Fig. 5.2). The transformation of Eq. 5.2 after slope normalization is:

$$\frac{dh}{\tan(\alpha)} = a \cdot \cos(b - \psi) + c \quad (5.3)$$

where:

$$c = \frac{\bar{dh}}{\tan(\bar{\alpha})} \quad (5.4)$$

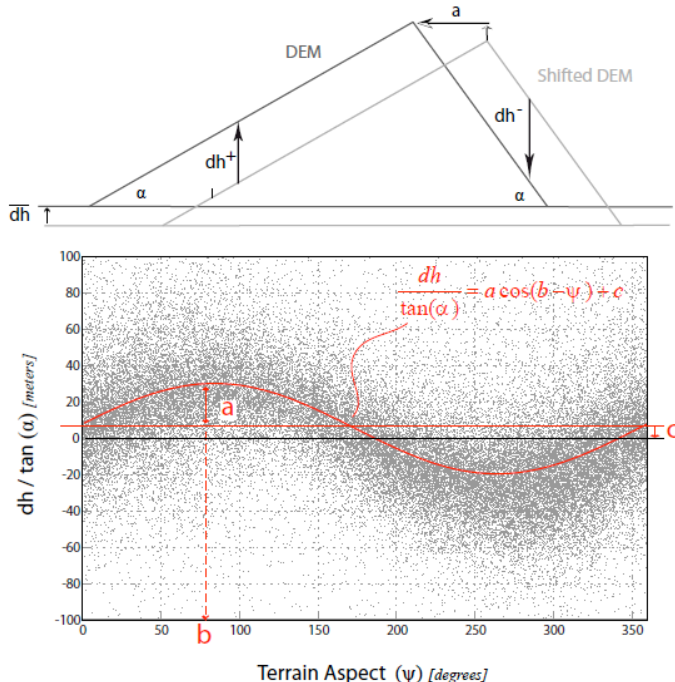


Fig. 5.1: Top: 2-D scheme of elevation differences induced by a DEM shift. Bottom: The scatter of elevation differences between two DEMs showing the relationship between the vertical deviations normalized by the slope tangent (y-axis) and terrain aspect (x-axis). The equation for the solved sinusoidal curve fit is shown along with the three unknown solution parameters  $a$ ,  $b$  and  $c$ . Reproduced from Nuth and Käab (2011).

Three cosine parameters ( $a$ ,  $b$  and  $c$ ) are solved using robust least squares minimization where the amplitude of the cosine ( $a$ ) is directly the magnitude of the shift vector,  $b$  is the direction of the shift vector and  $c$  is the mean bias between the DEMs divided by the mean slope tangent of the terrain. Because the solution to this analytical relationship is solved using the terrain which is not an analytical surface, the first solution may not be the final solution and iteration of the process is required to arrive at an ultimate solution. For automation, the iteration is halted when the improvement of the standard deviation is less than 2% or if the magnitude of the solved shift vector is less than 0.5 m (other values are possible, but might require more iterations). The final correction is applied to the corner coordinates of the un-registered DEM by solving the x- and y-components of the shift vector from the magnitude ( $a$ ) and direction ( $b$ ). The mean bias determined by inverting Eq. (5.4) is added to the DEM using an estimate of the mean slope of the terrain ( $\alpha$ ) used to solve Eq. (5.3):

$$\begin{aligned}x_{\text{adjustment}} &= a \cdot \sin(b) \\y_{\text{adjustment}} &= a \cdot \cos(b) \\z_{\text{adjustment}} &= c \cdot \tan(\bar{\alpha})\end{aligned}\tag{5.5}$$

The co-registration procedure outlined here is not restricted to DEMs, but to datasets that contain a sufficient amount of stable non-glacier terrain to solve with Eq. (5.3). In particular, ICESat can be used for this despite the smaller amount of points available (Nuth and Kääb, 2011). This provides a framework for global co-registration using ICESat as a reference. Last, alternate methods for co-registration involve the basic principles in image matching techniques, but use entire DEMs rather than sub-image search windows (e.g. Berthier et al., 2007). The algorithm may be useful in situations where the terrain slope is low over the entire scene (i.e. < 5 degrees) and the aspect distribution is not close to uniform rendering the analytical solution (equation 5.3) un-solvable.

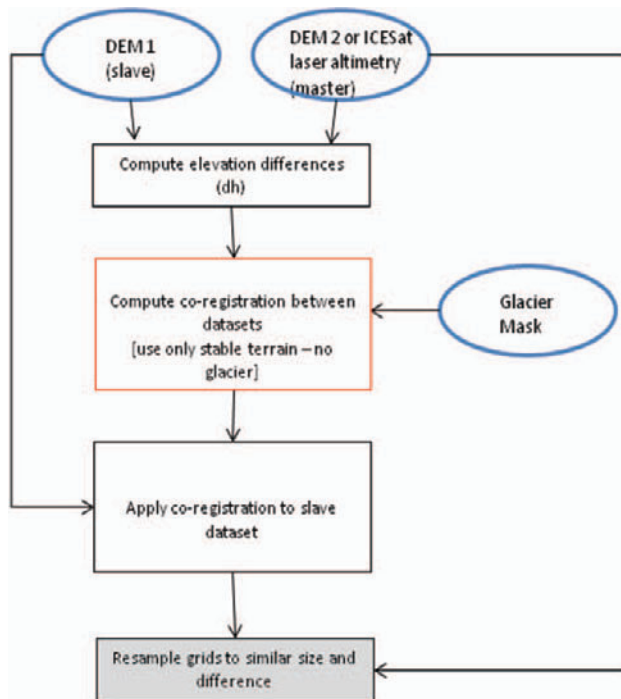
#### 5.4.4 Description of the processing line

Figure 5.2 outlines the processing scheme for DEM co-registration. The general procedures for DEM co-registration are:

- *Pre-Processing*: Selection of suitable terrain for input into the DEM co-registration routine. Suitable terrain is defined as stable and unchanging, i.e. outside glaciers, no water bodies, no clouds or data voids and assuming limited vegetation effects. This terrain is further used for both determining the co-registration parameters and later for validation of products and accuracy quantification. This choice of stable terrain is an implementation procedure that leads to variations in the accuracy.
- *Co-Registration*: DEM co-registration with the algorithms described in section 5.5. Adjustment of the slave DEM to the master DEM using the co-registration parameters.
- *Resampling*: Resample one DEM to another, and matrix difference the two aligned DEMs. Use the selected stable terrain for product validation and accuracy assessment. Estimation of random and systematic uncertainties in the final DEM difference grids.

### 5.5. Input data and algorithm output

The input data required for DEM co-registration is a slave DEM (to be co-registered) and a master DEM or laser altimetry (i.e. ICESat) I UTM projection. Auxiliary input data required is a glacier mask to separate stable terrain pixels from un-stable terrain (i.e. glacier) pixels. The geolocation accuracy of this dataset is uncritical, as outlines are buffered to be on the safe side. Once separated, the co-registration algorithm is then operated on the appropriate (non-glacier stable terrain) pixels. The output to the DEM co-registration tool are the co-registration parameters in the x, y, and z directions in metres, that can be applied by the user directly. Alternatively, a DEM co-registration tool may also be able to apply the co-registration and export a new DEM, directly. Outputs may also include an additional processing step to resample the DEMs to co-incident grids (requires interpolation) and further export an elevation difference grid (including glaciers and stable terrain) from which the user can assess glacier specific changes. We note that elevation difference grids of the glaciers alone (without the surrounding stable terrain) will not allow for error analysis by the users.



*Fig. 5.2: Flow chart for the elevation change – DEM differencing algorithm to be used. Input data is denoted by blue circles and may either be DEMs or ICESat laser altimetry. Also required is a glacier mask to determine stable terrain from which to apply the DEM co-registration algorithm. The output denoted as a grey shaded box may either be the raw co-registration parameters, the co-registered slave DEM, or a resampled difference DEM.*

Within Glaciers\_cci, we focus on product generation in selected key regions to obtain spatially common datasets. Whereas DEMs are available or can be created in most of the selected regions, a common period is more difficult to achieve. Here we have to use what is available in the respective region or can be produced from other datasets (e.g. from ASTER). Common periods P1-P4 of data availability are: P1: 1960-1990s (national DEMs, Corona/Hexagon), P2: 2000 (SRTM), P3: 2007-2012 (SPOT SPIRIT, ASTER), P4: 2012-2015 (ASTER, TS-X/TD- X, WorldDEM), respectively. Further details about time periods are given in Tables 2.1, 3.1, 4.1, and 5.1 of the DARD (Glaciers\_cci, 2014b). For spatial consistency, all results are provided in a metric UTM projection. At best, glacier outlines are available for the time of DEM acquisition or they do at least match the extent of the glaciers in the DEM. This is in particular critical for calculation of volume changes when glaciers are smaller than in the DEM for the older point in time ( $t_1$ ), as former volume loss will get cut-off and overall loss is underestimated. In this case we recommend determining the effect of the temporal inconsistency by manually digitizing extents fitting to the DEM for a couple of glaciers and subsequent determination of the difference (Le Bris and Paul, 2015).

## 5.6 Error budget estimates

The error budget of glacier elevation changes is in practice defined by the combination of the individual accuracies of the DEMs and may be estimated through either physical or statistical error modelling. Statistical error modelling is more robust, complete, and easier to implement. This error budget typically is composed of random errors estimated by the standard error of

the non-glacier terrain elevation differences after accounting for the degree of spatial autocorrelation. On top of this, the unknown systematic errors must be added. Parts of this uncertainty can be extracted through the co-registration of 3 or more DEMs, and subsequent sum of co-registration vectors (details in the PVASR Glaciers\_cci, 2012b). Ultimately, internal DEM bias may significantly affect the error of glacier elevation changes, but is difficult to detect and quantify, as there is negligible effect on measures of precision (random errors). A prime example is that of satellite jitter in, for example, ASTER DEMs. For cases where this is known to occur, the accuracy provided with products produced from these DEMs is set to the maximum bias that results from this effect, e.g. 10 m. For other products that do not seem to have these internal biases, the accuracy provided will be lower.

## 5.7 Expected accuracy

We estimate the reliability of the co-registration algorithm to return parameters as accurate as 1/10th a DEM pixel but certainly not worse than 1/3rd a pixel. Further investigation is required into the choice of stable terrain implemented and used for DEM co-registration as this affects the individual accuracies of the co-registration, the estimated errors for elevation difference grid products and the mean elevation changes that may be derived from them. It is highly important that the entire processing chain remain within one software. Within the round robin experiments, some contributions provided very accurate co-registrations, though the triangulation of co-registration vectors between 3 datasets revealed problems with the internal pixel definition (pixel centre vs. pixel corner) within the contributors processing chains as documented in the PVASR (Glaciers\_cci, 2012b). This failure to maintain proper pixel definition counter-acts the accuracy of the co-registration correction and the bias remains within glacier elevation changes even if considered removed. In addition, the choice of resampling is highly important, and should always be more sophisticated than nearest neighbour as this will also re-induce mis-alignments in the DEMs, and thus bias. In Glaciers\_CCI, we use bilinear interpolation as the standard. The resampling procedures used for glacier elevation change products from DEMs of varying resolutions requires first resampling of the finest resolution DEM up to the coarsest resolution DEM to reduce artefacts related to terrain curvature. This latter resampling uses a block averaging procedure with the block window size related to the resolution of the coarsest DEM.

## 5.8 Practical considerations for implementation

The co-registration algorithm presented here is the analytical solution to correct for a linear mis-registration between two DEMs, or elevation data sources. It is operational on continuous DEM products and also in combination with sparse laser altimetry (e.g. ICESat). The algorithm fails on low sloping surfaces (e.g. less than 3-5 degrees) and in situations where the aspect distribution is not uniform over at least 180 degrees of aspects. In these situations, some previous image matching based co-registration algorithms may be used (Berthier et. al. 2007). The number of iterations required to find a global minimum solution is on average between one and four. Computational effort will increase exponentially with the size of the DEM, so a subset might be selected to find the co-registration parameters.

## 6. Glacier Velocity

### 6.1 Introduction

A large number of archived and upcoming optical and SAR satellite missions make it now possible to operationally map and monitor glacier flow on a nearly global scale. Deriving glacier displacements globally provides unique glaciological information (Heid and Kääb, 2012a and b). It makes it possible to compare spatio-temporal variations of glacier velocities both within regions (e.g. Fig. 6.1) and between regions. Such knowledge enables better understanding of a wide range of processes related to glacier mass fluxes, such as glacier response to climate and climatic changes, glacier physics and flow modes, glacier flow instabilities (e.g. surges), subglacial processes (e.g. erosion), supra- and intra-glacial mass transport, etc. Knowledge about glacier ice supply helps to understand the development of glacier lakes and associated hazards (Kääb et al., 2005). Mapping and monitoring glacier flow globally perfectly complements current attempts for mapping and monitoring glacier areas and glacier volume changes on a global scale within Glaciers\_cci and other projects (GLIMS, GlobGlacier).

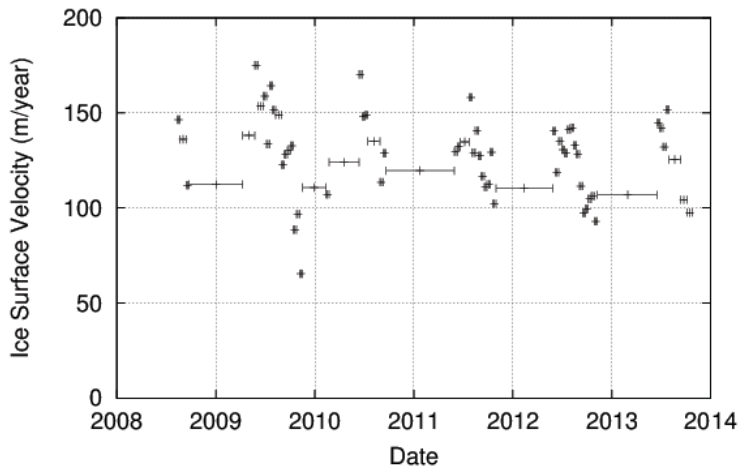


*Fig. 6.1: Variations of surface speeds from repeat TerraSAR-X data over Aletschglacier, Swiss Alps.*

Within the Glaciers\_cci project, the generation of ice motion fields of glaciers is performed using high and very-high resolution repeat-pass SAR images and medium to high-resolution optical satellite data. In the case of images from a single look direction none of these data, independent of the algorithm, is capable of providing 3-D ice surface velocity vectors, which is of interest for ice dynamic studies. Additional assumptions on the ice flow are introduced to provide ice velocity information for glaciological tasks; e.g. a surface-parallel ice flow assumption where the slope is derived from a low-pass filtered DEM. Another assumption assumes a static surface topography and provides the horizontal velocity components and the vertical surface elevation change, which is derived from the DEM and the horizontal displacement. This step involves assumptions and auxiliary data (in particular DEMs).

The suitable temporal baselines of the repeat data are defined by two fundamental constraints:

- The displacements have to exceed the accuracy of the method, i.e. have to be statistically significant;
- The surface changes such as melt, deformation, phase coherence loss, etc. over the measurement period have to be small enough so that the corresponding signal (intensity or phase) is preserved.

Typical temporal baselines suitable for optical data are up to 1-2 years for slow moving glaciers, for SAR offset-tracking up to a few weeks (depending on magnitude of ice flow and stability of available features), for SAR interferometry a few days (Glaciers\_cci, 2011b). In the optical domain, tracking methods are usually called ‘image matching’, in the microwave domain ‘offset tracking’. Here we use the term **offset-tracking** for both optical or SAR data.

This chapter provides an overview on the methods for retrieving ice motion fields from SAR and optical satellite data considering the results of the round robin and including the boundary conditions applied to transform satellite-derived displacement to ice surface velocity products. In response to the User Requirement Document (URD, Glaciers\_cci, 2014) and the surveys conducted in the requirement definition process, the main focus is on raw displacements derived from multi-temporal image pairs in UTM or geographic projection, i.e. without projection to a certain flow direction.

### 6.1.1 Ice Surface Velocity from SAR data

The generation of ice motion fields of glaciers requires repeat-pass images from high resolution SAR satellite data. As an active sensor, SAR data are independent of solar illumination (day/night) or cloud coverage. Moreover, accurate knowledge of the image acquisition geometry, the satellite orbit and the technical sensor properties enable precise retrieval of glacier motion from repeat-pass images. The penetration depth of microwaves in dry snow and ice is about a few metres to more than 100 m, depending on the RADAR frequency and snow and ice purity and structure (Ulaby et al., 1982; Mätzler, 1996; Rignot et al., 2001). For melting surfaces, as is the case for many temperate glaciers during summer, the penetration depth is highly reduced and backscattering occurs from the surface (top centimetres). While RADAR methods detect a mixture of surface and sub-surface features, they are generally referred to as a measurement of surface ice velocity as velocity at the maximum depth of penetration is about the same as at the surface (velocity reduction due to friction only started to play a role near the glacier bed).

Depending on the available SAR data in terms of spatial resolution and temporal sequence of repeat passes, three primary methods evolved during recent years to retrieve the ice surface motion fields:

- 1) Across-track repeat-pass SAR Interferometric (InSAR) analysis: delivers the velocity component in RADAR line-of sight (LOS) direction only (details are documented in the ATBDv0, Glaciers\_cci 2012a);
- 2) Multiple-Aperture Interferometry: provides an estimate of along-track velocity components applying split beam InSAR processing (details are documented in the AT-BDv0, Glaciers\_cci 2012a);
- 3) SAR offset tracking: provides two independent measures of the velocity, in LOS and in along-track (azimuth) direction.

All methods are performed in SAR slant range / azimuth geometry and require a proper transformation into map coordinates. Methods 1) and 2) are not followed in Glaciers\_cci.

### 6.1.2 Ice Surface Velocity from Optical data

Surface displacements from repeat optical data are usually performed on orthorectified and projected images so that the displacements are directly in the coordinate system aimed at. The method applied in most cases is block-matching (in contrast to feature-based matching) where a maximum similarity of an image template is searched for in the second image using image chips (also called templates). The mathematical algorithm is identical, or at least very similar, to the amplitude offset tracking of SAR images. Some differences in the performance of this technique applied to optical and SAR matching algorithms lies in their ability to cope with the speckle in SAR images (Debella-Gilo and Kääb, 2012).

Another difference relevant for offset tracking is the different image geometry of SAR and optical data. Most optical data used for this purpose are nadir looking, with, for instance, similar pixel resolutions over the image and little effect of topography and orthorectification errors from DEM errors, whereas both effects play a significant role in the side-looking geometry of SAR data. In their raw form, optical orthoimages provide the 2-dimensional horizontal displacement component in a given map coordinate system. They are sensitive to surface features only. To allow a comparison and potential merging with optical data, results from microwave sensors are converted to horizontal displacements (azimuth and magnitude).

## 6.2 Scientific background

### 6.2.1 Selection of the algorithm for ice motion fields from SAR data

The general steps of a processing line for ice motion retrieval from repeat-pass SAR data, including InSAR and offset tracking, are outlined in Fig. 6.2. As input a data stack of multi-temporal repeat pass SAR images and a DEM is needed. Accurate co-registration of the repeat pass SAR images is an important step for further analysis and has to be performed with high accuracy. Depending on the software implementation of the co-registration module different steps are applied including geometrical co-registration based on orbit and imaging parameters only, coarse-co-registration with pixel-accuracy using a DEM or not, and sub-pixel co-registration using stationary regions or points available in both images. In the latter methods it is important to mask out potentially non-stationary areas like glaciers or water surfaces in the co-registration process. The precisely co-registered SAR image stacks are fed into the offset-tracking modules for retrieving ice displacements. After performing offset-tracking the derived displacement component in RADAR geometry has to be resampled to the preferred map projection and can be converted to ice velocity maps.

The criteria used for algorithm selection within the Glaciers\_cci project were robustness, reliability and accuracy. This led to the selection of the intensity-cross correlation algorithm. The phase-based SAR methods (fringe-visibility, InSAR and MAI) show some inherent drawbacks which lead to a rejection of these algorithms for ECV production:

**Coherence:** The availability of coherent SAR data represents the main limitation. Glacier surface processes like summer melt cause total decorrelation between consecutive images. Further, short satellite repeat-cycles are a prerequisite for coherent images even in winter, and the current satellite missions do not fulfil this criterion.

**Phase unwrapping:** The process of phase unwrapping, translating phase shifts into actual motion values, is very costly and prone to errors. For example, it requires intensive interaction of a skilled operator, and fails with strong velocity gradients.

Therefore, offset tracking was selected as the main method for the production of ice velocity fields in phase 2 of the Glaciers\_cci project.

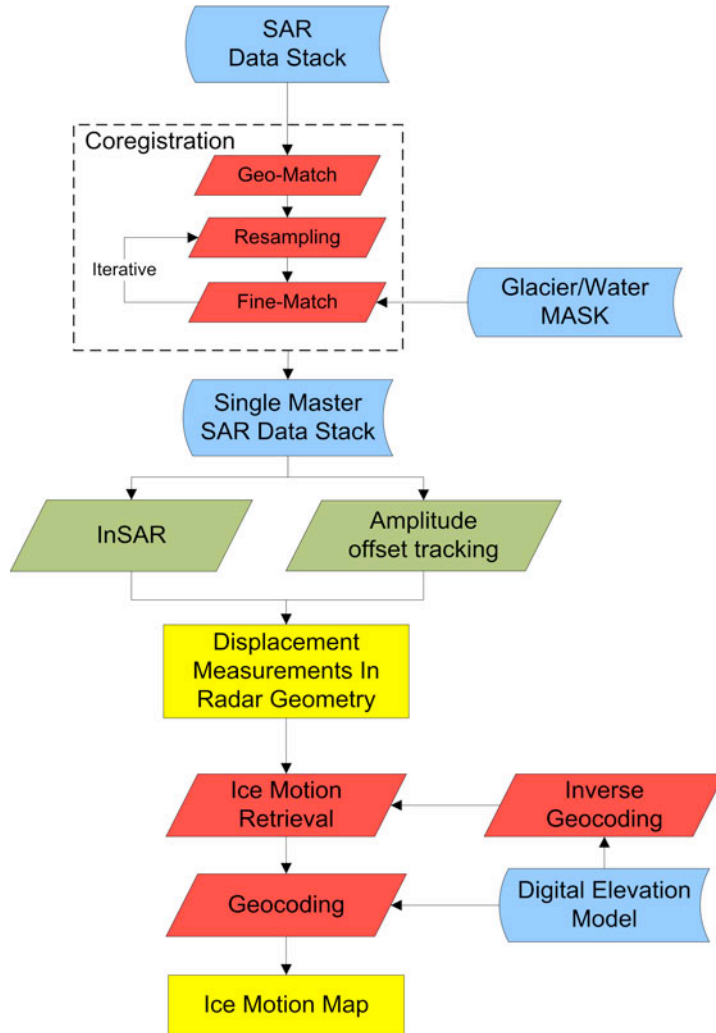


Fig. 6.2: Overview of general steps for ice motion retrieval from SAR data.

### 6.2.1.1 Ice motion fields from offset-tracking

Offset-tracking is employed in order to provide ice surface motion when the signal in the repeat-pass SAR image pair is not coherent. After the common co-registration, outlined in Fig. 6.2, the displacement is measured by applying various algorithms. One of the most commonly used is the normalized cross-correlation coefficient (NCC) of amplitude image chips according. Depending on the implementation there might be some overlap between the search and reference windows implicitly resulting in some low-pass filtering as the image windows are not completely independent. The NCC kernel provides image offsets in slant-range (LOS) and azimuth (along-track) direction. Optionally the Correlation Relaxation Labelling (CRL) tech-

nique can be applied to check for outliers in the displacement field. CRL provides the opportunity to check the consistency of a NCC image offset retrieval by comparing the results to neighbouring NCC results (Wu, 1995). If the result is not consistent with the neighbourhood it will be rejected. In general, the best performance of the NCC kernel can be expected in regions with pronounced surface features such as crevasses, drainage channels and surface moraines, but it also works where speckle (and thus coherence) is retained.

Offset tracking requires image patches of 64 x 64 pixels (this is a typically used value, though other values can be used depending on glacier flow velocity) to retrieve a single motion vector, which requires high-resolution SAR images like TerraSAR-X and CosmoSkymed for small alpine type glaciers. SAR Sensors with lower spatial resolution, like ERS SAR, ENVISAT ASAR or Sentinel-1 IWS, are suitable for large glaciers only. Distinct features (including speckle) need to be present on the glacier surface that move with the glacier and are preserved over months or years and in accumulation areas such features are usually missing. SAR offset tracking does also provide some information in (optically) low contrast accumulation regions (see Fig. 6.8). The limiting factor for SAR is steep terrain creating radar shadow) rather than contrast.

Complex-correlation of SAR images and coherence optimization are slight modifications of the incoherent offset tracking described above. These methods use complex SAR data as input to calculate the displacement and require some preservation of the RADAR signal between the two acquisitions. The advantage is that they are able to provide velocity measures in dry snow regions where no distinct features (crevasses) are present.

### 6.2.1.2 Retrieval of glacier surface velocity by SAR

The displacement of a particle on the glacier surface during a time interval, T, is described by the three-dimensional displacement vector  $\mathbf{d}$ :

$$\mathbf{d} = d_x \hat{\mathbf{x}} + d_y \hat{\mathbf{y}} + d_z \hat{\mathbf{z}} = \mathbf{d}_h + d_z \quad (6.1)$$

Normalizing the displacement by the time interval, T, between the two image acquisitions the velocity vector  $\mathbf{v}$ , is given by:

$$\mathbf{v} = v_x \hat{\mathbf{x}} + v_y \hat{\mathbf{y}} + v_z \hat{\mathbf{z}} = \mathbf{v}_h + v_z \quad (6.2)$$

$\hat{\mathbf{x}}$ ,  $\hat{\mathbf{y}}$ , and  $\hat{\mathbf{z}}$  are the unit vectors in the Cartesian coordinate system. The orientation of the coordinate system can, for example, be selected according to a specified map projection. In the following the x-coordinate is assumed to correspond to easting (E), the y-coordinate to northing (N), and the z-coordinate upward perpendicular to the local geoid surface. The three components of the vector can be re-arranged to separate the vertical displacement component  $d_z$  and the horizontal displacement vector  $\mathbf{d}_h$ . The vertical displacement (elevation change) at the glacier surface represents the net effect between the ablation/accumulation and emergence/submergence velocity of the ice at a given location. On land terminating glaciers in retreat, the emergence velocity in the ablation area is usually rather small. During summer the ablation dominates over emergence as well as on glaciers that are in balance over the year, causing the surface to subside.

Fig. 6.3 shows the imaging geometry of SAR and the velocity / displacement components.

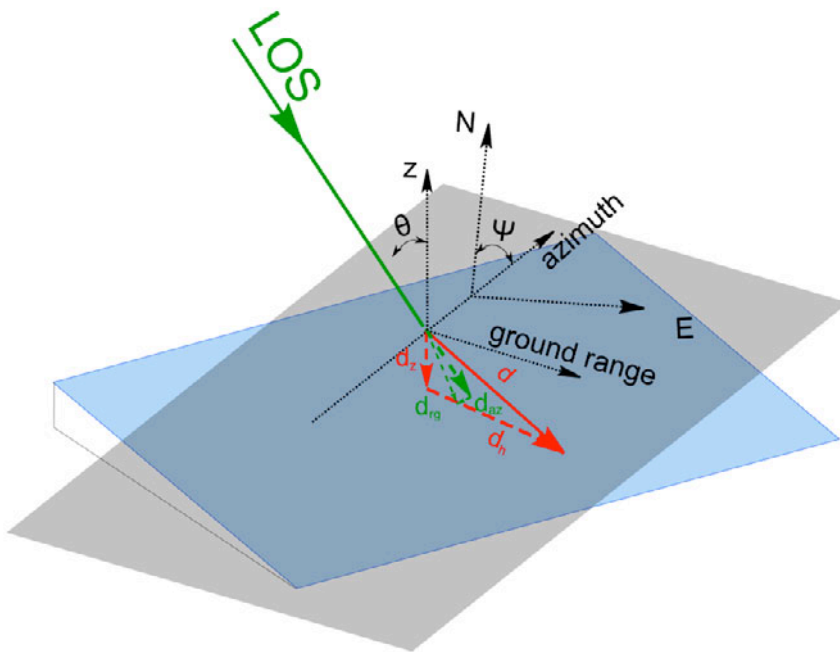


*Fig. 6.3: Sketch of the geometry of spaceborne SAR observations with 3D displacement vector ( $d$ ). With  $d_h$ : the horizontal displacement component,  $d_z$ : the vertical displacement (elevation change),  $d_{az}$  and  $d_{rg}$ : are the displacement components in azimuth and range direction in SAR slant range coordinates, respectively,  $\theta$ : the off-nadir angle, and  $\psi$  the azimuth angle (defined as the angle between North and along-track direction).*

SAR offset-tracking provides the shift of features in slant range and azimuth (across track) direction. Thus, an additional restriction about the deformation geometry is required in order to retrieve the 3D displacement. The displacement vector in slant range,  $r_g$ , and azimuth direction,  $d_{az}$ , observed at a pixel is related to the 3D displacement on the Earth surface according to

$$\begin{aligned} v_x &= |\mathbf{r}_{\text{LOS}}| \sin \nu \cos \varphi + |\mathbf{r}_{\text{az}}| \sin \varphi \\ v_y &= |\mathbf{r}_{\text{LOS}}| \sin \nu \sin \varphi + |\mathbf{r}_{\text{az}}| \cos \varphi \\ v_z &= |\mathbf{r}_{\text{LOS}}| \cos \nu \end{aligned} \quad (6.16)$$

The azimuth shift observed by offset-tracking is not sensitive to the vertical component of the displacement that is observed in the ablation zone of glaciers with significant ice melt (causing a net-decrease of surface elevation) and can thus be converted directly into horizontal motion. The slant range shift observed by offset-tracking includes both the horizontal and vertical motion, which cannot be resolved without additional information.

### 6.2.2 Selection of the algorithm for surface displacements from repeat optical data

Surface displacements from optical data are derived by finding similarities between two (or more) images. A general flow chart for the processing is shown in Fig. 6.4. Even if in some cases feature-based methods can provide good results, block-matching techniques are preferred due to the typical glacier surfaces that often lack distinct geometric features such as crevasses, but rather contain less sharp radiometric features, e.g. from dust or debris deposits.

The selected offset-tracking algorithms are listed in section 6.4. The main difference between the design of offset-tracking algorithms for SAR amplitude images and optical images are the higher robustness against RADAR speckle that SAR offset-tracking algorithms need to have. Thus, the same principles can be used for both types of images, but with different parameterisations (e.g. template size), and different evaluation criteria for their performance. Due to that, the different sensors used, the different pre-and post-processing procedures, and, importantly, the different imaging geometries and, thus, sensitivities to geometric errors, offset tracking based on optical and SAR data are treated in separate chapters. Nonetheless, the basic algorithm to derive displacements is the same for optical and radar, and, hence the resulting products are also geometrically comparable.

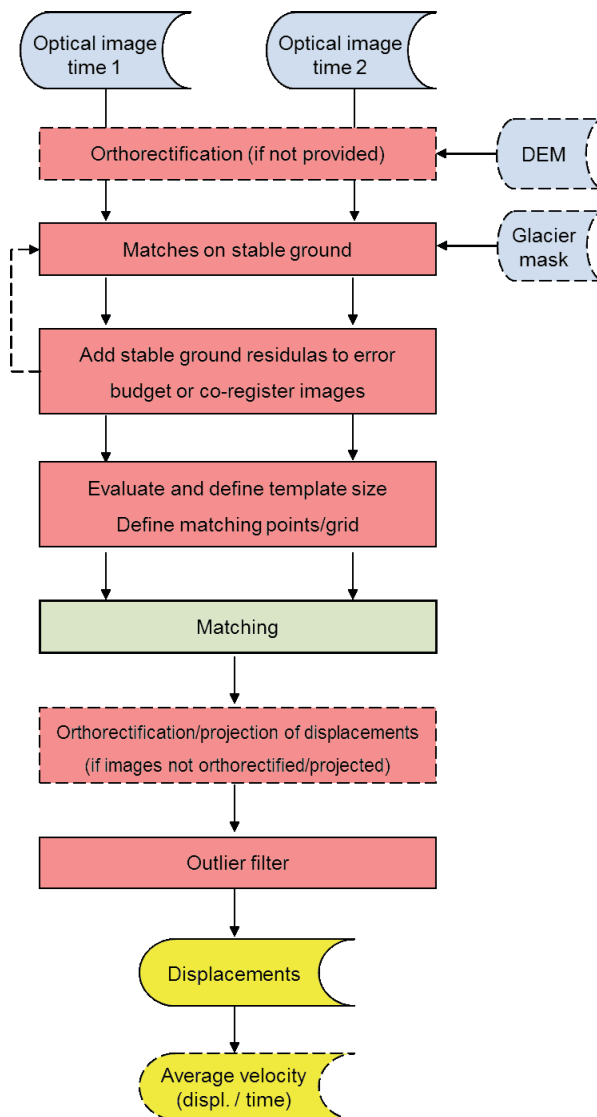


Fig. 6.4: Flow chart for glacier velocity from repeat optical images.

Usually, orthorectified optical data will be matched so that the raw displacements are already in the desired projection. A proper orthorectification is therefore crucial to the positional accuracy of the matches. The main error influences to orthoprojection are errors in the sensor position and attitude information (either in the auxiliary data or from orientation based on

ground control points) and propagated elevation errors from the DEM used for ortho-projection. Offsets on stable ground allow definition of the level of propagated DEM errors, and for evaluation and partial correction of orientation errors. Though, it is crucial to keep in mind that these errors, in particular the propagated DEM errors, cannot be simply corrected by coregistration because the mis-registrations are not linear (also not linear in the sense of a higher order polynomial). Rather, stable ground offsets give the background error to be expected from the matches on the moving glacier and to be added to the total error budget.

Since displacements are usually tracked from orthoprojected images, the tracked positions can be defined as a raster in e.g. UTM or geographic coordinates, or as points of special interest, for instance positions of ground measurements, such as GNSS, or fixed positions or flux gates for time series analysis. The matching template sizes can be chosen after iterative tests on the images, or from a list of typically optimal sizes for specific image types and resolutions. An automatic choice is in principle possible, but very time consuming and only particularly effective for high-resolution data, less for medium resolution such as Landsat (Debella-Gilo and Käab, 2012). The matching itself is to find in image of time 2 the most similar location to a template of image of time 1 (Fig. 6.5). The available algorithms differ among others in the similarity measure and the normalisation used.

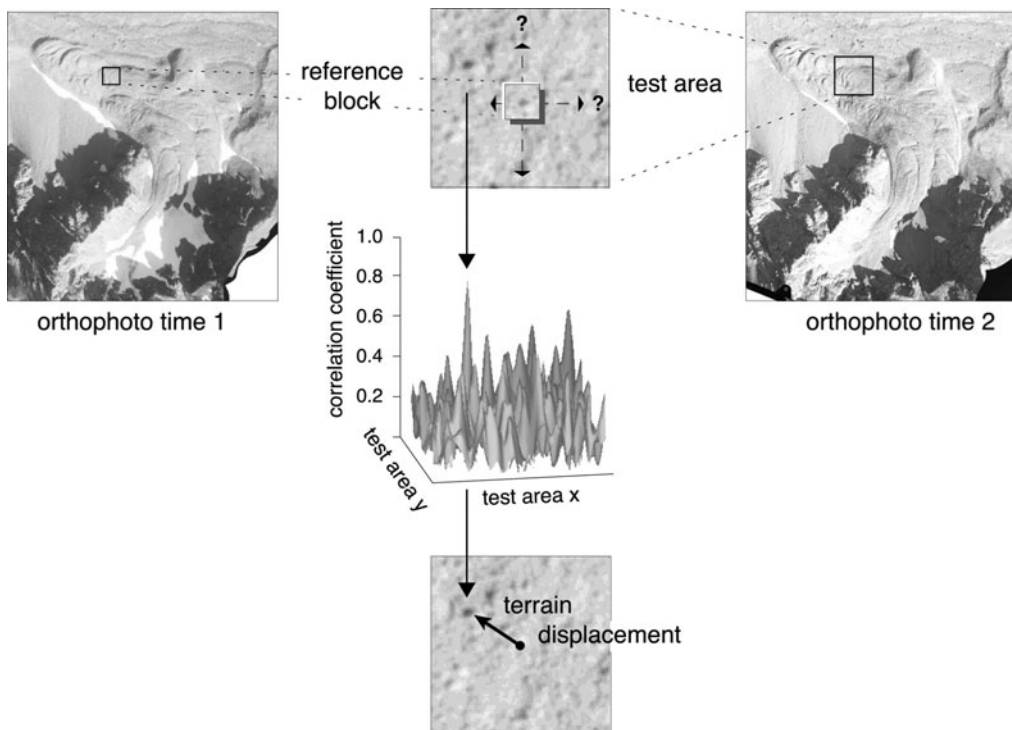


Fig. 6.5: Principle of matching between two repeat optical orthoimages within the offset-tracking process.

In the case the input images have not been orthorectified beforehand, the tracked displacements would have to be projected/orthorectified. This step requires reconstruction of the acquisition geometry and in most cases heavy operator interaction and specialized processing software. Glaciers\_cci does not therefore work with un-orthorectified optical images before the offset tracking process. The raw displacements can be filtered for outliers, and average

velocities be computed over the observation time period. The final displacements/velocities are horizontal movement components in the projection chosen for the orthoimages. This projection can be easily changed in standard software as the displacements are point information with attributes.

Since Glaciers\_cci phase 1 several new studies have appeared using offset tracking based on repeat optical data, but none of these have new or significantly modified algorithms. This confirms the algorithm choice made earlier for Glaciers\_cci.

### 6.3 Justification on the algorithm chosen

The purpose of the round robin was to compare algorithms and their potential embedding in a processing system with robust global-scale applications based on varying sensors in mind, rather than a review of the algorithms themselves on the strictly technical level (e.g. comparing advanced filtering methods for displacements). Moreover, projections to different three-dimensional movement components are not analysed, as the users prefer raw displacements in UTM or geographic projection. Hence, the main evaluation criteria for the assessment of glacier offset-tracking methods were:

- robustness of the method under different surface conditions;
- robustness of the method under different sensor resolutions (high & medium resolution);
- robustness of the method under different imaging frequencies (X-, C-, L-band);
- suitability of the method for a high degree of automation;
- accuracy requirements as outlined in the PSD (Glaciers\_cci, 2011b);
- user requirements as outlined in the URD (Glaciers\_cci, 2011a).

The round robin for the optical data suggest that no one matching method clearly outperforms all other methods investigated under all circumstances, but rather that a set of two methods should be combined depending on the image conditions and the glacier characteristics. Based on the evaluation criteria and algorithm comparisons the further steps (algorithm implementation, etc.) are based on NCC and CCF-O. The normalized cross-correlation in spatial domain (NCC) is a matching method that is often used when studying glacier velocities. This is much due to its simplicity and robustness. The first image is taken as the reference image and a template out of this image is searched for in the second image, or the search image. The peak of the cross-correlation surface indicates the displacement between the images. This cross-correlation is normalized.

The NCC algorithm is simple and robust and can be applied to both optical and SAR data. As a consequence of the normalization of images with different illumination conditions the correlation coefficient from different correlation attempts can be compared. The original precision of this algorithm is only on the pixel-level, but this can be improved by interpolation of the correlation peak or image template interpolation beforehand correlation. Because this method operates in the spatial domain (as a convolution operation), the computation is time-consuming compared to computations in the frequency domain. In addition, the NCC method is easily dominated by large differences in the image brightness, which is a major issue with optical images only where different snow, shadow or dark-rock conditions on glaciers during the acquisition of the two images might be present.

CCF-O computes cross-correlation in the frequency domain. One major advantage of CCF-O is that it is illumination invariant, i.e. the correlation is not affected by uniform areas. This is a desired property in glaciological research because uniform areas are common, not least due to snow cover. For the same reason the method is also capable to match striped Landsat images after the failure of the scan line corrector (SLC-off) which traditional image matching techniques (i.e. NCC) are not directly capable of. The main disadvantage of CCF-O is in regions of large velocity gradients (i.e. ice deformation) and especially narrow glacier tongues in which the algorithm may often match valley sides rather than the glacier or the method returns a mismatch (Heid and Kääb, 2012a).

Results from the round robin for SAR data demonstrated that the cross-correlation of chips in amplitude SAR images performs better compared to the other SAR methods (fringe-visibility, InSAR and Multiple Aperture InSAR), in particular regarding its wider application to different glaciers and SAR data. In terms of algorithm efficiency, pre- and post-processing are very efficient procedures with processing durations of a few minutes, but main processing might be quite computationally intense (e.g. between one hour to a few days for a whole SAR scene depending on window size, pixels spacing and oversampling factor).

## 6.4 Processing line for optical data

### 6.4.1. Pre-processing

#### 6.4.1.1 Geometric pre-processing

The most crucial pre-processing step before offset-tracking is the accurate co-registration of the data to be matched. Offsets over stable ground measured using the same algorithms as evaluated below (though often with different parameterizations) form the base of co-registration. The search (slave) image(s) can be either transformed to the geometry of the reference (master) image or (e.g. polynomial) transformation parameters can be computed and applied to the matching results without transforming the images. Co-registration transformation has the advantage to make offset-tracking and other usages of the images (e.g. time-series analysis) easier, but increases the computational time and storage and may introduce loss of information.

A polynomial transformation from a working image with coordinates (u,v) to the reference image (x,y) is given by:

$$\begin{aligned} u &= \sum_{l=0}^m \sum_{j=0}^i a_{lj} x^l y^{j-1} \\ v &= \sum_{l=0}^m \sum_{j=0}^i b_{lj} x^l y^{j-1} \end{aligned} \tag{6.17}$$

Where a and b are the polynomial parameters, and m and i the order of the polynomial used, in image registration typically up to 5th order. Note that (polynomial, and other) higher-order coregistration is not fully the appropriate model when tracking offsets in orthorectified images (see 6.2.2), but only when images in sensor geometry or in ellipsoid projected format are used. For orthoimages, a lower-order polynomial co-registration is used (lateral shift, rotation of significant), as orthoimages contain propagated DEM errors that vary locally and un-systematic.

#### 6.4.1.2 Radiometric pre-processing

A number of radiometric pre-processing steps in offset-tracking have been proposed such as:

- i. Normalizations of the images (Heid and Käab, 2012a);
- ii. Tracking based on derivatives of the image data rather than the raw data (e.g. filtered versions, gradient images) (Heid and Käab, 2012a);
- iii. Interest operators to select suitable tracking targets (Förstner, 2000; Debella-Gilo and Käab, 2012);
- iv. Selection of most suitable band, if available, or derivatives of multiple bands (e.g. principle components).

Some of these pre-processing possibilities can only be applied to very specific input data (iv) and do not meet the evaluation criteria described in section 6.3. Other potential pre-processing procedures (i, ii) are actually built-in in some tracking algorithms. Further procedures (ii, iii) depend much on the data resolution and noise level, and thus also do not meet the evaluation criteria. As a consequence only radiometric pre-processing procedures that are largely independent of input data are considered. Since their applicability depends much on the tracking algorithm, they are considered together with these algorithms in the next section.

#### 6.4.2 Selected algorithms for glacier velocity

The tables below summarize the main characteristics of the two selected algorithms NCC (Table 6.1) and CCF-O (Table 6.2).

---

<i>Abbreviation</i>	<b>NCC</b>
<i>Algorithm</i>	Normalized cross-correlation in spatial domain
	$CC(i, j) = \frac{\sum_{k,l} (s(i+k, j+l) - \mu_s)(r(k, l) - \mu_r)}{\sqrt{\sum_{k,l} (s(i+k, j+l) - \mu_s)^2 \sum_{k,l} (r(k, l) - \mu_r)^2}} \quad (6.18)$
<i>Reference Applications</i>	Käab and Vollmer (2000), Heid and Käab (2012a) Käab (2005)
<i>Description</i>	NCC is a matching method that is often used when studying glacier velocities. This is mostly due to its simplicity and robustness. The first image is taken as the reference image, and a template out of this image is searched for in the second image, or the search image. The peak of the cross-correlation surface indicates the displacement between the images. This cross-correlation is normalized.
<i>Advantages</i>	<ul style="list-style-type: none"> <li>- The algorithm is simple and robust.</li> <li>- The algorithm can be applied to optical and SAR data.</li> <li>- Effects of normalization: Firstly, images with different illumination conditions can be better compared, and secondly, the correlation coefficient from different correlation attempts can be compared.</li> </ul>
<i>Disadvantages</i>	- Original precision is only on the pixel-level.

- Because this method operates in the spatial domain (as a convolution operation), the computation is time-consuming compared to the frequency domain.

- The NCC method is easily dominated by large differences in the digital numbers. If large differences exist within the reference or the search template, large differences also have to exist in the opposite window (i.e. the search or the reference template, respectively). We hypothesize that this is a major drawback with this method for glacier applications using optical data. Glacier areas usually contain large differences in digital numbers, because white snow and black rocks etc. are present. This would not be a problem if these differences were present in both images and also represented the displacement. However, it is common that snow patches in one image disappears in the next image, or that rocks move independently of the glacier movement by rolling or sliding at the glacier surface. Situations where large intensity differences are not present in both images or where large intensity differences do not represent the displacement are hence hypothesized to create erroneous matches for the NCC method.

### *Improvements*

- The original pixel-level precision of NCC can be improved by interpolation of the correlation peak or image template interpolation beforehand correlation (Debella-Gilo and Kääb, 2012). In Glaciers\_cci, image intensity interpolation of the matching templates is used.
- Entire scenes or scene sections are matched, but a glacier mask is added as data layer indicating which matches are on a glacier or not, according to the glacier outlines available.
- The algorithm contains an image-pyramid of 2-3 levels in which a coarse (but potentially more robust) initial measurement is followed by one or two more precise local refinements.

Table 6.1: Summary of the NCC algorithm for the glacier velocity product.

<b>Abbreviation</b>	<b>CCF-O</b>
<b>Algorithm</b>	Cross-correlation on gradient images in frequency domain $f_o(x, y) = \text{sgn}\left(\frac{\partial f(x, y)}{\partial x} + i \frac{\partial f(x, y)}{\partial y}\right)$ $g_o(x, y) = \text{sgn}\left(\frac{\partial g(x, y)}{\partial x} + i \frac{\partial g(x, y)}{\partial y}\right)$ $\text{where } \text{sgn}(x) = \begin{cases} 0 & \text{if }  x  = 0 \\ \frac{x}{ x } & \text{otherwise} \end{cases} \quad (6.19)$
<b>Reference</b>	Fitch et al. (2002)
<b>Applications</b>	Heid and Kääb (2012b)
<b>Description</b>	CCF-O computes first image intensity gradients in both dimensions, x and y. The new gradient images, called orientation images, are complex and hence consist of one real and one imaginary part, where the intensity differences in the x-direction represent the real matrix and the intensity differences in the y-direction represent the imaginary matrix. These orientation images are matched using cross-correlation in the frequency domain.

where sgn is the signum function and i is the complex imaginary unit. The new images  $f_0$  and  $g_0$  are complex.

Fitch et al. (2002)

Heid and Kääb (2012b)

CCF-O computes first image intensity gradients in both dimensions, x and y. The new gradient images, called orientation images, are complex and hence consist of one real and one imaginary part, where the intensity differences in the x-direction represent the real matrix and the intensity differences in the y-direction represent the imaginary matrix. These orientation images are matched using cross-correlation in the frequency domain.

<i>Advantages</i>	- Orientation correlation is illumination invariant. Because the orientation vector (and hence both orientation images) has zero value in uniform areas and a length of one in non-uniform areas, the correlation is not affected by uniform areas. This is a desired property in glaciological research because uniform areas are common. We also hypothesize this to be important when it comes to matching striped Landsat images after the failure of the scan line corrector (SLC-off) because the stripes are ignored when using orientation correlation.
<i>Disadvantages</i>	Not known (besides general image matching problems).
<i>Improvements</i>	Not known.

*Table 6.2: Summary of the CCF-O algorithm for the glacier velocity product.*

#### 6.4.3 Post-processing

None of the algorithms above directly provides consistently accurate and reliable results. Errors and outliers cannot be avoided because of non-perfect image and ground conditions and have to be detected and filtered as much as possible ([Fig. 6.6](#)). Most of the above tracking algorithms provide, together with the offset with highest score, the correlation coefficient (CC) or signal-to-noise ratio (SNR) of the resulting offset. These measures can directly be used to estimate the potential quality of a match, and employ filters based on CC or SNR thresholds. Since CC and SNR, however, depend not only on the quality of a match but also on the image texture, such filters are not strictly conclusive and are used in combination with other post-processing measures. The Glaciers\_cci product on optical glacier velocity contains an attribute column of CC and/or SNR values that allows the user to set the according thresholds on the complete raw data.

The resulting displacement field is low-pass filtered (e.g. median) in order to filter out individual outliers. Similar to a resolution pyramid, the raw displacements will be compared to a low-pass filtered version of the field and measurements marked as outliers when the difference exceeds a given threshold on displacement magnitude and direction. This procedure is very successful over dense fields, but may fail where successful matches are only scattered, or where entire groups of displacements have a similar bias. The Glaciers\_cci product on optical glacier velocity will contain an attribute column of values that indicate the difference between the raw and low-pass filtered version, which allows the user to set the thresholds for measurement acceptance by themselves.

It should be noted that in our opinion glaciologically sound and useful glacier displacements can only be obtained when the automatic results undergo a final expert check and, potentially, editing (similar to the well acknowledged and good practice in multispectral glacier mapping). Thus, the aim of displacement filters is to support the analyst in removing the obvious errors as much as possible to focus on details that require glaciological expert judgment.

Displacements are provided using both NCC and CCF-O algorithms. The comparison between both gives another indication of reliability, but it is advised to not merge both results as both algorithms have their advantages and limitations that are specific to ground and image conditions. Rather, one of the two products should be chosen based on the better quality indicated by the above outlier detection and spatial coverage. In Glaciers\_cci we use the percent glacier coverage with valid measurements defined by a correlation threshold of 0.7 as a measure of product quality.

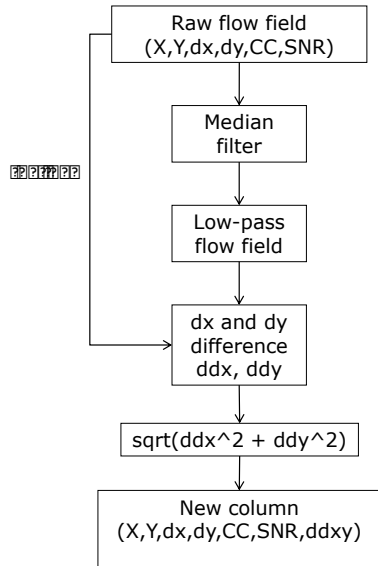


Fig. 6.6: Outlier filtering processing flow chart.

Filters on minimal/maximal speeds and vector directions can be very successful for individual glaciers that have specific maximum speeds and flow in a certain main direction, but are less useful for automated processing and groups of glaciers. Filtering the displacements based on the assumption that glaciers flow down-slope is considered to be impossible globally, because the required accurate elevation models are not available in all glacierized areas, and because of physical reasons where this assumption simply does not hold, such as in confluence areas or for supra-glacial ice topography. Some examples of the algorithm results and the filtering techniques discussed above are presented in Figs. 6.7 to 6.9 for a test site in Karakoram.

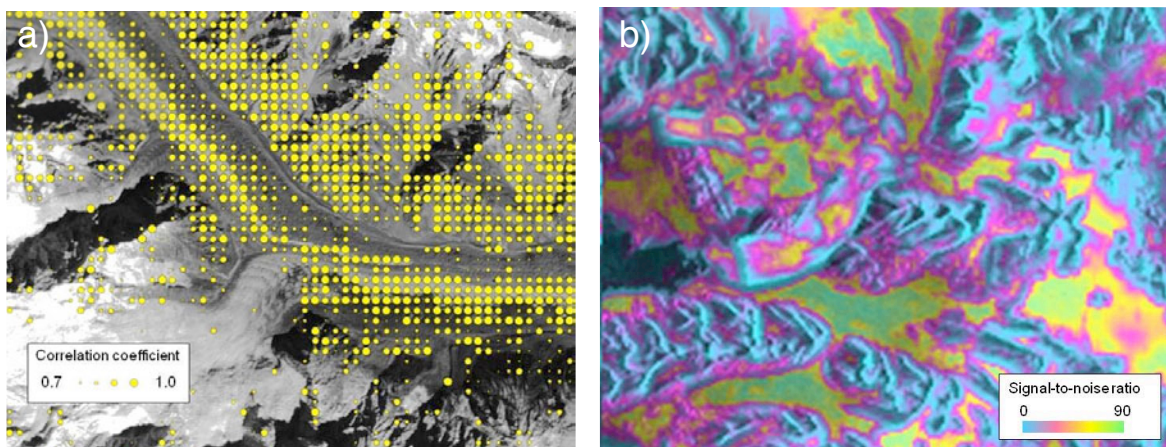
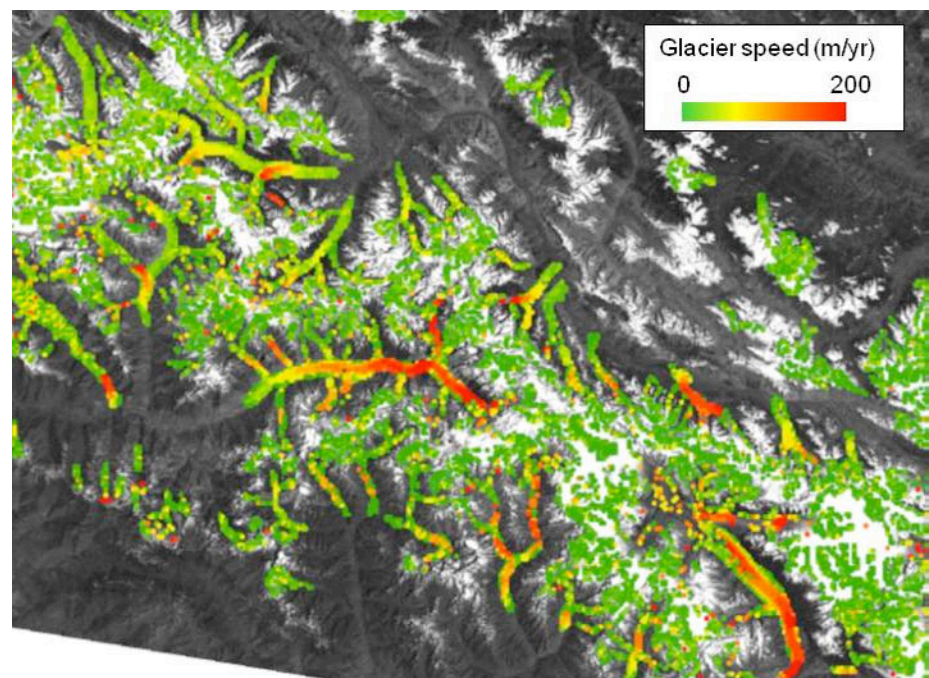
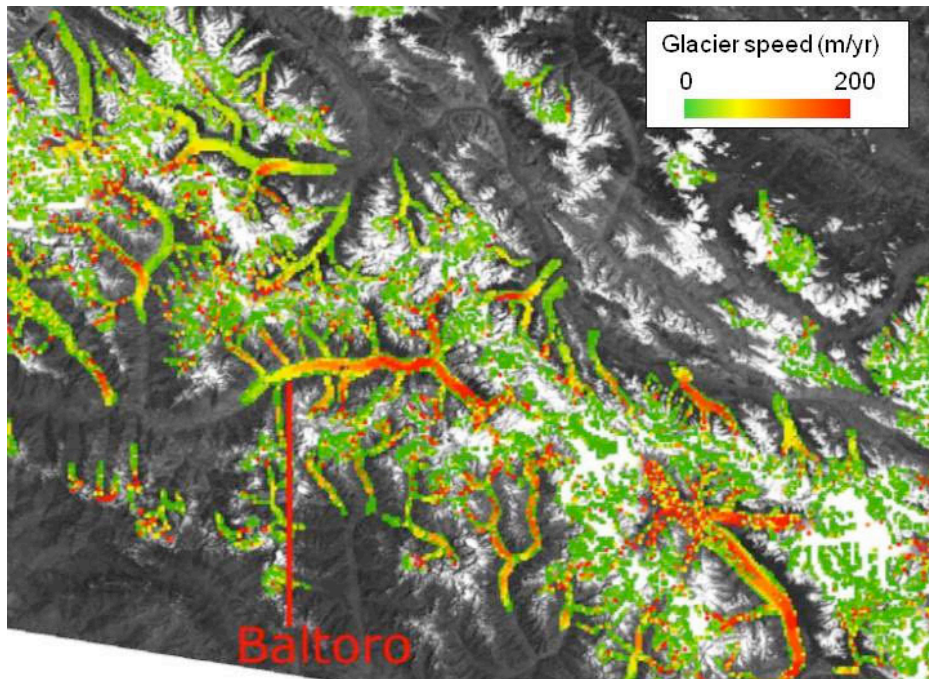
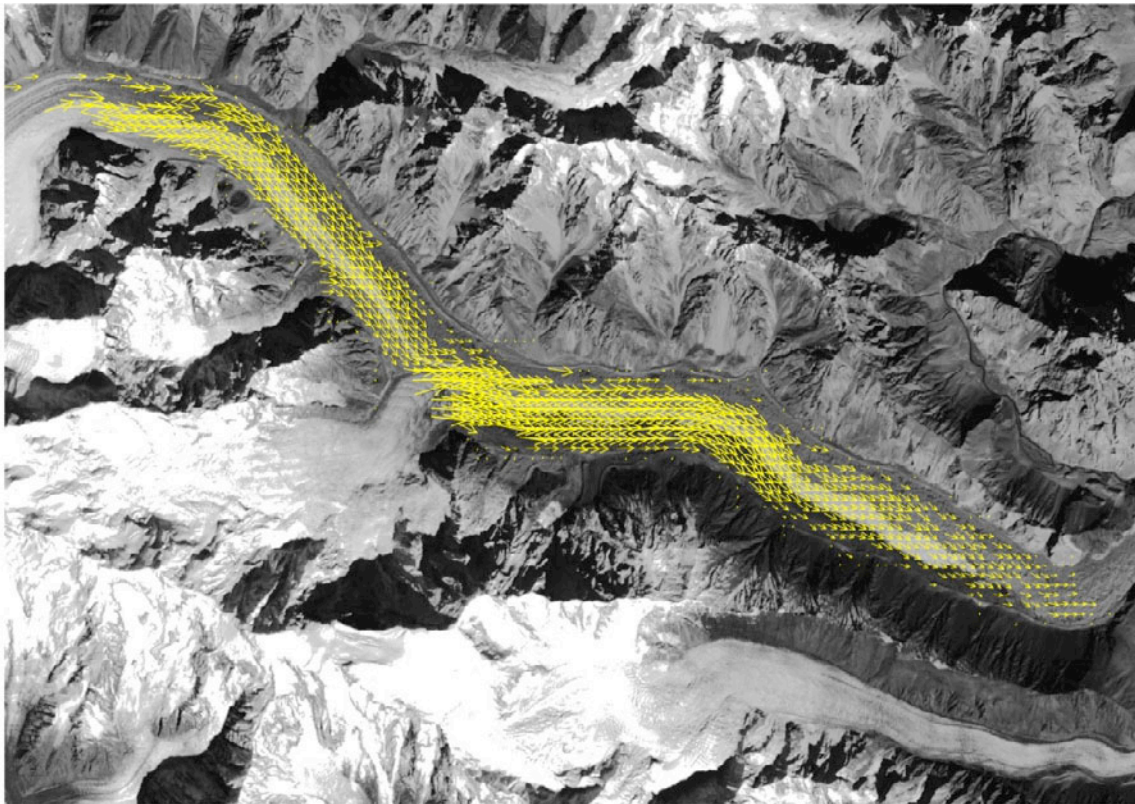


Fig 6.7: a) Cross-correlation coefficients for a 2000-2001 Landsat ETM+ image pair over Batura glacier, Karakorum. Small circles 0.7, maximum circles 1.0, correlation coefficients < 0.7 are removed (image width: 15 km). b) Signal-to-noise ratio (SNR) of offset-tracking between two ERS SAR images of 5 Apr and 10 May 1996 over Kronebreen, Svalbard. SNR values increase from blue over red to yellow and green (image width: 45 km). North is at top.



*Fig. 6.8: Upper panel: Raw glacier speeds 2000-2001 as derived from a Landsat ETM+ image pair using CCF-O. Lower panel: Glacier speeds from the upper panel automatically filtered using a threshold on differences between the raw measurements and a low-pass filtered version of them. Maximum speed (red) is up to 200 m / year. Image width: 170 km, North is at top.*



*Fig. 6.9: Typical output of optical image matching after outlier filtering, displayed as vectors of velocity magnitude and direction (Batura glacier, Karakorum). North to the top. Image width: 30 km. Maximum speeds up to 140 m/yr.*

## 6.5 Processing line for SAR

In addition to the core NCC algorithm as the main processing module (see description in 6.4.2), the flow diagram of SAR offset-tracking (Fig. 6.10) visualizes important pre- and post-processing issues for SAR data.

### 6.5.1 Pre-processing Module

In the pre-processing step data import and quality check (e.g. missing line detection) are first performed. The most crucial pre-processing step is then the accurate co-registration of the data to be matched. Offsets measured using the same NCC algorithms as the main processing (though often with different parametrizations, e.g. with much more limited number of sampling to reduce the computational borders) or using another algorithm (e.g. based on orbital data only or on fringe visibility) form the base of co-registration. A glacier outline mask can be optionally employed to limit the search over stable ground. A DEM can be optionally considered in the co-registration step in order to compensate for the stereo offsets relevant for the range offset field. The search (slave) image can be then either transformed to the geometry of the reference (master) image or (e.g. polynomial) transformation parameters can be computed and applied to the matching results without transforming the images. Co-registration transformation has the advantage to make offset-tracking and other usages of the images (e.g. time-series analysis of SAR data) easier, but increases the computational time.. A polynomial transformation from a working image with coordinates  $(u,v)$  to the reference image  $(x,y)$  is given by Equation (6.17).

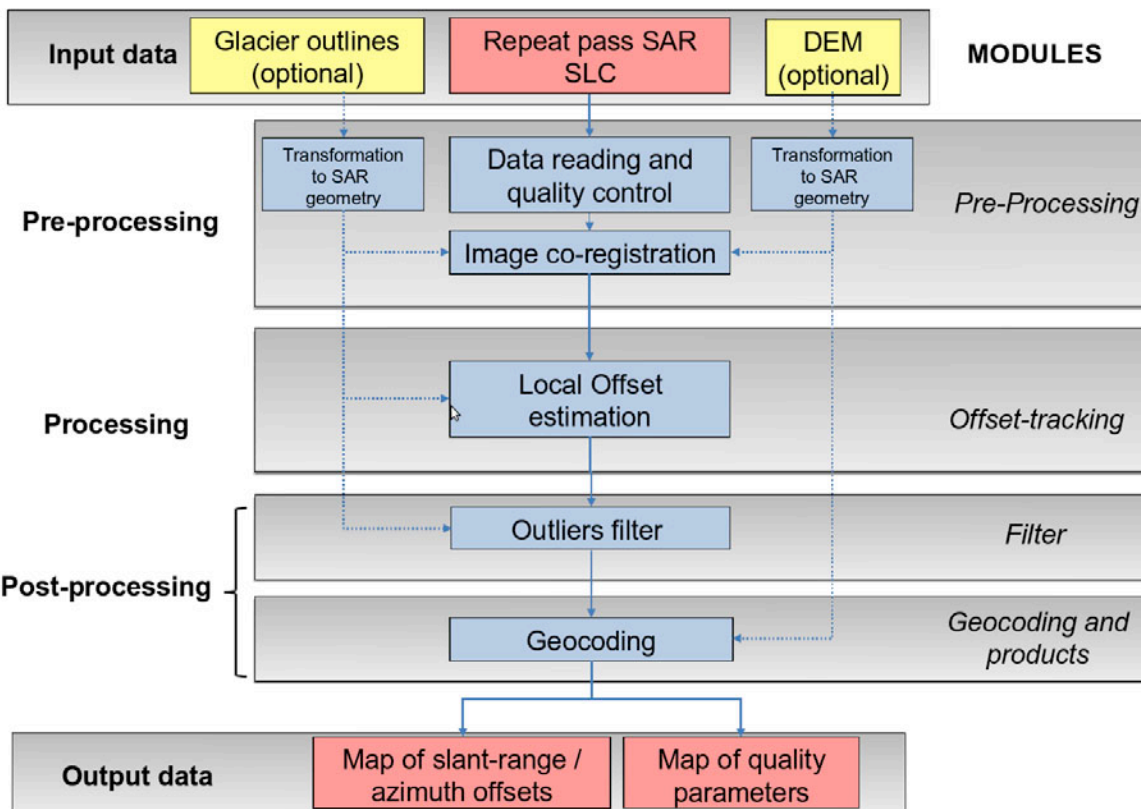


Fig. 6.10: Flow diagram outlining the principal processing steps of SAR offset tracking, including a first tentative indication of processing modules.

### 6.5.2 Offset-tracking Module

Once co-registered repeat-pass SAR images are available, NCC is employed to estimate offset-fields in slant-range and azimuth directions. In its mathematical framework the normalized cross-correlation in spatial domain is given in Equation (6.18). Offsets are measured using patches that are  $M_1 \times M_2$  (range x azimuth) pixels at a set of positions in the scene. The locations may be uniformly distributed over the image frame but for deformation mapping a specific region (i.e. glaciers) can be also selected for dense sampling. After global co-registration, the residual offsets should not be larger than a small fraction of the patch size that will be used for measuring the offset field. Typical values for  $M_1$  and  $M_2$  are in the range of 16 to 512 depending on the noise level, sensor resolution and specific application.

Data covering the patch is extracted from each SLC (single look complex) and the patch SLC data might be over-sampled by a factor of 2 or 4 using FFT interpolation to substantially improve the accuracy (Werner et al., 2005). The location of the maximum of the 2D correlation function yields the desired range and azimuth offsets. In order to obtain an accurate estimate of the correlation peak, the correlation function values over a  $(m_1 \times m_2)$  region can be fitted using a bi-quadratic polynomial surface. The SNR of the offset measurement is obtained by taking the ratio of the peak value divided by the average correlation level outside the  $(m_1 \times m_2)$  peak region. Typical values for  $m_1$  and  $m_2$  are in the order of 3.

### 6.5.3 Outlier Filtering Module

Similarly to working with optical images, also SAR offset-tracking does not directly provide accurate and reliable results. Errors and outliers have therefore to be detected and filtered (see example in Fig. 6.11). Post-processing steps of SAR offset-tracking is similar to that of optical images, which was described in Section 6.4.3 and is thus not repeated here.

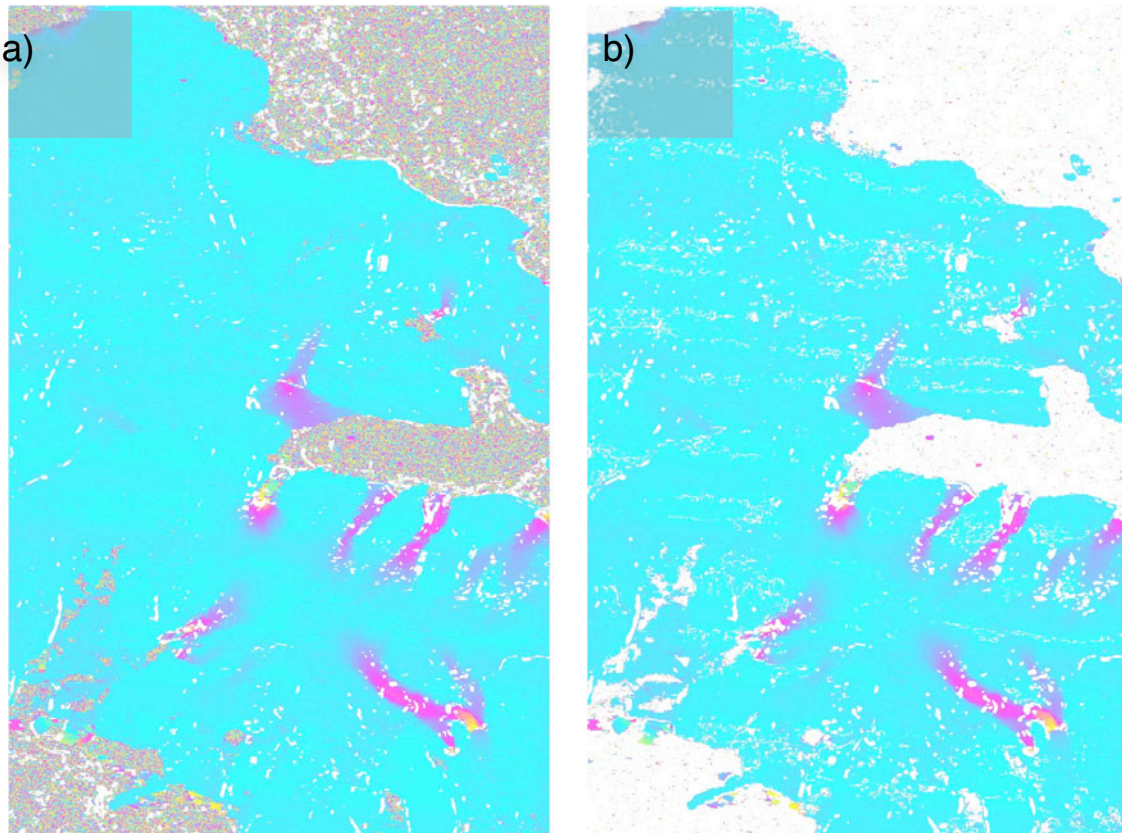


Fig. 6.11: Amplitude offset-tracking of an ALOS PALSAR pair from 1 February to 18 March 2008 over Vestfonna (Svalbard), (a) without outlier filtering and (b) with outlier filtering. Maximum speed (yellow/green) is up to 500 m/yr. The scene width is c. 70 km and the image is in the original RADAR geometry.

### 6.5.4 Geocoding Module

Prior to delivery, the displacement fields are geocoded. The geocoding of SAR images is acknowledged as an automatic procedure that requires special attention because of two typical characteristics of the SAR images: the range-Doppler image geometry and the speckle. Geocoding of SAR images can be performed in a three-step procedure (Werner et al., 2002).

- In a first step, a parametric description of the orbit, the SAR imaging geometry, the map projection, and the local terrain height (which requires a DEM in a strict procedure but that can be also accomplished on ellipsoidal height) are used to calculate an initial geocoding lookup table. The lookup table contains for each pixel of the map (i.e. the geocoded images in the desired map projection) the corresponding coordinate in the SAR range-Doppler geometry.

- Errors in the available orbit data, the SAR system parameters, and uncertainties in the map projection definition usually result in slight geocoding errors, which are corrected in a refinement step. As fine registration function a bi-linear function (range and azimuth offsets are linear functions of range and azimuth) is usually used.
- In the final step, the data files are resampled using the computed lookup table with advanced interpolation algorithms.

The refinement step is usually based on cross-correlation analysis between the SAR image to be geocoded and a SAR image simulated from a DEM. A SAR backscatter image is simulated from the local geometry and resampled into the SAR coordinates using inverse geocoding. Rather than having a small set of points, the simulated image can provide hundreds of features suitable for automated matching. The local offsets between the simulated and actual images are measured throughout the image. Then a least-square fit of the offsets is performed to obtain a polynomial transformation used to refine the lookup table. The values in the refined lookup table give the precise mapping between the SAR image and DEM. Modification of the lookup table values avoids having to resample the data a second time when generating a precise geocoded image. Considering that glaciers in high mountain regions are exposed to large topographic relief and sometimes fast elevation changes (e.g. from ice melt), the quality, resolution and release date of the DEM nominally affects the final accuracy of the geocoding.

## 6.6 Input data

The focus of the round robin was on the selection of algorithms for highly automated and robust global-scale applications based on various sensors. Hence, the datasets for product generation must be globally available, provide regular acquisitions, and have no or uncomplicated access restrictions. Consequently, all current and future planned satellite SAR data as well as data from several optical sensors can be considered for production of glacier displacements:

- ERS-1/2 SAR, Envisat ASAR, Radarsat-1/2, Sentinel-1 IWS at C-band;
- JERS-1 SAR, ALOS PALSAR and ALOS-2 PALSAR-2 at L-band;
- Landsat (15-30 m), ASTER (15 m), Sentinel-2 (10 m), Landsat 8 (15-30 m);

While Landsat data are already orthorectified (as L1T product), ASTER data can be ordered with and without orthorectification, the former is used in Glaciers\_cci. So far, we use the version that is orthorectified with a synchronous ASTER stereo DEM rather than the DEM as applied for orthorectification of Landsat scenes. The data have different co-registration accuracies on the subpixel level, i.e. pixel geolocation accuracies that can be estimated by stable ground matches, and have to be added to the error budget.

Data from the following sensors are considered for product and algorithm validation only, due to low spatial and temporal availability, limited coverage, usage restrictions, etc.:

- Optical:
  - ALOS AVNIR and PRISM (have to be orthorectified),
  - SPOT (orthorectified),
  - commercial very high-resolution sensors e.g. Ikonos, Quickbird, etc. (have to be orthorectified),
- Google Maps screenshots;

- SAR:
  - TerraSAR-X,
  - Radarsat high-resolution,
  - Cosmo-Skymed.
  - Sentinel-1 SM,

In the following sub-sections we describe upcoming and available new sensors and their impact on the processing line and products.

## 6.6.1 Landsat 8 Operational Land Imager (OLI)

The two most important characteristics of repeat optical data for offset tracking are:

- the detectability of corresponding features over the observation period, and
- the georeference accuracy of these features.

The first decides if and where displacements can be measured and with what reliability, and the second, how accurately the displacements and the location of displacements are determined for a given algorithm.

### 6.6.1.1 Georeference

As the USGS processing line for orientation and orthorectification of Landsat 8 data is equivalent to Landsat 7 and 5, we expect the largest changes to georeferencing to be caused by the transition from the scanner principle, used up to and including Landsat 7, to the pushbroom principle, used for Landsat 8. In particular, one could expect that the moving scanning mirror introduces geometric noise that should be reduced in Landsat 8 which lacks moving parts. This geometric noise is in (large) part responsible for the so-called coregistration accuracy, i.e. accuracy with which two images of the same scene can be coregistered to each other. For Landsat 7 an accuracy of around a third of a pixel is given (Lee et al., 2004). Fig. 6.12 shows the coregistrations of two sequential (16d) Landsat 7 and Landsat 8 scenes. The coregistration accuracy is much better for Landsat 8, a result which is confirmed by other similar tests (Kääb et al. 2016)/

### 6.6.1.2 Detectability of features

Landsat 8 offers 12 bit radiometric resolution versus 8 bit for earlier Landsat missions. This improved radiometric resolution enables, potentially, the detection of matching features that can not be detected in data from Landsat 7 or earlier. In addition the noise levels have been improved in Landsat 8, reducing the radiometric noise and thus enabling the use of smaller matching window sizes or, alternatively, allowing for better matching precision. Fig 6.13 shows a snow field in Landsat 7 and 8 data from roughly the same time, illustrating the improved radiometric fidelity of Landsat 8 OLI. Over the homogenous snow surface shown Landsat 7 data exhibit a standard deviation of about  $\pm 3$  digital numbers (DN), whereas Landsat 8 only  $\pm 0.3$  DN (when scaled to 8bit as Landsat 7).

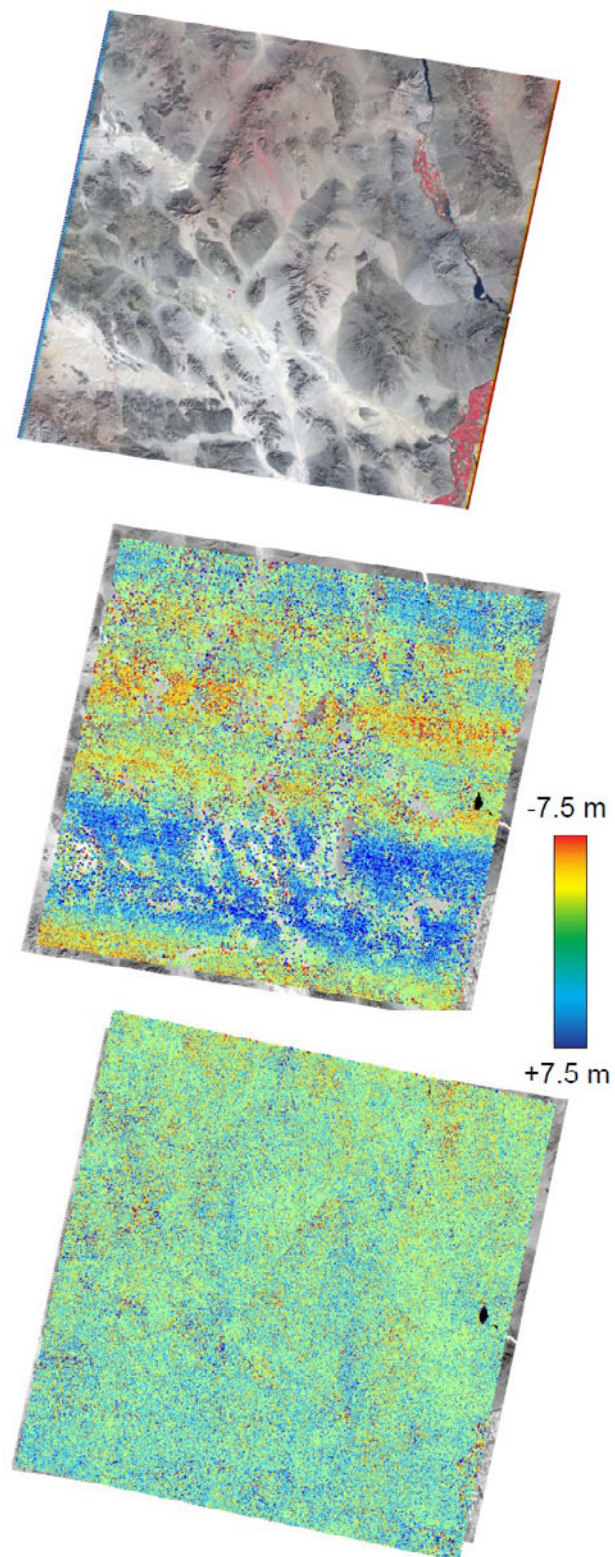


*Fig. 6.12: Upper panel: USGS test site Kelso/AZ (Landsat 7 scene), Middle panel: Cross-track component of coregistration between two repeat Landsat 7 scenes. Lower panel: Cross-track component of coregistration between two repeat Landsat 8 scenes.*

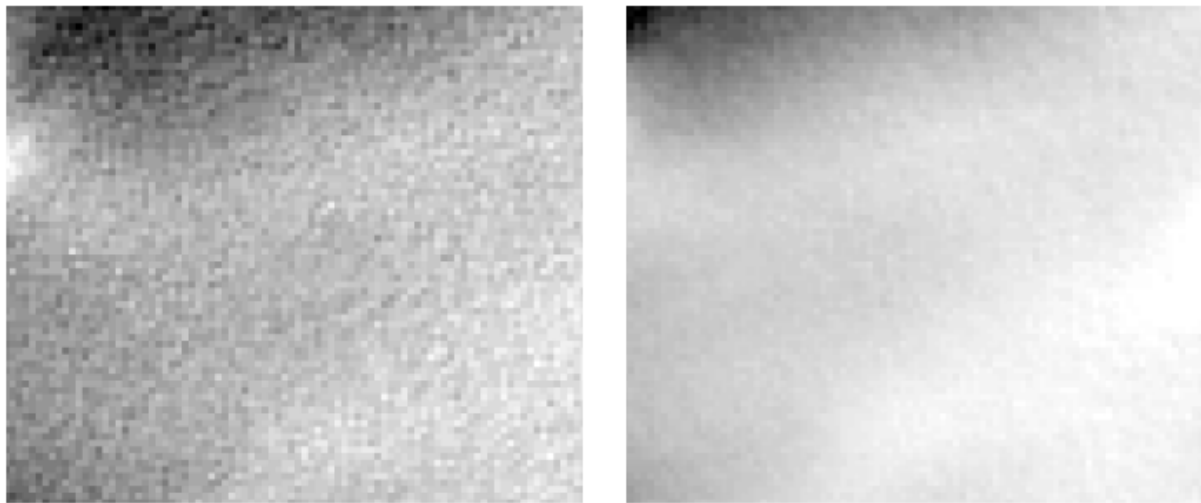


Fig 6.13: Left panel: Landsat 7 pan scene over a homogenous snow field. Right panel: Landsat 8 pan scene over the same snow field with 14 days time difference.

#### 6.1.1.3 Consequences for displacement measurement

As a consequence of the improved coregistration accuracy and radiometric fidelity of Landsat 8 OLI data, it is expected that more ice displacements can be tracked and with higher accuracy and precision. Fig. 6.14 shows a comparison of velocity fields from one Landsat 7 and one Landsat 8 scene, compared to displacements from two Landsat 8 scenes. This figure shows clearly the more complete and more consistent flow field obtained from Landsat 8 only. Figure 6.15 exemplifies that even over 20 days (neighbour orbits were used), with Landsat 8, smooth and consistent velocity fields can be obtained. Remarkably, matching worked even in zones that were in shadow in both scenes. Matching failed where shadows changed as the changes present too dominant a radiometric feature. Even over just two days, a reasonable velocity field could be obtained, though with significantly more noise.

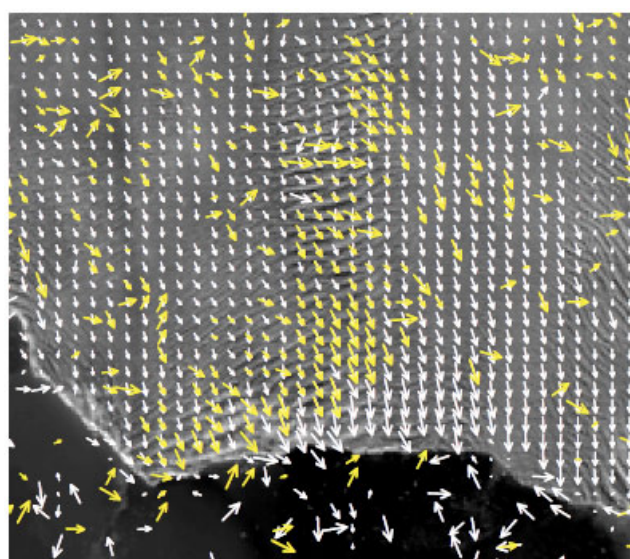
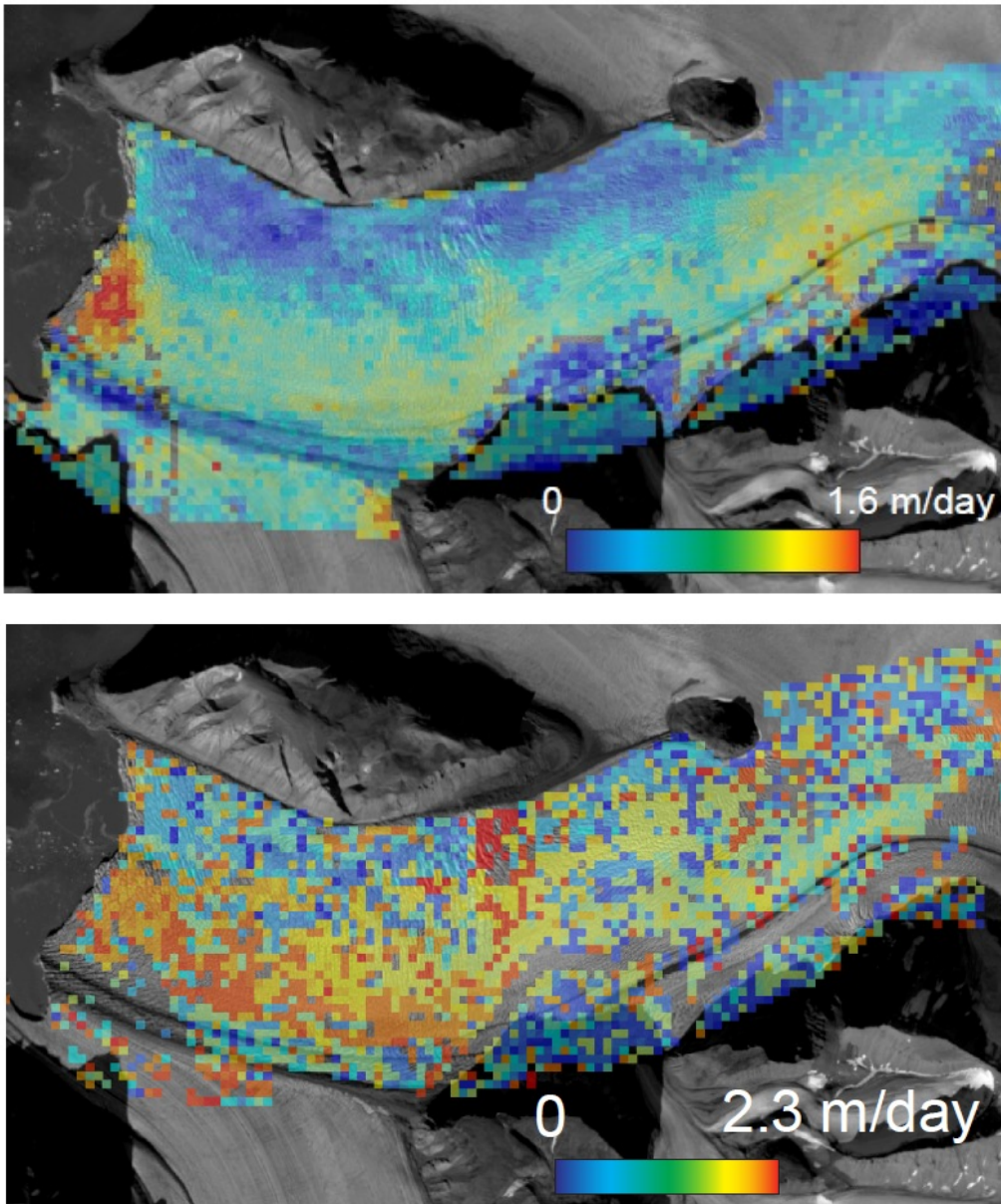


Fig. 6.14: Yellow vectors: ice flow over 45 days between a Landsat 7 pan and a Landsat 8 pan scene. White vectors: ice flow over 20 days between two Landsat 8 pan scenes. Vectors are displayed on a 100 m raster, those with low correlation coefficient have been filtered. Maximum speeds are approximately 2 m/day.



*Fig 6.15: Ice velocities over Kronebreen, Svalbard, over 20 days from two Landsat 8 pan scenes (upper panel), and over 2 days (lower panel).*

For the above reasons, as well as the Landsat 7 SLC-off data voids, Glaciers\_cci will prioritize Landsat 8 data for deriving more recent glacier velocity from optical data. For periods before 2013, only earlier Landsat instruments are available. The above considerations show however, that the quality, reliability, accuracy and relative precision of Landsat 8 derived displacement fields is considerably improved compared to Landsat 7 and earlier (see also UCR update in Glaciers\_cci, 2015).

### 6.6.2 Sentinel-2 MSI

Sentinel-2 MSI provides further improvements compared to Landsat 8 OLI (Kääb et al. 2016):

- The resolution of 10 m for bands 2-4 and 8 together with their 12-bit radiometric depth further improves offset tracking compared to Landsat 8 OLI ([Fig. 6.16](#)). Measurement of seasonal glacier velocities becomes more feasible ([Fig. 6.17](#)).
- The relative radiometric accuracy is high ( $\pm$  a few 0.0001 in TOA reflectance) and it seems possible to increase this number by improved destriping.
- The absolute geolocation accuracy seems in general high (around  $\pm$  10 m or better).
- Jitter patterns on the order of up to  $\pm$ 4 m in horizontal projection are possible but seldom.
- The DEM used for MSI data orthorectification is by necessity not strictly up to date. Vertical errors happen in particular on glacier termini and related orthorectification offsets of several 10 m were found ([Fig. 6.18](#)). This implies potential inconsistencies with Landsat data and derived products ([Fig. 6.19](#)).

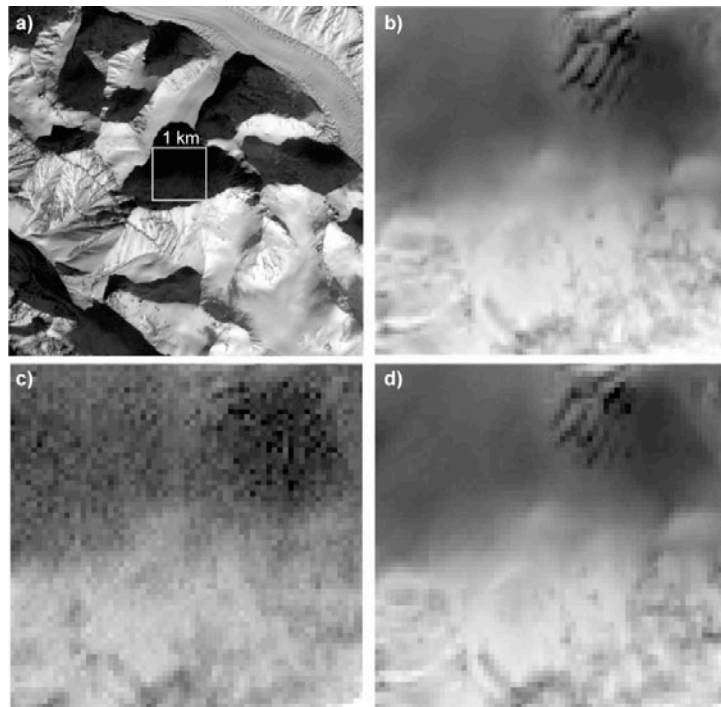


*Fig. 6.16: Dark shadow in a mountain flank in the Karakoram. a) overview with location of other panels marked by a white square of 1 × 1 km in size. b) section of a Sentinel-2A image (30.11.2015; c) Landsat 7 ETM+ (17.11.2001); (d) Landsat 8 (2.12.2015). All examples are using band 8 of the respective sensors with enhanced histogram. North to the top. Note the crevasses to the upper middle of the Sentinel-2A and Landsat 8 images.*

Tracking ice velocities between repeat Sentinel-2 data from different orbits, or between Sentinel-2 and Landsat data becomes often problematic for small displacements of a few pixels or less. In order to keep the relative velocity errors small, glacier tracking using images from different orbits should be applied only for ice displacements that are one or several orders of magnitude larger than the cross-track offsets due to DEM errors expected over the glacier studied. For repeat-orbit Sentinel-2A data, however, we find an impressive potential for ice flow measurements. The good radiometric and geometric performance of Sentinel-2 allows quantification of seasonal ice velocities even over 10-day cycles. The launch of

Sentinel-2B and with that the availability of 5-day repeat orbits will even further increase this potential, at least by reducing the probability of cloud cover. By triangulating displacement measurements between three subsequent acquisitions we show that ice velocities can be measured at least with an accuracy of 10-20% of a 10 m pixel (i.e. 1-2 m). This creates a number of new possibilities for investigating glacier flow and its spatio-temporal variations.

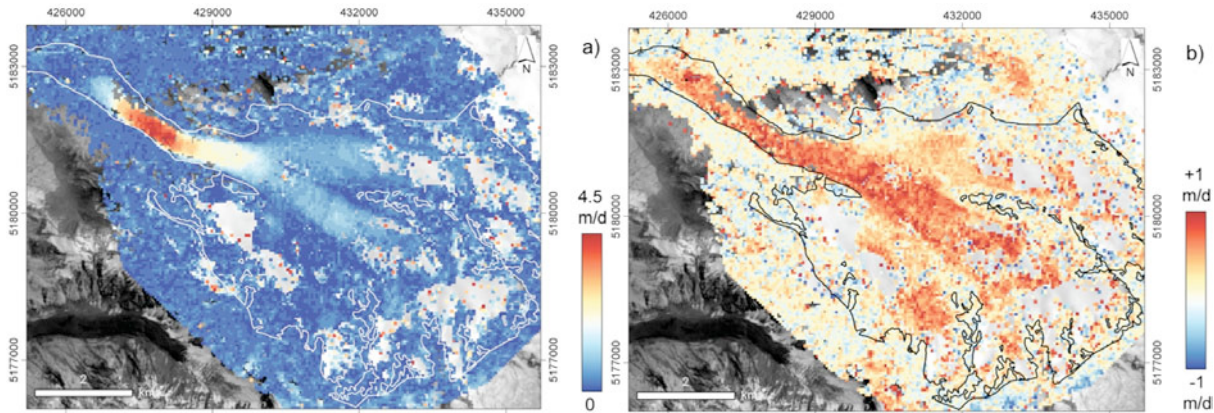


Fig. 6.17: a) ice velocities on Fox Glacier, New Zealand, from Sentinel-2A data from 24.12. 2015 and 3.1. 2016. b) Velocity differences between 24.12. 2015 and 3.1. 2016, and 3.1. 2016 and 13.1. 2016 (calculated as time 2 minus time 1 so that positive differences indicate increase in speed). Outliers have been removed based on low correlation values and residuals of the vector sum of the two 10-day displacements and the full 20-day displacements. White glacier outlines are from Gjermundsen et al. (2011). Coordinates are in UTM zone 59S.

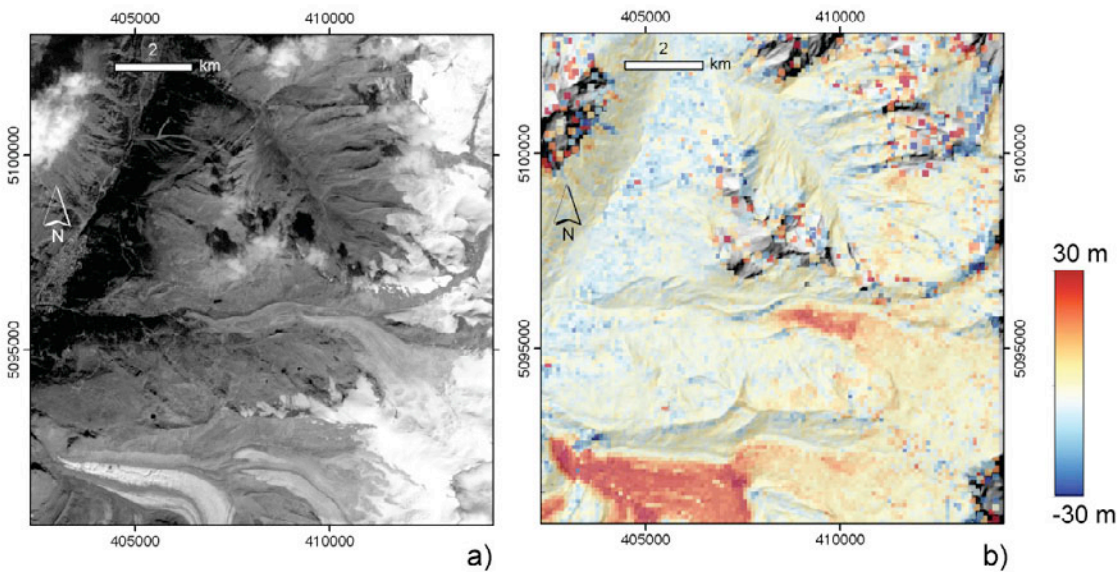


Fig. 6.18: Cross-track offsets (image b) between sections of a Landsat 8 and a Sentinel-2A (image a) scene from 8.9.2015 (10:10 and 10:30 UTC, respectively) over Zermatt, Gorner Glacier and Findelen Glacier, Swiss Alps. Data voids in the offset field are due to mismatches over clouds. Colour-coded offsets underlain by a DEM hillshade. Distinct offsets over the glaciers are due to glacier thickness loss between the date of the DEM used for orthorectification and the image acquisition in 2015.

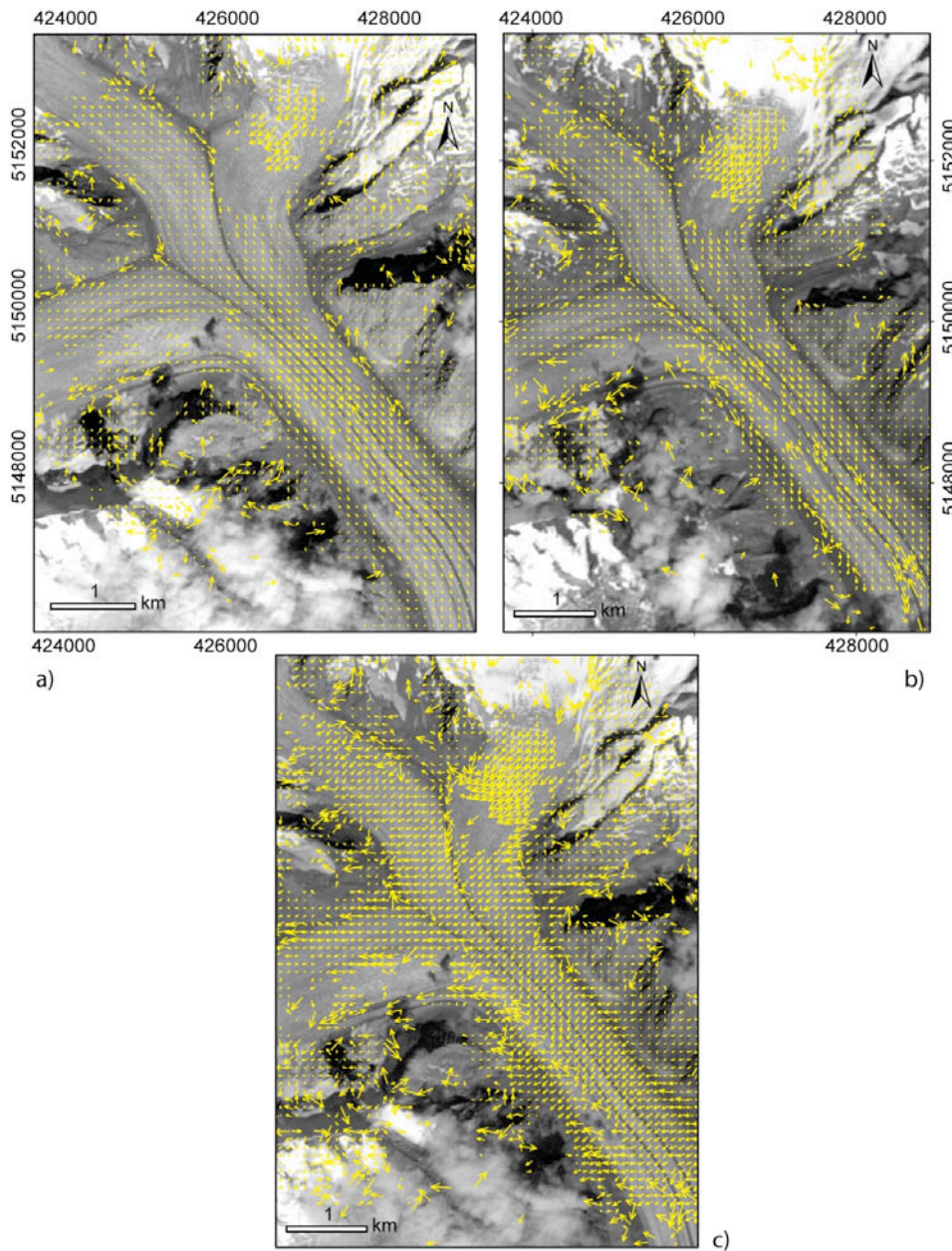


Fig 6.19: a) ice velocities between Sentinel-2 data from 30 July (background) and 8 September 2015. b) ice velocities between Landsat 8 data from 7 August (background) and 8 September 2015. c) Velocities between Landsat 8 data from 7 August and Sentinel-2 data from 8 September (background). Maximum values are ~0.8 m/d. The same matching windows (in ground size) and the same threshold for correlation coefficients have been used. Outliers have not been filtered manually. Copernicus Sentinel data 2015, Coordinates: UTM 32N.

### 6.6.3 Sentinel-1

The main new SAR sensor for monitoring the cryosphere is Sentinel-1A, launched on 3 April 2014. The SAR sensor onboard of Sentinel-1 operates at C-band in three main modes, Stripmap, Interferometric Wide Swath mode (IWS) , which applies the TOPS technology, and Extra Wide Swath Mode (EWS) (Fig 6.20).

For polar environments monitoring, major global sea-ice zones will be observed to satisfy in particular the needs from the COPERNICUS Marine (Sea-Ice) service with the EWS mode (<https://sentinel.esa.int/web/sentinel/missions/sentinel-1/observation-scenario>). However, major global ice-caps are covered at least twice a year according to local summer and winter conditions, employing IWS mode, HH polarization, and achieving at least three consecutive full coverages on each, ascending and descending passes. Global tectonic active areas, including the Himalayas, Andes and Rocky Mountains where there are large glaciers, are observed in a stable full two pass IWS mode, VV polarization coverage with a revisit frequency of 24 days per pass (alternating ascending and descending passes, i.e. a particular area is observed every 12 days, interferometric pairs are available every 24 days). The specifications of IWS mode are listed in **Table 6.3**.

Characteristic	Value
Swath width	250 km
Incidence angle range	29.1° - 46.0°
Sub-swaths	3
Azimuth steering angle	± 0.6°
Azimuth and range looks	Single
Polarisation options	Dual HH+HV, VV+VH, Single HH, VV
Maximum Noise Equivalent Sigma Zero (NESZ)	-22 dB
Radiometric stability	0.5 dB (3σ)
Radiometric accuracy	1 dB (3σ)
Phase error	5°

*Table 6.3: Characteristics of Sentinel-1 IWS mode.*

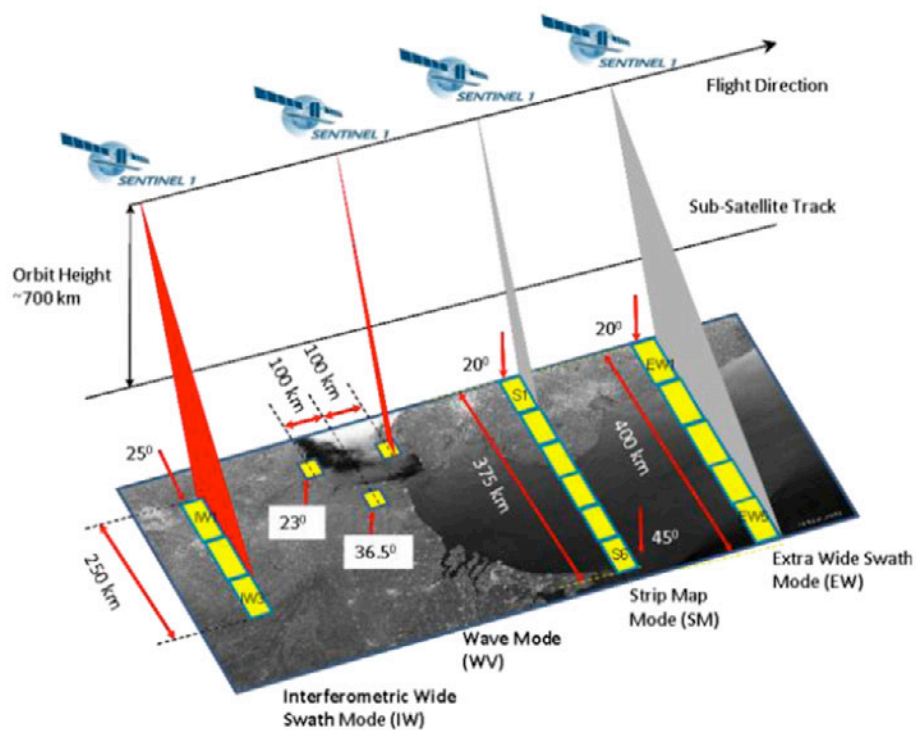


*Fig. 6.20: Acquisition modes of Sentinel-1 SAR.*

***Interferometric Wide Swath (IWS)***

Interferometric Wide Swath (IWS) data are acquired applying the TOPS technology and distributed either as Single-Look Complex (SLC) data with a slant-range pixel spacing of 2.3 m and an azimuth pixel spacing of 13.9 m or as Ground-Range Detected (GRD) data with a pixel spacing of 10 m. Required software adaptations for TOPS mode in the pre-processing of the data included:

- data import;
- burst and sub-swath stitching for real-value intensity and complex images in case of use of SLC data.

Required software adaptations for TOPS mode in the post-processing of the data included:

- geocoding of SLC and GRDH data.

Main processing (i.e. offset-tracking) is applied using the same core algorithm previously described for the other SAR sensor. Tests with the window size were performed, suggesting sizes of 256x128 or 512x128 pixels depending on glaciers and ice caps size. Normalized histograms of matches on stable ground were performed for a large series of image pairs. Standard-deviations of ground-range and azimuth estimates with SLC data are as low as 0.05 pixels, corresponding to an error in the estimation of the 2D rate of motion of about 24 m/yr (i.e.  $\text{sqrt}((2.3/\sin(35)/10) \times (2.3/\sin(35)/10) + (13.9/20) \times (13.9/20)) \times 365/12$ ).

An example of flow velocity from Sentinel-1 in the winter of 2015 is shown in Fig. 6.21 below and compared to a map derived from ALOS PALSAR in 2008. Please notice the dramatic increase in ice surface velocity of Basin 3 on the east from 2008 to 2015 and the good resolution of Sentinel-1 results over the comparatively small glaciers on Vestfonna to the west.

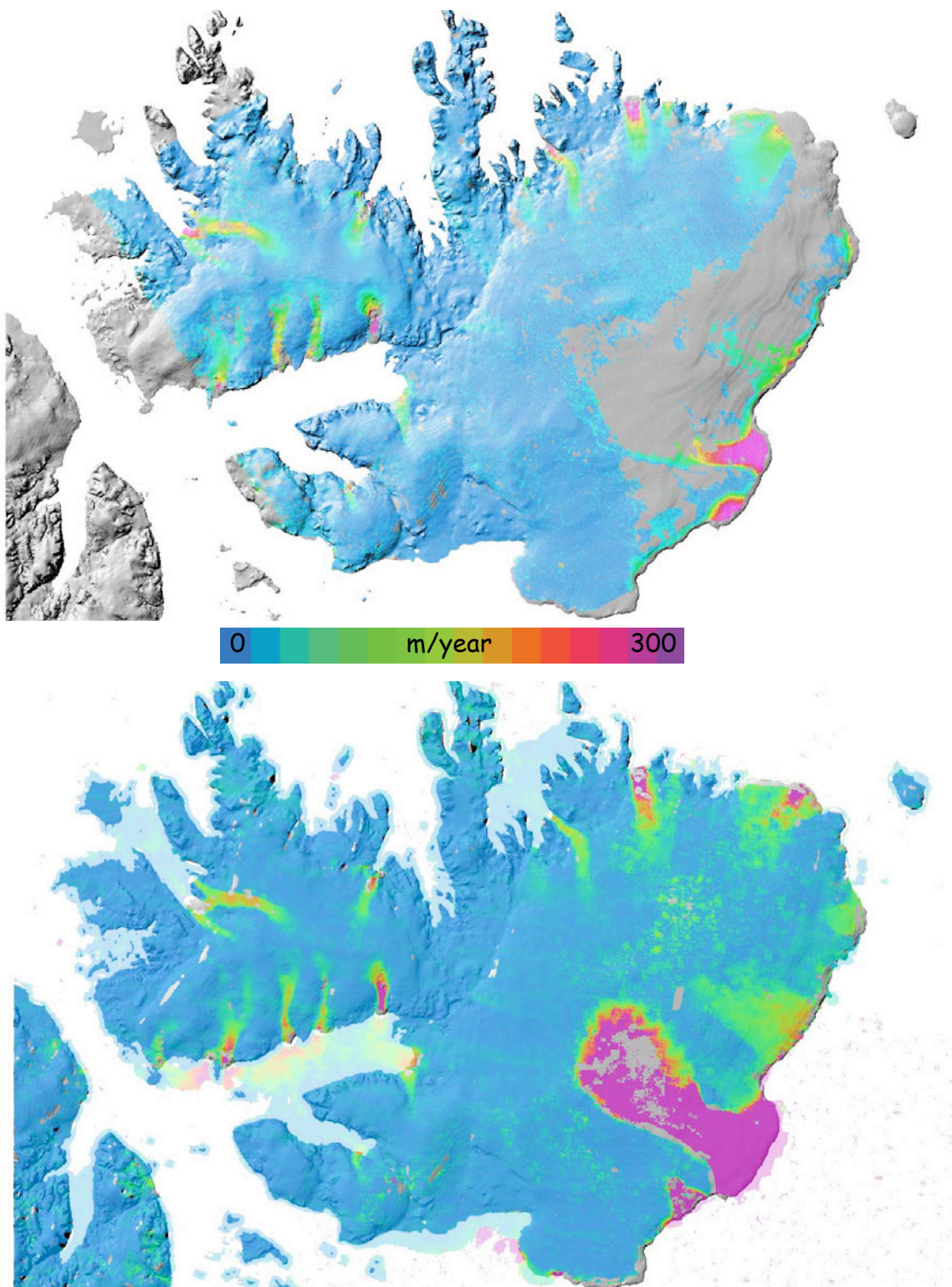


*Fig. 6.21: Flow velocities for Nordaustlandet, Svalbard. The top panel is derived from ALOS PALSAR image pairs acquired on 5.1./20.2. 2008 and 1.2./18.3. 2008. The lower panel is from Sentinel-1 pairs acquired on 21.1./02.1. 2015 and 22.1./3.2. 2015.*

### ***Extra Wide Swath Mode (EWS)***

The Extra Wide Swath Mode (EWS) data are mainly distributed as Ground-Range Detected (GRD) data with a 40 m ground-resolution. Tracking of these data was tested over the Austfonna ice-cap with acquisitions of the 19th and 31st of March 2015 ([Fig. 6.22](#)). Although the strong signal of the surging Basin 3 is visible with this image mode, the comparison with IWS data highlights the very large noise, precluding to apply Sentinel-1 EWS data for any quantitative study on changes of flow rates.

### ***Stripmap***

So far, this image mode was not considered over glaciers and ice caps.

### **6.6.4 JAXA ALOS-2 PALSAR-2**

The JAXA ALOS-2 mission was launched in May 24, 2014 and operates an L-Band SAR sensor (PALSAR-2). ALOS-2 is in a sun-synchronous orbit and has a repeat cycle of 14 days. PALSAR-2 supports 6 different acquisition modes, with different coverages and spatial resolutions. The specifications are given in [Table 6.4](#). Over land ALOS-2 PALSAR-2 acquires mainly in Fine and ScanSAR nominal modes.

		<b>Spotlight</b>	<b>Ultra Fine</b>	<b>High sensitive</b>	<b>Fine</b>	<b>ScanSAR nominal</b>		<b>ScanSAR wide</b>
Bandwidth		84MHz	84MHz	42MHz	28MHz	14MHz 28MHz		14MHz
Resolution		Rg × Az: 3 × 1m	3m	6m	10m	100m		60m
Swath		Rg × Az: 25 × 25km	50km	50km	70km	350km (5-scan)		490km (7-scan)
Polarization		SP	SP/DP	SP/DP/QP/CP			SP/DP	
NESZ		-24dB	-24dB	-28dB	-26dB	-26dB	-23dB	-23dB
S/A	Rg	25dB	25dB	23dB	25dB	25dB		20dB
	Az	20dB	25dB	20dB	23dB	20dB		20dB

*Table 6.4: Acquisition modes of ALOS-2 PALSAR.*

### ***Fine***

The major characteristics of ALOS-2 PALSAR-2 Fine mode data are similar to those of ALOS-1 PALSAR-1 Fine Beam Single (FBS) mode data, including the time interval because repeat orbits are generally expected only after three cycles (i.e. 42 days). Up to mid 2016 only a very limited number of ALOS-2 PALSAR-2 Fine mode image pairs with repeat intervals of 42 days or less was acquired over glaciers and ice caps, which allowed to broadly assess the sensor's performance but is not sufficient for large scale production.

ALOS-2 PALSAR-2 Fine images are distributed as Single-Look Complex (SLC) data with a slant-range pixel spacing of 4.3 m and an azimuth pixel spacing of 3.2 m. No special software adaptations was required for the processing of these images apart from the data import. Main processing (i.e. offset-tracking) is applied using the same core algorithm previously described for the other SAR sensors, in particular ALOS-1 PALSAR-1. Tests with the window size were performed, suggesting an optimal size of 64x192. Normalized histograms of matches performed on stable ground for a few image pairs indicate standard-deviations of horizontal estimates of 5 to 30 m/yr, depending on the amount of ionospheric contamination. An example of flow velocity from ALOS-2 PALSAR-2 in the winter of 2016 is shown in [Fig.](#)

6.23 and compared to maps derived from JERS-1 in 1998, ALOS-1 PALSAR-1 in 2008 and Sentinel-1 in 2015. Please notice the increase in ice surface velocity on the south of Novaya Zemlya, also confirmed by Sentinel-1 data, and the high level of ionospheric contamination on the northeast of Novaya Zemlya for the 2016 ALOS-2 PALSAR-2 image pair.

### ***ScanSAR***

PALSAR-2 ScanSAR data cover large swaths of 350 km, which is very attractive for large-scale studies, but spatial resolution is low. SLC's are distributed with a slant-range pixel spacing of 8.6 m and an azimuth\_pixel\_spacing of 2.4 m, however the indicated nominal spatial resolution is 100 m (<http://www.eorc.jaxa.jp/ALOS/en/about/palsar.htm>). For interferometry, burst synchronisation between the two images is required, which was not often guaranteed at the beginning of the mission but is better controlled now. A good number of PALSAR-2 ScanSAR data was acquired so far over the Arctic and Himalayas and investigations about the suitability of this sensor mode for ice velocity estimation were performed. Here, we concentrate on a winter image pair acquired over East Svalbard on 28.12.2015 and 11.01.2016.

Software adaptations was required for data import the ALOS-2 PALSAR-2 ScanSAR images. The entire processing from co-registration to geocoding is performed individually for each ScanSAR swath. Various tests for the main processing (i.e. offset-tracking) were performed using single- and multi-looked images and different window sizes. Best results were obtained after applying a multi-look factor of 1 in slant-range and 5 in azimuth, transformation of the multi-looked intensity images from linear to logarithmic scale, and using a correlation window size of 128x128 pixels. Normalized histograms of matches performed on stable ground indicate standard-deviations of horizontal estimates of 30 to 70 m/yr, depending on swath. The flow velocity over Vestfonna and Austfonna from ALOS-2 PALSAR-2 ScanSAR data is compared to that of Sentinel-1 in 2015 in Fig. 6.24. Although the strong signals of the surging Basins 2 and 3 are well visible with this image mode and the coverage with valid information is very good in the interior of the ice caps (as expected for L-band data), the comparison with Sentinel-1 IWS data highlights that the signals over the smaller basins are not well preserved, because of the low spatial resolution of the ScanSAR images, and ionospheric artefacts are often present at L-band. This is precluding for the moment to apply ALOS-2 PALSAR-2 ScanSAR data for any quantitative study on changes of flow rates on glaciers and ice caps. On the other hand, the quality of the ALOS-2 PALSAR-2 ScanSAR interferograms and backscattering intensity images is excellent.

## **6.7 Output products**

The native output products of SAR offset-tracking procedures are co-registered displacements in the satellite line-of-sight and along track components for the entire area of interest (scene coverage). For final delivery and comparison with other products, the raw satellite line-of-sight displacements are transformed to 2D velocity maps and orthorectified to a specific geographic projection. The algorithm outputs for matching optical data are horizontal displacements in the easting and northing coordinates in UTM or geographic projection (i.e. without projection to a certain flow direction) and a map of quality parameters (e.g. SNR and/or CC). The format of the products is described in detail in the PSD (Glaciers\_cci, 2014).

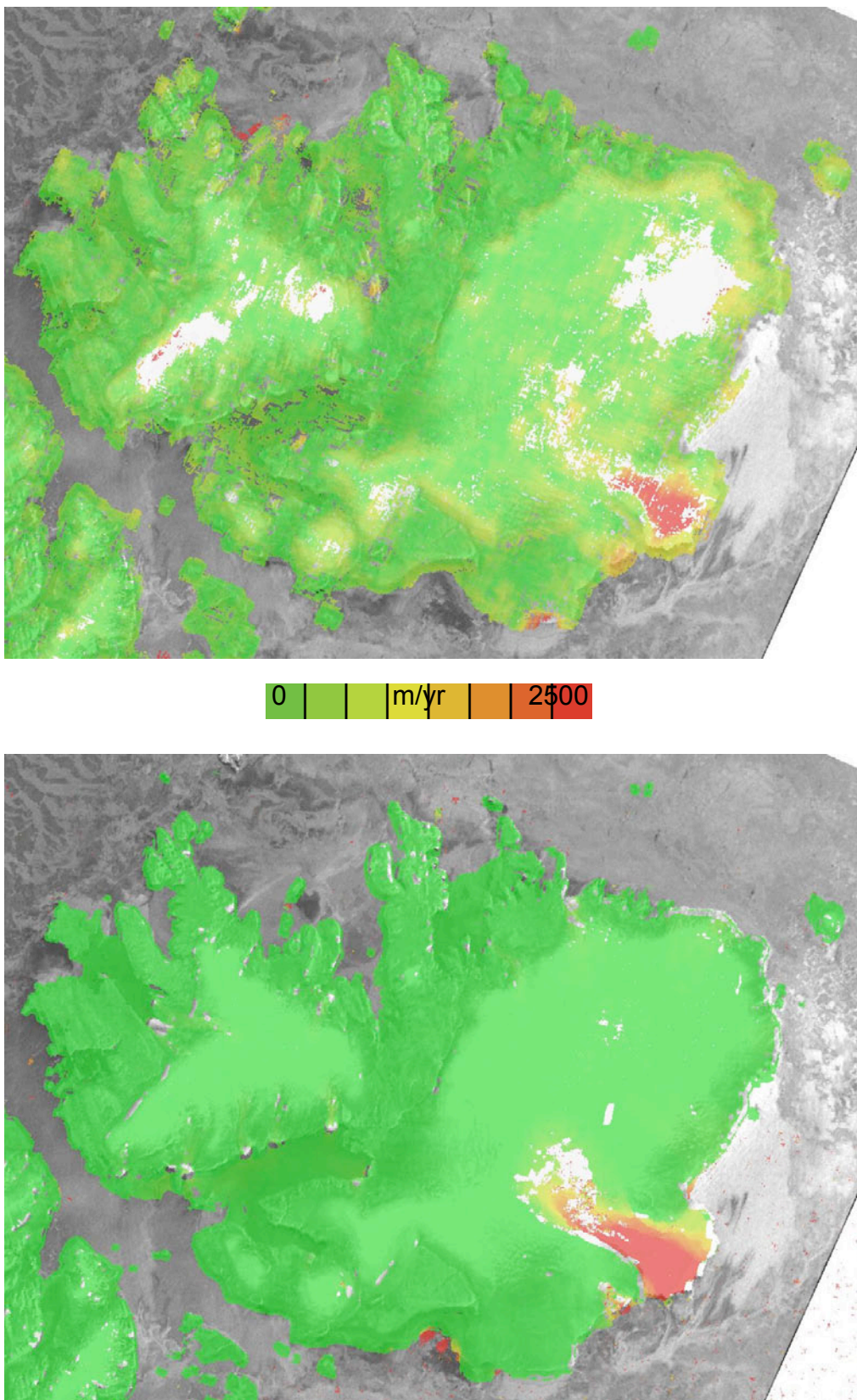
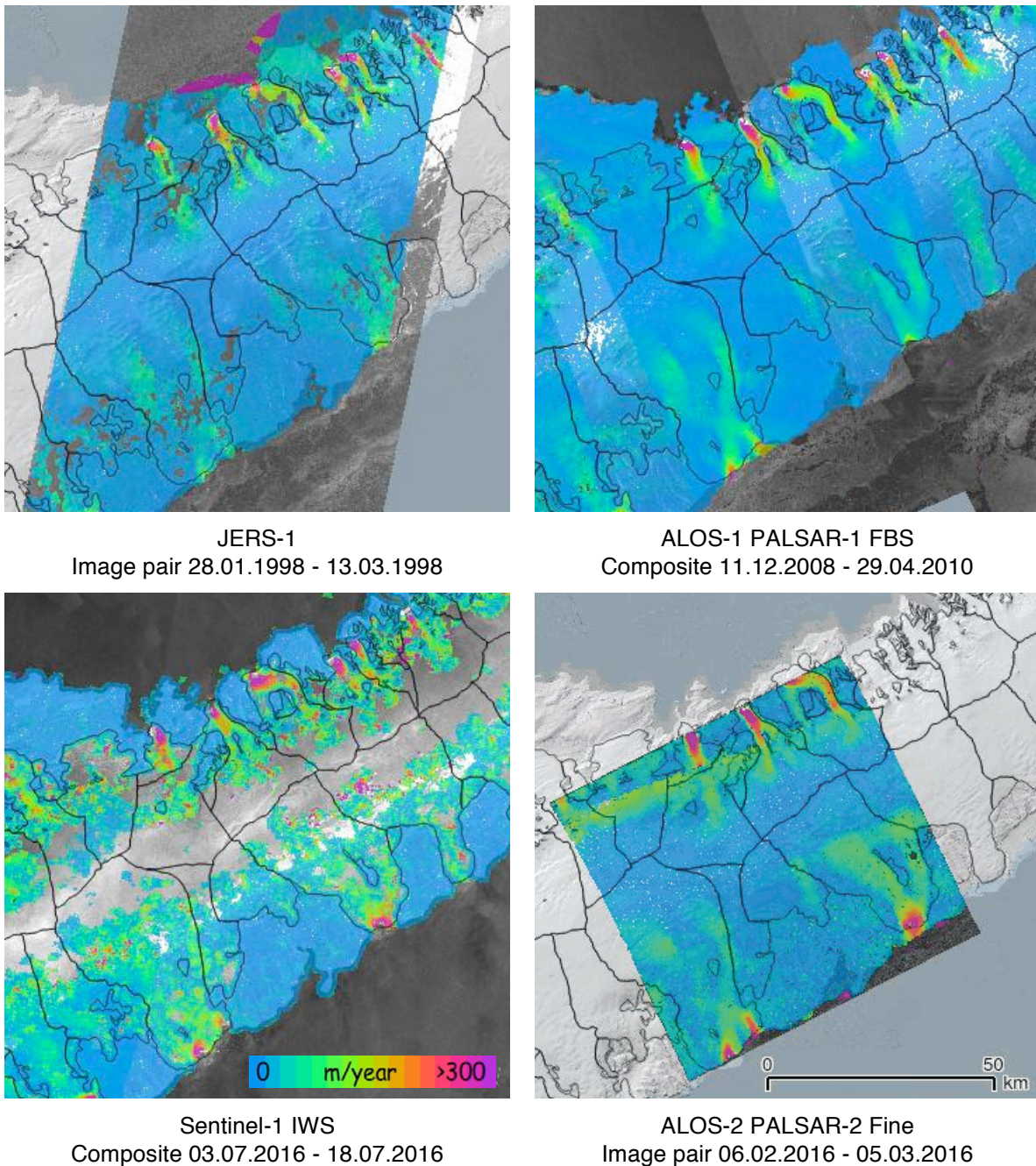
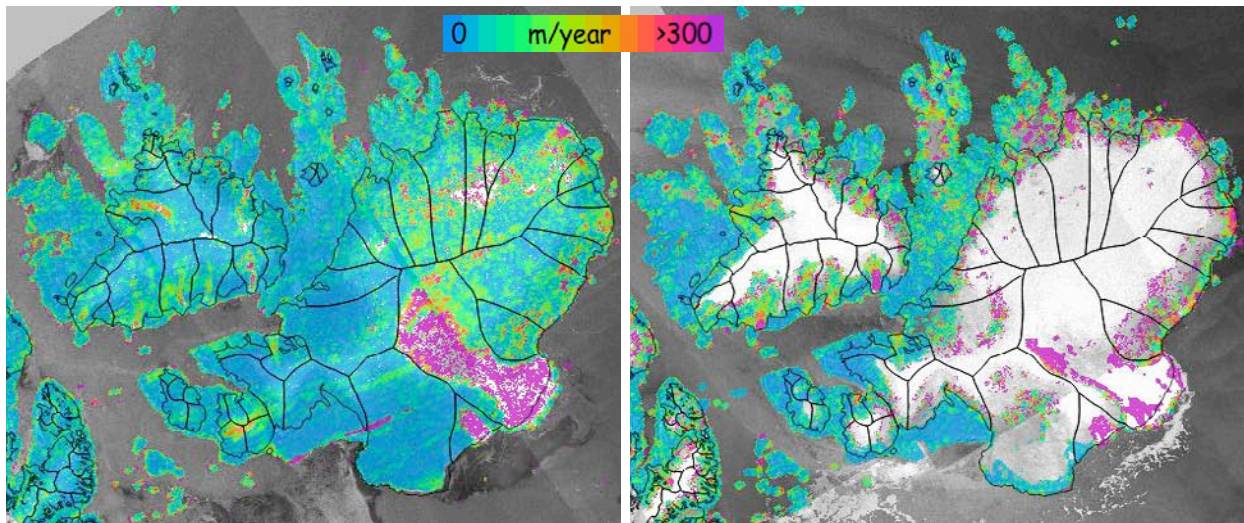
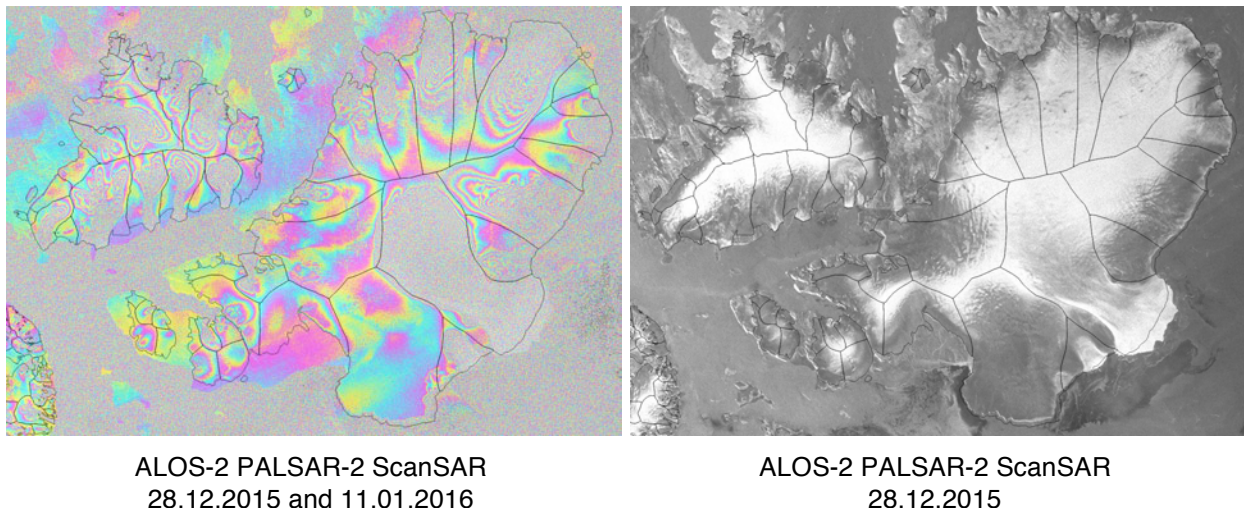


Fig. 6.22: Flow velocities for Nordaustlandet, Svalbard. The top panel is derived from Sentinel-1 EWS SLC pairs acquired on 19./31.1. and 20.1./2.2. 2015 with 10 m resolution. The lower panel is Sentinel-1 EWS GRDM from 19./31.3. 2015 with 40 m-resolution.



*Fig. 6.23: Flow velocities for part of Novaya Zemlya from top left: JERS-1; top right: ALOS - 1 PALSAR-1; bottom left: Sentinel-1 IWS; and bottom right: ALOS-2 PALSAR-2 Fine image pairs.*


 ALOS-2 PALSAR-2 ScanSAR  
 28.12.2015 and 11.01.2016

 Sentinel-1 IWS  
 Composite 03.07.2016 - 18.07.2016

 ALOS-2 PALSAR-2 ScanSAR  
 28.12.2015 and 11.01.2016

 ALOS-2 PALSAR-2 ScanSAR  
 28.12.2015

*Fig. 6.24: Top row: Flow velocities for Vestfonna and Austfonna on Svalbard from ALOS-2 PALSAR-2 ScanSAR (left) and Sentinel-1 IWS image pairs (right). Bottom row, left: ALOS-2 PALSAR-2 ScanSAR differential interferogram (IDEM used for topographic phase component removal), right: backscattering intensity image.*

## 6.8 Error budget estimates

The algorithm evaluation showed that most algorithms and implementations are in principle able to achieve precisions far into the sub-pixel range. That makes clear that the actual error budget is in practice and in most cases not dominated by the algorithm itself. The error budget of glacier displacement measurements from optical and SAR data consists of:

- the algorithm precision (subpixel, down to 1/5th to 1/10th of a pixel);
- image co-registration, including stereo offsets in the slant-range direction resulting from the different satellite orbit configurations of the two SAR images (to be checked over stable terrain where the accuracy close to matching precision possible);

- azimuth positional shifts caused by ionospheric phase delay variations (“azimuth streaking” with stronger effects at lower frequencies);
- surface changes and transformations (i.e. representativeness of surface features for ice particle displacement; e.g. shift of surface feature at sub-pixel or pixel level);
- geometric sensor noise (theoretical image-to-image registration error; sub-pixel level, but often larger than algorithm precision);
- mismatches due to similar but not corresponding features (e.g. self-similar ogives, crevasses or seracs; errors of many pixels possible);
- ability of post-processing procedures to eliminate measurement noise and mismatches;
- geocoding accuracy (e.g. influence from the DEM used for orthorectification).

## 6.9 Expected accuracy

The accuracy of individual glacier displacement measurements from repeat satellite data using optical offset-tracking is in the order of one pixel, with areas with better accuracy, but also areas and points of much lower accuracy. For SAR images we estimate the reliability of the NCC algorithm to return co-registration parameters in a typical application over glacierized regions as accurate as 1/10th of a pixel. This corresponds for the ALOS PALSAR and TerraSAR-X data separated by a temporal interval ( $ti$ ) of 46 and 11 days, respectively, to an accuracy of about 6 to 10 m/yr and for the ENVISAT ASAR data with  $ti = 35$  days to an accuracy of about 15 m/yr (based on pixel sizes in ground range and azimuth direction of 7x3, 2x2 and 14x4 m, respectively, and using the equation (for ASAR)  $\text{accuracy} = \sqrt{[1.4^2 * 0.4^2] * [365/ti]}$ ). Investigations with Sentinel-1 (S1) Interferometric Wide Swath (IWS) SAR data separated by a temporal interval ( $ti$ ) of 12 days indicate that standard deviation for stable ground matches is on order of 20 m/yr, suggesting that the reliability of the cross-correlation algorithm to return co-registration parameters with S1 IW data is more accurate than 1/20th of an image pixel based on pixel sizes in ground range and azimuth direction of 8x20 m. Reliability of the results is reduced due to frequent outliers that require special attention for optical and SAR data. Initial investigations with ALOS-2 PALSAR-2 Stripmap data suggest similar accuracy than with ALOS-1 PALSAR-1 FBS data, while for the moment production of ice surface velocity data from ALOS-2 PALSAR-2 ScanSAR data is not considered because of the low quality results obtained so far.

Both Landsat 5, 7 and 8 (and Sentinel-2 L1C) products are provided as orthoimages ensuring geolocation compatibility between the sensors as velocities are derived and provided directly in ground coordinates. Though as described above, the accuracy and quality of velocity products will vary, due to, for instance, different resolutions (Landsat 5: 30 m, Landsat 7 and 8: 15 m (pan) and 30 m, Sentinel-2: 10 m and 20 m), different radiometric properties (Landsat 5 and 7: 8 bit, Landsat 8 and Sentinel-2: 12 bit), and different error propagations of DEM errors into the provided orthoimages. These influences are minimized by matching only images from the same relative orbit and the same sensor so that compatibility between the above four sensors is maximized. The related varying accuracies are declared in the product metadata, and the varying qualities are reflected in the quality flags to each velocity measurement, or in the completeness of the velocity field, respectively, if the user thresholds the data are based on the quality flags.

## 6.10 Practical considerations for implementation

The purpose of the algorithms is to allow for a high degree of automation over large regions. In offset tracking, operator intervention can be useful, but is not necessary, for

- accepting the stable ground co-registration,
- setting the matching template sizes and search window sizes (maximum displacement expected),
- choosing a matching algorithm, and
- post-processing filtering of outliers

For a final processing scheme two complementary algorithms will be used for optical data. It is open to discussion if matching template sizes will be set by an operator, or if a set of default parameters will be used depending on the sensor type and the region of the scene (i.e. glacier type). It is also open to discussion, if a first-order filter will be applied to the result groups, providing an additional attribute containing a quality flag based on CC, SNR and low-pass filtered displacements, or if even measurements assumed to be erroneous from the filter will be removed completely.

## References

- Abermann, J., Fischer, A., Lambrecht, A. and Geist, T. (2010): On the potential of very high-resolution repeat DEMs in glacial and periglacial environments. *The Cryosphere*, 4, 53-65.
- Abshire, J.B., Sun, X.L., Riris, H., Sirota, J.M., McGarry, J.F., Palm, S., Yi, D.H. and Liiva, P. (2005): Geoscience Laser Altimeter System (GLAS) on the ICESat mission: On-orbit measurement performance, *Geophysical Research Letters*, 32, L21S02, 1-4.
- Albert, T.H. (2002): Evaluation of remote sensing techniques for ice-area classification applied to the tropical Quelccaya Ice Cap, Peru. *Polar Geography*, 26 (3), 210-226.
- Andreassen, L.M. (1999): Comparing traditional mass balance measurements with long-term volume change extracted from topographical maps: a case study of Storbreen glacier in Jotunheimen, Norway, for the period 1940–1997. *Geografiska Annaler*, 81A (4), 467-476.
- Andreassen, L.M., Paul, F., Kääb, A. and Hausberg, J.E. (2008): Landsat-derived glacier inventory for Jotunheimen, Norway, and deduced glacier changes since the 1930s. *The Cryosphere*, 2, 131-145.
- Aniya, M., Sato, H., Naruse, R., Skvarca, P. and Casassa, G. (1996): The use of satellite and airborne imagery to inventory outlet glaciers of the Southern Patagonia Icefield, South America. *Photogrammetric Engineering and Remote Sensing*, 62, 1361-1369.
- Atwood, D., Meyer, F. and Arendt, A. (2010): Using L-band SAR coherence to delineate glacier extent. *Canadian Journal of Remote Sensing*, 36, S186-S195.
- Bamber, J.L. Ice sheet altimeter processing scheme. *Int. J. Remote Sensing*, 15, 4, 925-938 (1994).
- Bayr, K. J., Hall, D.K. and Kovalick, W.M. (1994): Observations on glaciers in the eastern Austrian Alps using satellite data. *International Journal of Remote Sensing*, 15, 1733-1742.
- Berthier, E., Arnaud, Y., Vincent, C. and Rémy, F. (2006): Biases of SRTM in high-mountain areas: Implications for the monitoring of glacier volume changes. *Geophys. Res. Lett.*, 33, L08502.
- Berthier, E., Arnaud, Y., Kumar, R., Ahmad, S., Wagnon, P. and Chevallier, P. (2007): Remote sensing estimates of glacier mass balances in the Himachal Pradesh (Western Himalaya, India). *Remote Sensing of Environment*, 108, 327-338.
- Berthier, E. and Toutin, T. (2008): SPOT5-HRS digital elevation models and the monitoring of glacier elevation changes in North-West Canada and South-East Alaska. *Remote Sensing of Environment*, 112, 2443-2454.
- Berthier, E., Schiefer E., Clarke, G.K.C., Menounos, B. and Rémy, F. (2010): Contribution of Alaskan glaciers to sea-level rise derived from satellite imagery. *Nature Geoscience*, 3 (2), 92-95.
- Binaghi, E., Madella, P., Montesano, M.P. and Rampini, A. (1997): Fuzzy contextual classification of multisource remote sensing images. *IEEE Transactions on Geoscience and Remote Sensing*, GE-35 (2), 326-339.
- Bishop, M.P., Barry, R.G., Bush, A.B.G., Copeland, L., Dwyer, J.L., Fountain, A.G., Haeberli, W., Hall, D.K., Kääb, A., Kargel, J.S., Molnia, B.F., Olsenholter, J.A., Paul, F., Raup, B.H., Shroder, J.F., Trabant, D.C., Wessels, R. (2004): Global Land Ice Measurements from Space (GLIMS): Remote sensing and GIS investigations of the Earth's cryosphere. *Geocarto International*, 19 (2), 57-85.

- Bhardwaj, A., P.K. Joshi, L. Sam and Snehmani (2016): Remote sensing of alpine glaciers in visible and infrared wavelengths: a survey of advances and prospects, *Geocarto International*, 31 (5), 557-574.
- Bouillon, A., Bernard, M., Gigord, P., Orsoni, A., Rudowski, V. and Baudoin, A. (2006): SPOT 5 HRS geometric performances: Using block adjustment as a key issue to improve quality of DEM generation. *ISPRS Journal of Photogrammetry and Remote Sensing*, 60, 134-146.
- Brown G. S. (1977): The average impulse response of a rough surface and its applications. *IEEE Transactions on Antennas Propagation*, AP-25, 67-74.
- Burns, P. and Nolin, A. (2014): Using atmospherically-corrected Landsat imagery to measure glacier area change in the Cordillera Blanca, Peru from 1987 to 2010. *Remote Sensing of Environment*, 140, 165–178.
- Chavez, P. (1988): An improved dark-object subtraction technique for atmospheric scattering correction of multispectral data. *Remote Sensing of Environment*, 24, 459-479.
- Cox, L.H. and March, R.S. (2004): Comparison of geodetic and glaciological mass-balance techniques, Gulkana Glacier, Alaska, USA. *Journal of Glaciology*, 50 (170), 363-370.
- Davis, C. H. (1996): Comparison of Ice-Sheet Satellite Altimeter Retracking Algorithms. *IEEE Transactions on Geoscience and Remote Sensing*, 34, (1), 229-236.
- Davis, C.H. A robust threshold retracking algorithm for measuring ice sheet surface elevation change from satellite radar altimeters. *IEEE Trans. Geosci. Remote Sens*, 35, 4, 974 – 979 (1997).
- Davis, C.H. and V.I. Poznyak The depth of penetration in Antarctic Firn at 10 Ghz. *IEEE Trans. Geosci. Remote Sens.*, 31, 5, 1107-1111 (1993).
- Debella-Gilo, M. and Kääb, A. (2012): Locally adaptive template sizes in matching repeat images of Earth surface mass movements. *ISPRS Journal of Photogrammetry and Remote Sensing*, 69, 10-28.
- DMK/DPK (Deutschschweizerische Mathematikkommission/Physikkommission) (1977): Formeln und Tafeln. Mathematik - Statistik - Physik. Zürich, Orell Füssli Verlag.
- Dozier, J. (1989): Spectral signature of alpine snow cover from Landsat 5 TM. *Remote Sensing of Environment*, 28, 9-22.
- Duda, D.P., Spinhirne, J.D. and Eloranta, E.W. (2001): Atmospheric multiple scattering effects on GLAS altimetry. I. Calculations of single pulse bias. *IEEE Transactions on Geoscience and Remote Sensing*, 39(1), 92 -101.
- Elachi, C. Spaceborne Radar Remote Sensing: Applications and Techniques, IEEE Press, New York (1988).
- Eloranta, E. W. (1998): A practical model for lidar multiple scattering. *Appl. Opt.*, 37, 2464-2472.
- Elsberg, D.H., W.D. Harrison, K.A. Echelmeyer and R.M. Krimmel (2001): Quantifying the effects of climate and surface change on glacier mass balance. *Journal of Glaciology*, 47 (159), 649-658.
- ESA Online News Bulletin (2007): Sentinel-3 The Ocean and Medium-Resolution Land Mission for GMES Operational Services, ESA Bulletin 131.
- Farr, T. G., Rosen, P. A., Caro, E., Crippen, R., Duren, R., Hensley, S., Kobrick, M., Paller, M., Rodriguez, E., Roth, L., Seal, D., Shaffer, S., Shimada, J., Umland, J., Werner, M., Oskin, M., Burbank, D. and Alsdorf, D. (2007): The Shuttle Radar Topography Mission. *Rev. Geophys.*, 45, RG2004.
- Fitch, A.J., Kadyrov, A., Christmas, W.J. and Kittler, J. (2002): Orientation correlation. *British Machine Vision Conference*, 133-142.

- Frey, H. Paul, F. and Strozzi, T. (2012): Compilation of a glacier inventory for the western Himalayas from satellite data: Methods, challenges and results. *Remote Sensing of Environment*, 124, 832-843.
- Ficker, H.A., Borsa, A., Minster, B., Carabajal, C., Quinn, K. and Bills, B. (2005): Assessment of ICESat performance at the Salar de Uyuni, Bolivia. *Geophysical Research Letters*, 32 (L21S06), 1-5.
- Fu, L.L. and A. Cazenave (2001): *Satellite Altimetry and Earth Sciences: A Handbook of Techniques and Applications*. International Geophysics Series Vol. 69, Academic Press, San Diego, 457 pp.
- Fujisada, H., Bailey, G., Kelly, G., Hara, S. and Abrams, M. (2005): ASTER DEM performance. *IEEE Transactions on Geoscience and Remote Sensing*, 43, 2707-2714.
- Förstner, W. (1982): On the geometric precision of digital image correlation. *ISPRS Symposium Mathematical Models, Accuracy Aspects and Quality Control*, 176-189.
- Förstner, W. (2000): Image preprocessing for feature extraction in digital intensity, color and range images. In: A. Dermanis, A. Grün and F. Sansò (Eds.), *Geomatic Methods for the Analysis of Data in the Earth Sciences. Lecture Notes in Earth Sciences*. Springer. 165-189.
- Gardelle, J., Berthier, E. and Arnaud, Y. (2012): Impact of resolution and radar penetration on glacier elevation changes computed from DEM differencing. *Journal of Glaciology*, 58 (208), 419-422.
- Gardner, A.S., Moholdt, G., Wouters, B., Wolken, G., Burgess, D., Sharp, M., Cogley, J., Braun, C. and Labine, C. (2011): Sharply increased mass loss from glaciers and ice caps in the Canadian Arctic Archipelago. *Nature*, 473, 357-360.
- Geist, T., E. Lutz and J. Stötter. (2003): Airborne laser scanning technology and its potential for applications in glaciology. In *Proceedings of the ISPRS Workshop on 3-D Reconstruction from Airborne Laserscanner and INSAR Data*. Dresden, International Society for Photogrammetry and Remote Sensing, 101-106.
- Geist, T., Elvehøy, H., Jackson, M. and Stötter, J. (2005): Investigations on intra-annual elevation changes using multi-temporal airborne laser scanning data: case study Engabreen, Norway. *Annals of Glaciology*, 42, 195-201.
- Gjermundsen, E.F., Mathieu, R., Kääb, A., Chinn, T., Fitzharris, B. and Hagen, J.O. (2011): Assessment of multispectral glacier mapping methods and derivation of glacier area changes, 1978-2002, in the central Southern Alps, New Zealand, from ASTER satellite data, field survey and existing inventory data. *Journal of Glaciology*, 57 (204), 667-683.
- Glaciers\_cci (2011a): User Requirements Document (URD): Prepared by the Glaciers\_cci consortium, 45 pp.
- Glaciers\_cci (2011b): Product Specifications Document (PSD): Prepared by the Glaciers\_cci consortium, 43 pp.
- Glaciers\_cci (2011c): Data Access Requirements Document (DARD): Prepared by the Glaciers\_cci consortium, 46 pp.
- Glaciers\_cci (2012a): Algorithm Theoretical Basis Document version 0 (ATBDv0): Prepared by the Glaciers\_cci consortium, 95 pp.
- Glaciers\_cci (2012b): Product Validation and Algorithm Selection Report (PVASR): Prepared by the Glaciers\_cci consortium, 113 pp.
- Glaciers\_cci (2013a): Algorithm Theoretical Basis Document version 1 (ATBDv1): Prepared by the Glaciers\_cci consortium, 96 pp.
- Glaciers\_cci (2013b): Input/Output Data Definition version 1 (IODDv1): Prepared by the Glaciers\_cci consortium, 26 pp.

- Glaciers\_cci (2013c): Detailed Processing Model version 1 (DPMv1): Prepared by the Glaciers\_cci consortium, 86 pp.
- Glaciers\_cci (2013d): Uncertainty Characterisation Report v1 (UCRv1): Prepared by the Glaciers\_cci consortium, 22 pp.
- Glaciers\_cci (2013e): Algorithm Theoretical Basis Document version 2 (ATBDv2): Prepared by the Glaciers\_cci consortium, 81 pp.
- Glaciers\_cci (2014a): User Requirements Document (URD): Prepared by the Glaciers\_cci consortium, 18 pp.
- Glaciers\_cci (2014b): Data Access Requirements Document (DARD): Prepared by the Glaciers\_cci consortium, 25 pp.
- Glaciers\_cci (2015): Uncertainty Characterisation Report v2 (UCRv2) Phase 2 Year 2: Prepared by the Glaciers\_cci consortium, 34 pp.
- Green, R. O., Dozier, J., Roberts, D. A. and Painter, T. H. (2002): Spectral snow reflectance models for grain size and liquid water fraction in melting snow for the solar reflected spectrum. *Annals of Glaciology*, 34, 71-73.
- Haeberli, W. (2006): Integrated perception of glacier changes: a challenge of historical dimensions. In: Knight, P.G. (ed.): *Glacier science and environmental change*. Oxford: Blackwell Publishing, 423-430.
- Hagen, J.O., Eiken, T., Kohler, J. and Melvold, K. (2005): Geometry changes on Svalbard glaciers: mass-balance or dynamic response? *Annals of Glaciology*, 42, 255-261.
- Hall, D. K. and Martinec, J. 1985. *Remote Sensing of Ice and Snow*. Chapman and Hall. 189 pp.
- Hall, D.K., Chang, A.T.C. and Siddalingaiah, H. (1988): Reflectances of glaciers as calculated using Landsat 5 Thematic Mapper data. *Remote Sensing of Environment*, 25, 311-321.
- Hall, D. K. Bindschadler, R. A., Foster, J. L., Chang, A. T. C., and Siddalingaiah, H. (1990): Comparison of in situ and satellite derived reflectances of Forbindels Glacier, Greenland. *International Journal of Remote Sensing*, 11(3), 493-504.
- Hall, D. K., Forster, J. L., Irons, J. R. and Dabney, P. W. (1993): Airborne bidirectional radiances of snow covered surfaces in Montana, USA. *Annals of Glaciology*. 17, 35-40
- Hall, D.K., Williams, R.S., Barton, J.S. Sigurdsson, O. Smith, L.C. and Garvin, J.B. (2000): Evaluation of remote-sensing techniques to measure decadal-scale changes of Hofsjokull ice cap, Iceland. *Journal of Glaciology*, 46 (154), 375-388.
- Heid, T. and Kääb, A. (2012a): Evaluation of different image matching methods for deriving glacier surface displacements globally from optical satellite imagery. *Remote Sensing and Environment*, 118, 339-355.
- Heid, T. and Kääb, A. (2012b): Repeat optical satellite images reveal widespread and long term decrease in land-terminating glacier speeds. *The Cryosphere*, 6, 467-478.
- Hirano, A., Welch, R. and Lang, H. (2003): Mapping from ASTER stereo image data: DEM validation and accuracy assessment. *ISPRS Journal of Photogrammetry and Remote Sensing*, 57, 356-370.
- Holobaca, I.-H. (2013): Glacier Mapper – a new method designed to assess change in mountain glaciers. *International Journal of Remote Sensing*, 34 (23), 8475-8490.
- Howat, I.M., Smith, B.E., Joughin, I. and Scambos, T.A. (2008): Rates of southeast Greenland ice volume loss from combined ICESat and ASTER observations. *Geophysical Research Letters*, 35, L17505.
- Huggel, C., Kääb, A., Haeberli, W., Teyssiere, P. and Paul, F. (2002): Remote sensing based assessment of hazards from glacier lake outbursts: a case study in the Swiss Alps. *Canadian Geotechnical Journal*, 39 (2), 316-330.

- Huss, M., Bauder, A. and Funk, M. (2009): Homogenization of long term mass-balance time series. *Annals of Glaciology*, 50 (50), 198-206.
- Huss, M. (2011): Present and future contribution of glaciers to runoff from macroscale drainage basins in Europe. *Water Resources Research*, 47, W07511.
- Höhle, J. and Höhle, M. (2009). Accuracy assessment of digital elevation models by means of robust statistical methods. *Isprs Journal of Photogrammetry and Remote Sensing*, 64, 398-406
- IGOS (2007): Integrated Global Observing Strategy Cryosphere theme report - For the monitoring of our environment from space and from Earth. Geneva: World Meteorological Organization. WMO/TD-No. 1405, 100 pp.
- Iwasaki, A. and Fujisada, H. (2005): ASTER geometric performance, Geoscience and Remote Sensing. *IEEE Transactions on Geoscience and Remote Sensing*, 43, 2700-2706.
- Jacobs, J.D., Simms, E.L. and Simms, A. (1997): Recessional of the southern part of Barnes Ice Cap, Baffin Island, Canada, between 1961 and 1993, determined from digital mapping of Landsat TM. *Journal of Glaciology*, 43 (143), 98-102.
- Jin, Z., and Simpson, J. J. (1999): Bidirectional anisotropic reflectance of snow and sea ice in AVHRR channel 1 and 2 spectral regions – Part 1: theoretical analysis. *IEEE Transactions on Geoscience and Remote Sensing*. 37, (1) 543-554.
- JPL (2011): ASTER spectral library Version 2.0. Online at: <http://speclib.jpl.nasa.gov/>
- Kääb, A. (2005): Remote Sensing of Mountain Glaciers and Permafrost Creep. *Schriftenreihe Physische Geographie. Glaziologie und Geomorphodynamik*. 48. University of Zurich, Zurich.
- Kääb, A. (2008): Glacier Volume Changes Using ASTER Satellite Stereo and ICESat GLAS Laser Altimetry, A Test Study on Edgeya, Eastern Svalbard, *IEEE Transactions on Geoscience and Remote Sensing*, 46, 2823-2830.
- Kääb, A. and Vollmer, M. (2000): Surface geometry, thickness changes and flow fields on creeping mountain permafrost: automatic extraction by digital image analysis. *Permafrost and Periglacial Processes*. 11(4), 315-326.
- Kääb, A., Paul, F., Maisch, M., Hoelzle, M. and Haeberli, W. (2002): The new remote-sensing-derived Swiss glacier inventory: II. First Results. *Annals of Glaciology*, 34, 362-366.
- Kääb, A., Huggel, C., Paul, F., Wessels, R., Raup, B., Kieffer, H. and Kargel, J. (2002): Glacier monitoring from ASTER imagery: Accuracy and Applications. *Proceedings of EARSeL-LISSIG Workshop Observing our Cryosphere from Space*, 2,43-53.
- Kääb, A., Huggel, C., Fischer, L., Guex, S., Paul, F., Roer, I., Salzmann, N., Schlaefli, S., Schmutz, K., Schneider, D., Strozzi, T. and Weidmann, W. (2005): Remote sensing of glacier- and permafrost-related hazards in high mountains: an overview. *Natural Hazards and Earth System Sciences*, 5, 527-554.
- Kääb, A., Berthier, E., Nuth, C., Gardelle, J., and Arnaud, Y. (2012): Contrasting patterns of early twenty-first-century glacier mass change in the Himalayas. *Nature*. 488(7412), 495-498
- Kääb, A., Winsvold, S. H., Altena, B., Nuth, C., Nagler, T., and Wuite, J. (2016): Glacier remote sensing using Sentinel-2. Part I: Radiometric and geometric performance, and application to ice velocity. *Remote Sensing*, 8(7), 598.
- Kaufmann, V. and Ladstädter, R. (2003): Quantitative analysis of rock glacier creep by means of digital photogrammetry using multi-temporal aerial photographs: two case studies in the Austrian Alps. *Eighth International Conference on Permafrost*, 1, Balkema, 525-530.

- Klein A.G. and Isacks, B.L. (1999): Spectral mixture analysis of Landsat Thematic Mapper images applied to the detection of the transient snowline on tropical Andean glaciers. *Global and Planetary Change*, 22, 139-154.
- Knap, W.H. and Reijmer, C.H. (1998): Anisotropy of the reflected radiation field over melting glacier ice: measurements in Landsat TM bands 2 and 4. *Remote Sensing of the Environment*. 65, 93-104
- Korona, J., Berthier, E., Bernard, M., Rémy, F. and Thouvenot, E. (2009): SPIRIT. SPOT 5 stereoscopic survey of Polar Ice: Reference Images and Topographies during the fourth International Polar Year (2007-2009): *ISPRS Journal of Photogrammetry and Remote Sensing*, 64, 204-212.
- König, M., Winther, J-G. and Isaksson, E. (2001): Measuring snow and glacier ice properties from satellites. *Reviews of Geophysics*, 39(1), 1-27
- Larsen, C.F., Motyka, R.J., Arendt, A.A., Echelmeyer, K.A. and Geissler, P.E. (2007): Glacier changes in southeast Alaska and northwest British Columbia and contribution to sea level rise. *Journal of Geophysical Research-Earth Surface*, 112, F01007.
- Le Bris, R., Paul, F., Frey, H. and Bolch, T. (2011): A new satellite-derived glacier inventory for western Alaska. *Annals of Glaciology*, 52 (59), 135-143.
- Le Bris, R. and Paul, F. (2015): Glacier-specific elevation changes in western Alaska. *Annals of Glaciology*, 56 (70), 184-192.
- Lee, D., J. Storey, M. Choate, R. (2004): Hayes Four years of Landsat-7 on-orbit geometric calibration and performance. *IEEE Transactions on Geoscience and Remote Sensing*, 42 (12), 2786–2795.
- Le Grésy B. and F. Rémy (1998): Using the temporal variability of satellite radar altimetric observations to map surface properties of the Antarctic ice sheet. *J. Glaciol.*, 44, 147, 197–206.
- Le Grésy, B., F. Papa, F. Rémy, G. Vinay, M. Van den Bosh and O.Z. Zanife (2005): ENVISAT radar altimeter measurements over continental surfaces and ice caps using the ICE-2 retracking algorithm. *Remote Sensing of Environment*, 95, 150–163.
- Leprince, S., Ayoub, F., Klinger, Y. and Avouac, J.P. (2007): Co-Registration of Optically Sensed Images and Correlation (COSI-Corr): an operational methodology for ground deformation measurements. *IGARSS: 2007 IEEE International Geoscience and Remote Sensing Symposium*, Vols 1-12, 1943-1946.
- Lillesand, T., Kiefer, R. and Chipman, J. (2004): *Remote Sensing and Image Interpretation*, 5 editon, John Wiley & Sons, Inc., Hoboken, NJ.
- Martin, T.V., Zwally, H.J., Brenner A.C. and Bindschadler R.A. (1983): Analysis and retracking of continental ice sheet radar altimetry wave-forms. *Journal of Geophysical Research*, 88, 1608-1616.
- Mätzler, C. (1996): Microwave permittivity of dry snow. *IEEE Transactions on Geoscience and Remote Sensing*, 34 (2), 573-581.
- Mavrocordatos C., Berruti B., Aguirre M. and Drinkwater M. (2007): The Sentinel-3 mission and its Topography element. *Proceeding of IEEE IGARSS 2007*, Barcelona, Spain.
- McMillan, M., Shepherd, A., Sundal, A., Briggs, K., Muir, A., Ridout, A., Hogg, A., and Wingham, D. (2014): Increased ice losses from Antarctica detected by CryoSat-2. *Geophysical Research Letters*, 41(11), 3899-3095.
- Middleton, W.E.K. and Mungall, A.G. (1952): The luminous directional reflectance of snow. *Journal middleton and mungall*, 1952 scatteringof the Optical Society of America, 42, 572-579.
- Moholdt, G., Hagen, J.O., Eiken, T. and Schuler, T.V. (2010a): Geometric changes and mass balance of the Austfonna ice cap, Svalbard. *The Cryosphere*, 4, 21-34.

- Moholdt, G., Nuth, C., Hagen, J.O. and Kohler, J. (2010b): Recent elevation changes of Svalbard glaciers derived from ICESat laser altimetry. *Remote Sensing of Environment*, 114 (11), 2756-2767.
- Mohr, J.J. and Madsen, S.N. (1996) Multi-pass interferometry for studies of glacier dynamics, *ESA Workshop Applicat. ERS SAR Interferometry: FRINGE'96*: Univ. Zurich.
- Müller, K. (2011): Microwave penetration in polar snow and ice: Implications for GPR and SAR, PhD Thesis: Department of Geosciences, University of Oslo.
- Nagai, H., Fujita, K., Sakai, A., Nuimura, T. and Tadono, T. (2016): Comparison of multiple glacier inventories with a new inventory derived from high-resolution ALOS imagery in the Bhutan Himalaya. *The Cryosphere*, 10, 65-85.
- Nuth, C., Moholdt, G., Kohler, J., Hagen, J.O. and Kääb, A. (2010): Svalbard glacier elevation changes and contribution to sea level rise. *Journal of Geophysical Research*, 115 (F1), F01008.
- Nuth, C. and Kääb, A. (2011): Co-registration and bias corrections of satellite elevation data sets for quantifying glacier thickness change. *The Cryosphere*, 5, 271-290.
- Nuth C., Schuler T.V., Kohler J., Altena B. and Hagen J.O. (2012): Estimating the long term calving flux of Kronebreen, Svalbard, from geodetic elevation changes and mass balance modelling, *Journal of Glaciology*.
- Paul, F. (2001): Evaluation of different methods for glacier mapping using Landsat TM. *EARSeL Workshop on Remote Sensing of Land Ice and Snow*, Dresden, 16.-17.6.2000. *EARSeL eProceedings*, 1, 239-245.
- Paul, F. (2002): Changes in glacier area in Tyrol, Austria, between 1969 and 1992 derived from Landsat 5 TM and Austrian Glacier Inventory data. *International Journal of Remote Sensing*, 23 (4), 787-799.
- Paul, F. (2008): Calculation of glacier elevation changes with SRTM: is there an elevation-dependent bias? *Journal of Glaciology*, 54 (188), 945-946.
- Paul, F. (2010): Towards a global glacier inventory from satellite data. *Geographica Helvetica*, 65 (2), 103-112.
- Paul, F. and Kääb, A. (2005): Perspectives on the production of a glacier inventory from multispectral satellite data in the Canadian Arctic: Cumberland Peninsula, Baffin Island. *Annals of Glaciology*, 42, 59-66.
- Paul, F. and Haeberli, W. (2008): Spatial variability of glacier elevation changes in the Swiss Alps obtained from two digital elevation models, *Geophysical Research Letters*, 35, L21502.
- Paul, F. and Andreassen, L.M. (2009): A new glacier inventory for the Svartisen region, Norway, from Landsat ETM+ data: challenges and change assessment. *Journal of Glaciology*, 55 (192), 607-618.
- Paul, F. and Hendriks, J. (2010): Optical remote sensing of glaciers. In: Pellikka, P. and Rees, W.G (Eds.), *Remote Sensing of Glaciers - Techniques for Topographic, Spatial and Thematic Mapping of Glaciers*. CRC Press, Taylor and Francis Group, Leiden, 137-152.
- Paul, F., Kääb, A., Maisch, M., Kellenberger, T. and Haeberli, W. (2002): The new remote-sensing-derived Swiss glacier inventory: I. Methods. *Annals of Glaciology*, 34, 355-361.
- Paul, F., Huggel, C., Kääb, A. and Kellenberger, T. (2003): Comparison of TM-derived glacier areas with higher resolution data sets. *EARSeL Workshop on Remote Sensing of Land Ice and Snow, Bern*, 11.-13.3.2002. *EARSeL eProceedings*, 2, 15-21.
- Paul, F., Huggel, C. and Kääb, A. (2004): Combining satellite multispectral image data and a digital elevation model for mapping of debris-covered glaciers. *Remote Sensing of Environment*, 89 (4), 510-518.

- Paul, F., Barry, R., Cogley, G., Frey, H., Haeberli, W., Ohmura, A., Ommanney, S., Raup, B., Rivera, A., Zemp, M. (2009): Recommendations for the compilation of glacier inventory data from digital sources. *Annals of Glaciology*, 50 (53), 119-126.
- Paul, F. and Hendriks, J. (2010): Optical remote sensing of glaciers. In: Pellikka, P. and Rees, W.G (Eds.), *Remote Sensing of Glaciers - Techniques for Topographic, Spatial and Thematic Mapping of Glaciers*. CRC Press, Taylor and Francis Group, Leiden, 137-152.
- Paul, F., Andreassen, L.M. and Winsvold, S.H. (2011a): A new glacier inventory for the Jostedalsbreen region, Norway, from Landsat TM scenes of 2006 and changes since 1966. *Annals of Glaciology*, 52 (59), 144-153
- Paul, F., Frey, H. and Le Bris, R. (2011b): A new glacier inventory for the European Alps from Landsat TM scenes of 2003: Challenges and results. *Annals of Glaciology*, 52 (59), 144-152.
- Paul, F., N. Barrand, E. Berthier, T. Bolch, K. Casey, H. Frey, S.P. Joshi, V. Konovalov, R. Le Bris, N. Mölg, G. Nosenko, C. Nuth, A. Pope, A. Racoviteanu, P. Rastner, B. Raup, K. Scharrer, S. Steffen and S. Winsvold (2013): On the accuracy of glacier outlines derived from remote sensing data. *Annals of Glaciology*, 54 (63), 171-182.
- Paul, F. and 24 others (2015): The Glaciers Climate Change Initiative: Algorithms for creating glacier area, elevation change and velocity products. *Remote Sensing of Environment*, 162, 408-426.
- Paul, F., S.H. Winsvold, A. Kaab, T. Nagler and G. Schwaizer (2016): Glacier Remote Sensing Using Sentinel-2. Part II: Mapping Glacier Extents and Surface Facies, and Comparison to Landsat 8. *Remote Sensing*, 8(7), 575; doi:10.3390/rs8070575.
- Pritchard, H., Murray, T., Luckman, A., Strozzi, T and Barr, S. (2005): Glacier surge dynamics of Sortebræ, east Greenland, from synthetic aperture radar feature tracking. *Journal of Geophysical Research*, 110, F03005.
- Pritchard, H.D., Arthern, R.J., Vaughan, D.G. and Edwards, L.A. (2009): Extensive dynamic thinning on the margins of the Greenland and Antarctic ice sheets. *Nature*, 461, 971-975.
- Quincey, D.J. and Glasser, N.F. (2009): Morphological and ice-dynamical changes on the Tasman Glacier, New Zealand, 1990-2007. *Global and Planetary Change*, 68(3), 185-197.
- Qunzhu, Z., Meisheng, C., Xuezhi, F., Fengxian, L., Xianzhang, C. and Wenkuna, S. (1983): A study of spectral reflection characteristics for snow, ice and water in the north of China. *IAHS*, 145, 451-462.
- Qunzhu, Z., Meisheng, C. and Xuezhi, F. (1984): Study on Spectral reflection characteristics of snow, ice and water of northwestern China. *Science Sinis (Series B)*. **27**, 647-656
- Rabus, B., Eineder, M., Roth, A. and Bamler, R. (2003): The shuttle radar topography mission - a new class of digital elevation models acquired by spaceborne radar. *ISPRS Journal of Photogrammetry and Remote Sensing*, 57, 241-262.
- Racoviteanu, A.E., Williams, M.W. and Barry, R.G. (2008): Optical remote sensing of glacier characteristics: a review with focus on the Himalaya. *Sensors*, 8, 3355-3383.
- Racoviteanu, A.E., Paul, F., Raup, B., Khalsa, S.J.S. and Armstrong, R. (2009): Challenges in glacier mapping from space: recommendations from the Global Land Ice Measurements from Space (GLIMS) initiative. *Annals of Glaciology*, 50 (53), 53-69.
- Rastner, P., T. Bolch, C. Notarnicola and F. Paul (2014): A comparison of pixel- and object-based glacier classification with optical satellite images. *Journal of Selected Topics in Applied Earth Observations and Remote Sensing*, 7 (3), 853-862.
- Rees, G. (1999): *The Remote Sensing Data Book*. Cambridge University Press
- Rees, G. (2001): *Physical Principles of Remote Sensing*. Cambridge University Press. 2<sup>nd</sup> edition.

- Ridley, J.K. and K.C. Partington (1988): A model of satellite radar altimeter return from ice sheets. *Int. J. Remote Sensing*, 9, 4, 601424.
- Rignot, E., Echelmeyer, K. and Krabill, W. (2001): Penetration depth of interferometric synthetic-aperture radar signals in snow and ice, *Geophysical Research Letters*, 28, 3501-3504.
- Rignot, E., Rivera, A. and Casassa, G. (2003): Contribution of the Patagonia Icefields of South America to sea level rise. *Science*, 302, 434-437.
- Rinne, E. J., Shepherd, A., Palmer, S., van den Broeke, M. R., Muir, A., Ettema, J. and Wingham, D. (2011): On the recent elevation changes at the Flade Isblink Ice Cap, northern Greenland. *Journal of Geophysical Research-Earth Surface*, 116, F03024.
- Robson, B.A., C. Nuth, S.O. Dahl, D. Hölbling, T. Strozzi and P. R. Nielsen (2015): Automated classification of debris-covered glaciers combining optical, SAR and topo-graphic data in an object-based environment. *Remote Sensing of Environment*, 170, 372-387.
- Rodriguez, E., Morris, C.S. and Belz, J.E. (2006): A global assessment of the SRTM performance. *Photogrammetric Engineering and Remote Sensing*, 72, 249-260.
- Rosen, P. A., Hensley, S., Joughin, I. R., Li, F. K., Madsen, S. N., Rodriguez, E. and Goldstein, R. M. (2000): Synthetic aperture radar interferometry - Invited paper, *Proceedings IEEE*, 88, 333-382.
- Rosmorduc, V., Benveniste, J., Bronner, E., Dinardo, S., Lauret, O., Maheu, C., Milagro, M. and Picot, N. (2011): Radar Altimeter Tutorial, J. Benveniste, N. Picot, Editors.
- Rott, H. and Markl, G. (1989): Improved snow and glacier monitoring by the Landsat Thematic Mapper. *Proceedings of a workshop on Landsat Thematic Mapper applications*, ESA, SP-1102, 3-12.
- Rott, H., Müller, F., Nagler, T. and Floricioiu, D. (2010): The imbalance of glaciers after disintegration of Larsen B ice shelf, Antarctic Peninsula. *The Cryosphere*. 4, 1607–1633, 2010.
- Sauber, J., Molnia, B., Carabajal, C., Luthcke, S. and Muskett, R. (2005): Ice elevations and surface change on the Malaspina Glacier, Alaska, *Geophysical Research Letters*, 32, L23S01.
- Scambos, T.A., Dutkiewicz, M.J., Wilson, J.C. and Bindschadler, R.A. (1992): Application of image cross-correlation to the measurement of glacier velocity using satellite image data. *Remote Sensing of Environment*, 42 (3), 177-186.
- Schenk, T. (1999): Digital Photogrammetry, 1, TerraScience, Laurelville, Ohio.
- Scherler, D., Leprince, S. and Strecker, M.R. (2008): Glacier-surface velocities in alpine terrain from optical satellite imagery - Accuracy improvement and quality assessment. *Remote Sensing of Environment*, 112 (10), 3806-3819.
- Schiefer, E., Menounos, B. and Wheate, R. (2007): Recent volume loss of British Columbian glaciers, Canada. *Geophysical Research Letters*, 34, L16503.
- Schutz, B.E., Zwally, H.J., Shuman, C.A., Hanock, D. and DiMarzio, J.P. (2005): Overview of the ICESat Mission. *Geophysical Research Letters*, 32, L21S01.
- Shepherd, A., Wingham, D., Ridout, A. and Muir, A. (2010): Initial Assessment of CryoSat-2 Performance over Continental Ice. *Proc. of American Geophysical Union, Fall Meeting 2010*.
- Shukla, A., M.K. Arora and R.P. Gupta (2011): Synergistic approach for mapping debris-covered glaciers using optical-thermal remote sensing data with inputs from geomorphometric parameters. *Remote Sensing of Environment*, 114 (7), 1378-1387.
- Sidjak, R.W. and Wheate, R.D. (1999): Glacier mapping of the Illecillewaet icefield, British Columbia, Canada, using, Landsat TM and digital elevation data. *International Journal of Remote Sensing*, 20, 273-284.

- Skvarca, P., Raup, B. and De Angelis, H. (2003): Recent behaviour of Glaciar Upsala, a fast-flowing calving glacier in Lago Argentino, southern Patagonia. *Annals of Glaciology*. 36, 184-188.
- Slobbe, D.C., Lindenbergh, R.C. and Ditmar, P. (2008): Estimation of volume change rates of Greenland's ice sheet from ICESat data using overlapping footprints. *Remote Sensing of Environment*, 112, 4204-4213.
- Smith, B.E., Fricker, H.A., Joughin, I.R. and Tulaczyk, S. (2009): An inventory of active subglacial lakes in Antarctica detected by ICESat (2003-2008). *Journal of Glaciology*. 55, (192), 573-595.
- Strohbehn, J.W. (1978): Modern theories in the propagation of optical waves in a turbulent medium. *Laser Beam Propagation in the Atmosphere Topics in Applied Physics*, 25, 45-106.
- Strozzi T., Murray, T., Wegmüller, U. and Werner, C. (2002): Glacier Motion Estimation Using SAR Offset-Tracking Procedures. *IEEE Transactions on Geoscience and Remote Sensing*, 40 (11), 2384-2391.
- Strozzi, T., Paul, F. and Kääb, A. (2010): Glacier mapping with ALOS PALSAR data within the ESA GlobGlacier project. *Proceedings of the ESA Living Planet Symposium*, 28 June - 2 July 2010, Bergen, Norway, ESA SP-686.
- Stuefer, M. (1999) Investigations on mass balance and dynamics of Moreno Glacier based on field measurements and satellite imagery. PhD Thesis, Univ. of Innsbruck, Austria.
- Thibert, E., Blanc, R., Vincent, C. and Eckert, N. (2008): Glaciological and volumetric mass-balance measurements: error analysis over 51 years for Glacier de Sarennes, French Alps. *Journal of Glaciology*, 54 (186), 522-532.
- Toutin, T. (2002): Three-dimensional topographic mapping with ASTER stereo data in rugged topography. *IEEE Transactions on Geoscience of Remote Sensing*, 40, 2241-2247.
- Toutin, T. (2004): Review article: Geometric processing of remote sensing images: models, algorithms and methods. *International Journal of Remote Sensing*, 25, 1893-1924.
- Toutin, T. (2008): ASTER DEMs for geomatic and geoscientific applications: a review. *International Journal of Remote Sensing*, 29, 1855-1875.
- Treichler D. and Kääb, A. (2016): ICESat laser altimetry over small mountain glaciers. *The Cryosphere*, 10, 2129-2146.
- Tsang, L., Kong, J.A. and Shin, R.T. (1985): Theory of Microwave Remote Sensing. New York: Wiley-Interscience.
- Ulaby, F.T., Moore, R.K. and Fung, A.K., Microwave remote sensing: active and passive, Addison-Wesley Publishing Company, London [etc.], (1982).
- Warren, S.G. (1984): Optical constraints of ice from the ultraviolet to the microwave. *Applied Optics*. 23, 1206.
- Weichel, H. (1990): Laser Beam Propagation in the Atmosphere. Tutorial texts in optical engineering, 102 pp.
- Werner, C., Strozzi T., U. Wegmüller, and A. Wiesmann (2002): SAR geocoding and multi-source image registration, *Proceedings of IGARSS 2002*, Toronto, Canada, 24-28 June 2002.
- Werner C., U. Wegmüller, T. Strozzi and A. Wiesmann, (2005): Precision estimation of local offsets between SAR SLCs and detected SAR images, *Proceedings of IGARSS 2005*, Seoul, Korea, 25-29 July 2005.
- WGMS (1989): World glacier inventory - Status 1988. In: Haeberli, W., Bösch, H., Scherler, K., Østrem, G. and Wallén, C. C. (eds.), IAHS (ICSI) / UNEP / UNESCO, World Glacier Monitoring Service, Zurich, Switzerland: 458 pp.
- Wilson, J. and Gallant, J. (2000): Terrain Analysis, Principles and Applications, John Wiley & Sons, Inc., New York.

- Wingham, D.J., Rapley, C.G. and Griffiths, H. (1986): New techniques in satellite altimeter tracking systems, Proc. IGARSS'86, 1, 185-190.
- Wingham, D.J. (1995): The limiting resolution of ice-sheet elevations derived from pulse-limited satellite altimetry. *Journal of Glaciology*, 41 (138), 413-422.
- Wingham, D.J., Ridout, A.J., Scharroo, R., Arthern, R.J. and Shum, CK. (1998): Antarctic elevation change from 1992 to 1996. *Science*, 282, 456-458.
- Wingham, D. J., Wallis, D. W. and Shepherd, A. 2009. Spatial and temporal evolution of Pine Island Glacier thinning, 1995-2006. *Geophysical Research Letters*. **36**(17)
- Winsvold, S. H., Kääb, A. and Nuth, C. (2016): Regional glacier mapping using optical satellite data time series. *IEEE Journal of Selected Topics in Applied Earth Observations and Remote Sensing* , 9(8), 3698-3711.
- Winther, J-G. (1993): Landsat TM derived and in situ summer reflectance of glaciers in Svalbard. *Polar Research*, 12 (1), 37-55.
- Wu, Q. X. (1995): A correlation-relaxation-labelling framework for computing optical flow-Template matching from a new perspective. *IEEE Transactions on Pattern Analysis and Machine Intelligence*, 17, 843-853.
- Yan, L., Wang, J., Hao, X., and Tang, Z. (2014): Glacier mapping based on rough set theory in the Manas River watershed. *Advances in Space Research*, 53, 1071–1080.
- Zappa, M. and Kan, C. (2007): Extreme heat and runoff extremes in the Swiss Alps. *Natural Hazards and Earth System Sciences*, 7, 375-389.
- Zemp, M., Paul, F., Hoelzle, M. and Haeberli, W. (2008): Alpine glacier fluctuations 1850-2000: An overview and spatio-temporal analysis of available data and its representativity. In: Orlove, B., Wiegandt, E. and Luckman, B. (eds.): *Darkening Peaks: Glacier Retreat, Science, and Society*. University of California Press, Berkeley and Los Angeles, 152-167.
- Zlotnicki, V., Fu, L.L. and Patzert, W. (1989): Seasonal variability in global sea level observed with Geosat altimetry. *Journal of Geophysical Research*, 94, C12, 17959-18237.
- Zwally, H.J. and A.C. Brenner (2001): Ice sheet dynamics and mass balance, In: Fu, L.L. and A. Cazenave (eds.) *Satellite altimetry and earth sciences*, New York, Academic Press Inc., 351–369.
- Zwally, H.J., Schutz, B., Abdalati, W., Absihre, J., Bentley, C., Brenner, A., et al. (2002): ICESat's lasar measurements of polar ice, atmosphere, ocean and land. *Journal of Geodynamics*, 34, 405-445.

## Abbreviations

ALOS	Advanced Land Observing Satellite
AOI	Area Of Interest
ASAR	Advanced SAR
ASTER	Advanced Spaceborne Thermal Emission and Reflection radiometer
CC	Correlation Coefficient
CCF	Cross Correlation in the Frequency domain
CGIAR	The Consultative Group on International Agricultural Research
CRL	Correlation Relaxation Labelling
GCP	Ground Control Point
GIS	Geographic Information System
GLIMS	Global Land Ice Measurements from Space
GNSS	Global Navigation Satellite System
GTN-G	Global Terrestrial Networks - Glaciers
DARD	Data Access Requirement Document
DEM	Digital Elevation Model
DInSAR	Differential InSAR
DMRT	Dense Medium Radiative Transfer
DN	Digital Number
DOS	Dark Object Subtraction
ECV	Essential Climate Variable
ERS	European Remote-sensing Satellite
ETM+	Enhanced Thematic Mapper plus
FCDR	Fundamental Climate Data Record
InSAR	Interferometric repeat-pass SAR
IWS	Interferometric Wide Swath
kHz	kilo Hertz
LIDAR	Light Detection and Ranging
LOS	Line Of Sight
LRM	Low Resolution Mode
NED	National DEM
NCC	Normalized Cross-Correlation
NIR	Near-InfraRed part of the electromagnetic spectrum
NDSI	Normalized Difference Snow Index
NDVI	Normalized Difference Vegetation Index

PALSAR	Phased Array type L-band SAR
PCA	Principle Component Analysis
PSD	Product Specifications Document
RADAR	Radio Detection And Ranging
RGB	Red Green Blue
RMSE	Root Mean Square Error
RSS	Root Sum of Squares
SAR	Synthetic Aperture Radar
SB-SAR	Satellite-Borne repeat pass SAR
SLC	Single Look Complex(for SAR)
SLC-off	Scan Line Corrector off (for Landsat 7)
SNR	Signal-to-Noise Ratio
SPOT	System Pour l'Observation de la Terre
SRTM	Shuttle Radar Topography Mission
SWIR	Short Wave InfraRed
THz	Tera Hertz
TOA	Top of Atmosphere
TM	Thematic Mapper
URD	User Requirement Document
USGS	United States Geological Survey
UTM	Universal Transverse Mercator
VIS	VISible part of the electromagnetic spectrum
VNIR	Visible to Near-InfraRed part of the electromagnetic spectrum
WGI	World Glacier Inventory
WGMS	World Glacier Monitoring Service